Experimental study of 3D magneto-photonic crystals made of silica inverse opals doped by magnetic nanoparticles

Renata Kékesi

Année: 2011

UNIVERSITE JEAN MONNET

SAINT ETIENNE

FRANCE

THESE

Pour obtenir le grade de

DOCTEUR

Laboratoire Télécom Claude Chappe

École Doctorale « Science, Ingénierie et Santé »

Présentée et soutenue publiquement

Le 19 Octobre 2011

par

Renata Kékesi

Étude expérimentale de cristaux magnéto-photoniques 3D réalisés sous forme d'opales inversés par une matrice de silice dopée en nanoparticules magnétiques

Jury:

DR. Béatrice DAGENS	Rapporteur
Prof. Joël BELLESSA	Rapporteur
Prof. Etelka TOMBACZ	Co-directrice
DR Taha BENYATTOU	Président
Dr. Jean-Pierre CHATELON	Co-directeur
Dr. François ROYER	Co-encadrant
Dr. Damien JAMON	Examinateur

Year : 2011

UNIVERSITY OF JEAN MONNET

SAINT ETIENNE

FRANCE

THESIS

Laboratoire Télécom Claude Chappe

École Doctorale « Science, Ingénierie et Santé »

Experimental Study of 3D Magneto-Photonic Crystals Made of Silica Inverse Opals Doped by Magnetic Nanoparticles

Thesis by

Renata Kékesi

2011 October 19 th

Judges:

DR Béatrice DAGENS	Reviewer
Prof. Joël BELLESSA	Reviewer
Prof. Etelka TOMBACZ	Co-director
DR Taha BENYATTOU	Chairman
Dr. Jean-Pierre CHATELON	Co-director
Dr. François ROYER	Co-supervisor
Dr. Damien JAMON	Examiner

"No amount of experimentation can ever prove me right, a single experiment can prove me wrong."

"Une infinité d'expériences ne pourra jamais donner une preuve définitive de ma théorie, tandis qu'une expérience unique pourrait la réfuter."

"Végtelen számú kísérlet sem bizonyíthatja, hogy igazam van, de egyetlen kísérlet is bizonyíthatja, hogy tévedtem."

Albert Einstein

INTRODUCTION (FRANCAIS) 11

INTRODUCTION 15

I. CHAPITRE: MATERIAUX MAGNETO-OPTIQUES (RESUME FRANCAIS) 19

I. CHAPTER: MAGNETO-OPTICAL MATERIALS 25

I.1. Technologic and scientific context 25
I.1.1. Faraday rotation 26
I.1.2. Isolator realizations 29

I.2. Magneto-optical materials for integration 30

I.3. The "composite" approach 31

I.4. Magneto-Photonic Crystals (MPC) structures 36
I.4.1. Photonic Crystals (PC) 38
I.4.2. Magneto-Photonic Crystals (MPC) 41

I.5. Motivations, goals and research plan 46

II. CHAPITRE: ARRANGEMENT PERIODIQUE (RESUME FRANCAIS) 49

II. CHAPTER: PERIODIC ARRANGEMENT 53

II.1. General properties of Photonic Crystals 53
II.1.1. What is the interest of Photonic Crystals? 53
II.1.2. Propagation of light in Photonics Crystals: from Maxwell equation to "Master equation" 56
II.1.3. Reciprocal lattice and Brillouin zone 58
II.1.4. Bloch mode 61
II.1.5. Dispersion relation for 3D crystals 62
II.1.6. 1D dispersion relation 65

II.2. Dispersion relation of 1D Magneto-Photonic Crystals 68

II.3. One Dimensional Calculations 70
II.3.1. 4x4 Transfer matrix calculations 71
II.3.2. Magneto-optical 1D calculation 73
II.3.3. "Microcavity" structure 76
II.3.4. "Periodic" structure 77
II.3.5. Comparison between the "periodic", "microcavity" and monolayer structure 77

II.4. Conclusion 81

III. CHAPITRE: ÉLABORATION ET CARACTERIZATION DE CRISTAUX MAGNETO-PHOTONIQUE 3D (RESUME FRANCAIS) 83

III. CHAPTER: ELABORATION AND CHARACTERIZATION OF 3D MAGNETO-PHOTONIC CRYSTALS 89

III.1. Opal based 3D Photonic Crystals 90
III.1.1. Natural opal 90
III.1.2. Artificial opal 91
III.1.2.1. Direct opal 91
III.1.2.2. Self-assembly methods 92
III.1.2.3. Fcc arrangement 95
III.1.2.4. Inverse opals 98

III.2. Elaboration of 3D opal based Photonic and Magneto-Photonic Crystal 100
III.2.1. Properties of polystyrene sphere 100
III.2.1.1. Material of the direct opal 100
III.2.1.2. Solubility of the polystyrene spheres 101
III.2.2. Sol gel process 101
III.2.2.1. Preparation of TEOS solution 103
III.2.2.2. Cobalt-ferrite nanoparticles ($CoFe_2O_4$) 104
III.2.2.3. Sol-Gel Doping 105
III.2.3. Realization of Photonic and Magneto Photonic Crystal 106
III.2.3.1. Preparation of the substrate 106
III.2.3.2. Vertical deposition (VD) 106
III.2.3.3. Doping 107
III.2.3.4. Impregnation 107
III.2.3.5. Elimination of the polystyrene spheres from the silica opal 107

III.3. Characterization 109
III.3.1. Scanning Electron Microscope (SEM) 109
III.3.2. Ellipsometry 110
III.3.3. Optical and magneto-optical characterization 112
III.3.3.1. Description of the optical bench 113
III.3.3.2. Transmittance measurement 114
III.3.3.3. Faraday rotation 115

III.4. Conclusion 118

IV. CHAPITRE: COMPORTEMENT MAGNETO-PHOTONIQUES DES OPALES ELABORES (RESUME FRANCAIS) 121

IV. CHAPTER: OPTICAL PROPERTIES OF ELABORATED OPALS: MAGNETO-PHOTONIC BEHAVIOR 131

IV.1. Optical properties of doped silica monolayers 131
IV.1.1. Refractive index 132
IV.1.2. Faraday rotation hysteresis loop 133
IV.1.3. Faraday rotation spectrum 135

IV.2. Optical and structural properties of undoped opals 136
IV.2.1. Direct opals 137
IV.2.1.1. PBG position 137
IV.2.1.2. Study of the structure 140
IV.2.1.3. SEM images 143
IV.2.2. Inverse opals 144
IV.2.2.1. PBG position 145
IV.2.2.2. Study of the structure 148
IV.2.2.3. SEM images 150

IV.3. Magneto-optical inverse opals 151

IV.3.1. PBG position 151
IV.3.2. Study of the structure 154
IV.3.3. SEM images 155
IV.3.4. Faraday rotation enhancement 156
IV.3.5. Merit factor 161

CONCLUSION (FRANCAIS) 163

CONCLUSION 167

ACKNOWLEDGEMENT 171

REFERENCE 173

INTRODUCTION (FRANCAIS)

Les lasers, filtres, photo-détecteurs, multiplexeurs, amplificateurs, modulateurs, ou encore commutateurs optiques sont tous des éléments intégrés au sein des circuits optiques utilisés dans le domaine des télécommunications. L'isolateur est le seul élément qui n'a pas encore pu être intégré. Ce composant autorise le passage de la lumière dans une seule direction, en bloquant la propagation dans le sens retour. Cette fonction permet ainsi d'éviter tout risque d'endommagement ou d'instabilité des lasers dû aux reflexions parasites. Elle est basée sur la non-réciprocité de la rotation Faraday des matériaux magnéto-optiques (MO).

Les isolateurs disponibles existent seulement sous la forme de composants discrets d'espace libre. Ils présentent des effets MO importants avec une isolation élevée et de faibles pertes d'insertion. Cependant, un traitement thermique élevé (~ 700 °C) est nécessaire pour la cristallisation des matériaux magnétiques les constituant. Cette température n'est pas compatible avec les technologies classiques d'optique integrée, c'est à dire avec les semiconducteurs III-V, la silice, le silicium ou avec des matériaux polymères. Pour surmonter ce problème de compatibilité, le laboratoire LT2C a travaillé sur le développement d'un matériau composite. Ce matériau est obtenu en dopant une solution sol-gel avec des nanoparticules magnétiques issues d'un ferrofluide de ferrite de cobalt ($CoFe_2O_4$). Ainsi, des couches minces de matériaux magnétiques compatibles avec la technologie sur verre sont développées par l'intermédiaire d'un procédé basse température.

Une concentration volumique de $CoFe_2O_4$ de 1 % dans des couches composites permet d'obtenir une rotation Faraday de 200 °.cm^{-1} à 1550 nm. Cependant, le facteur de mérite, défini comme rapport entre la valeur de la rotation Faraday et l'absorption optique, est d'environ 7 °. Cette valeur est encore trop faible pour considérer ce matériau comme un bon candidat pour les applications intégrées.

Différents auteurs [1-5] ont montré que l'effet magnéto-optique peut être augmenté en utilisant une structure de cristaux photoniques. Ces derniers sont essentiellement obtenus par structuration de l'oxyde de grenat au moyen de la photolithogravure. D'autre part, Nishijima *et al.*[6] ont montré que des cristaux photoniques 3D peuvent être élaborés à partir de silice

fabriquée à l'aide de la technique sol-gel. Cette approche semble être entièrement compatible avec le matériau composite développé au laboratoire.

Ainsi, l'objectif principal de cette étude est la réalisation et l'étude magnéto-optique de cristaux magnéto-photoniques 3D basés sur une structure auto-assemblée d'opales. Cette structure agit comme un moule pour la solution sol-gel dopée avec des nanoparticules magnétiques.

Cette thèse se compose de quatre chapitres.

Le premier présente les informations générales nécessaires à la compréhension des enjeux principaux de cette étude. Les isolateurs optiques et les difficultés de leur intégration sont traités. Ensuite, un bref état de l'art des matériaux magnéto-optiques est proposé et l'intérêt de l'approche «composite» développée par le LT2C est montré. Après une courte introduction sur les cristaux photoniques (CP), l'utilisation d'un matériau magnéto-optique associé à un cristal photonique 3D est présentée, en accordant une attention particulière à l'amélioration de la rotation Faraday. Enfin, les motivations et les objectifs de cette étude sont donnés.

Dans le second chapitre, est présentée la structure du CP qui est capable de contrôler la propagation de la lumière. Le contrôle de la propagation peut être étudié au travers de la relation de dispersion. Cette dernière montre la propagation de la lumière dans un matériau en fonction de la longueur d'onde, et une analogie avec le diagramme de bandes électroniques dans le cas de la propagation des électrons est montrée. A une dimension, ce type de structure a été simulé en utilisant la silice dopée avec de la ferrite de cobalt réalisée classiquement au LT2C, la bande interdite photonique (BIP) a été observée à 1550 nm. Ce calcul met en évidence une amélioration de l'effet magnéto-optique dans la BIP correspondante par rapport à une monocouche magnétique simple. Pour deux sortes d'arrangement de la structure, le renforcement des effets MO ne se produit pas au même endroit par rapport aux BIP respectives.

Le troisième chapitre est consacré aux propriétés des matériaux utilisés et au processus d'élaboration des cristaux photoniques magnétiques et non magnétiques. Des opales artificielles à base de sphères de polystyrène, sont utilisées comme moule pour la réalisation de cristaux magnéto-photoniques 3D (CPM). L'étape suivante est la réalisation d'opales

inverses 3D magnétiques et non magnétiques grâce à l'utilisation d'une solution de TEOS. Cette solution est compatible avec le ferrofluide utilisé (ferrite de cobalt), dont les effets magnéto-optiques sont connus. L'opale direct peut être imprégné par la solution de TEOS dopée ou non dopée, et ensuite les billes de polystyrène peuvent être éliminées. Cette élimination est réalisée avec un acide afin de travailler à basse température. Une présentation des différentes techniques de caractérisation, comme la microscopie électronique à balayage, l'ellipsométrie et la polarimétrie spectrale est proposée en fin de chapitre.

Le dernier chapitre présente les résultats optiques et magnéto-optiques obtenus lors de ce travail. Tout d'abord, les propriétés des couches de silice dopées sont exposées en vue de déterminer la concentration volumique optimale des nanoparticules de ferrite de cobalt dans la matrice sol-gel et d'analyser la qualité du dopage en terme de comportement magnétique et magnéto-optique. Ensuite, les résultats concernant les propriétés optiques et structurelles des opales élaborés sont rassemblés. Leurs analyses donnent une bonne idée de la qualité de l'arrangement que nous avons pu atteindre. Enfin, les principaux résultats de cette étude, par l'intermédiaire des propriétés optiques et magnéto-optiques sont donnés pour l'opale dopé. La capacité de ces structures de se comporter comme des CPM est présentée. Puis les résultats sont résumés, et quelques perspectives sont dressées.

INTRODUCTION

Lasers, optical filters, photo detectors, multiplexers, amplifiers, modulators, switches are integrated elements of high performance telecommunication systems. Isolator is the only element, which has not been integrated yet. This magneto-optical device assures that the transmitted light passes in one direction, but it blocks the backward propagation into the laser and avoids damage risk or instabilities. This function is based on a non-reciprocal Faraday rotation effect of magneto-optical (MO) materials.

The available isolators exist only through bulk forms. They exhibit large MO effects leading to high isolation ratio and low insertion losses. Nevertheless, a high temperature (~700 °C) annealing process is required for their crystallization. This temperature is not compatible with classical integrated technologies, i.e. with III-V semiconductors, silica, silicon or with polymer materials. To overcome this compatibility problem, the LT2C laboratory has worked on the development on a composite material. This last is obtained by doping a metallic precursor solution with magnetic nanoparticles issued from a cobalt-ferrite based ferrofluid. From this, glass compatible thin layers of diluted magnetic material are developed via a low temperature sol-gel process.

For 1% volume fraction of $CoFe_2O_4$ the Faraday rotation of such a composite layer reach 200 $°\cdot cm^{-1}$ at 1550 nm. However, the merit factor, which is the quality ratio between the Faraday rotation and the absorption, is about 7 $°^{1}$. This value is still too low to consider this material as a good candidate for integrated applications.

Based on the literature [2–6] the magneto-optical effect can be increased using photonic crystal structure. These last are essentially obtained by patterning garnet oxide by means of photolithography. Moreover, Nishijima *et al.*[7] reported that 3D photonic crystal can be elaborated on a use of silica sol-gel method. This bottom up approach seemed to be fully compatible with the composite material developed by the laboratory.

Thus, the main purpose of this study is the realization of 3D magneto-photonic crystal based on self-assembled opal structure. This structure acts as a removable template for magnetic nanoparticles doped sol gel solution.

This thesis consists of four main parts.

The first one deals with the general information required to understand the main issues of this study. Optical isolator and its integration's difficulties are discussed. Next, we produce a brief review of magneto-optical materials and we show the interest of the "composite" approach developed by the LT2C. After a short introduction on photonic crystals (PC), the use of magneto-optical material associated with a 3D photonic crystal (Magneto-Photonic Crystals: MPC) is presented, by paying a special attention to the enhancement of the Faraday rotation. Finally, motivations and goals of this study are given.

In the second part, we will present PC structure, which is able to control the propagation of the light. This propagation control can be derived from the dispersion equations relation, like electronic band diagram in the case of the electron propagation, shows the light propagation of a material as a function of the wavelength. In one dimension such a structure was simulated using the cobalt-ferrite doped silica material of LT2C laboratory, where the PBG was positioned at 1550 nm. This calculation evidences an enhancement of the magneto-optical effect in a corresponding PBG compared to a simple magnetic monolayer. For two kinds of arrangements the MO effect enhancement does not occur at the same place with regard to the corresponding PBG.

Thirdly, we will show the properties of the used materials and the elaboration process of the magnetic and non-magnetic photonic crystals. Artificial opal, based on polystyrene spheres, can be used as a template of the realization of 3D MPCs. The next step is the realization of the 3D magnetic and non-magnetic inverse opals. For these last, we used TEOS solution, which utilization is already well-known in the literature[7]. This solution is compatible with our cobalt-ferrite ferrofluid, whose magneto-optical effects are well-examined. Accordingly, the direct opal template can be impregnated by doped or non-doped TEOS solution, and then the template can be eliminated. (It is important to note, that we chose an acid elimination, because we wanted to work at low-temperature.) This will be followed by a presentation of the functions of the applied characterization equipment, as Scanning Electron Microscopy, Ellipsometry, Free Space Ellipsometry and Spectral Polarimeter.

Finally, the last chapter is related to the optical and magneto-optical results obtained during this work. A first section is dedicated to the properties of silica doped layers in order to determinate the volume fraction of nanoparticles in the matrix and to analyze the quality of the doping in terms of magnetic and magneto-optical behavior. In the second section are gathered the results concerning the optical and structural properties of the elaborated opals.

Their analyze gives a good idea of the quality of the arrangement we were able to reach. The last section gives the main results of this study through the optical and magneto-optical properties of the doped opal. The ability of these structures to behave as MPC is presented. Then the results are summarized and some perspectives are given.

I. CHAPITRE: Matériaux magnéto-optiques (resumé francais)

L'objectif de ce travail est de développer un matériau magnéto-optique composite organisé en cristal photonique 3D utilisable, par exemple, dans un isolateur optique. La structuration périodique a pour but d'augmenter les propriétés magnéto-optiques comme la rotation Faraday et ainsi le facteur de mérite du matériau. Le composant isolateur, utilisé notamment dans le domaine des télécommunications infra-rouge (1550 nm), a pour fonction de laisser passer le signal lumineux dans un sens et de le bloquer dans le sens contraire, ce qui permet de protéger les équipements qui sont très sensibles aux réflexions comme les sources laser. Il utilise pour cela le caractère non réciproque des interactions magnéto-optiques.

L'isolateur est très présent dans les réseaux de télécommunications, mais sous forme de composant discret d'espace libre. Il y a donc un besoin fort de réaliser des isolateurs intégrés et par conséquent, il est nécessaire d'axer l'étude sur l'élaboration de matériaux magnétiques sous la forme de couches minces. Or les matériaux magnétiques classiques nécessitant une température de cristallisation très importante (~ 700°C), ils ne se prêtent pas forcément à leur élaboration en film mince avec les technologies classiques d'optique intégrée. Ils peuvent par contre se retrouver sous la forme de nanoparticules diluées dans une matrice compatible.

La rotation Faraday est un phénomène magnéto-optique (rotation de la polarisation de la lumière en fonction d'un champ magnétique) observable dans les matériaux diélectriques en présence d'un champ magnétique. La polarisation de la lumière peut être décomposée en deux polarisations circulaires tournant en sens contraire. Ces deux polarisations vont se propager à des vitesses différentes dans le matériau. Ces deux composantes vont être ainsi déphasées. Par conséquent, un rayon lumineux va avoir sa polarisation modifiée par passage dans un matériau diélectrique soumis à un champs magnétique. Les performances d'un isolateur sont évaluées en fonction de la rotation Faraday du matériau qui doit être la plus élevée possible et du coefficient d'absorption de ce même matériau, qui lui, devra être le plus faible possible. Le

facteur de mérite, donné par $\frac{Rotation\ Faraday}{Coefficient\ d'absorption}$, permet de chiffrer le compromis entre les deux paramètres cités précédemment.

Cette rotation Faraday peut être obtenue en utilisant des matériaux magnétiques. Les ferrofluides sont de bons candidats pour l'obtention de ce type d'effet magnétique. Ces composés magnétiques peuvent être élaborés sous la forme de nanoparticules supportées dans une matrice obtenue par la méthode sol-gel. Ces composés sont des particules mono-domaines qui ont une anisotropie uniaxiale. Le procédé sol-gel est une technique de dépôt de couches minces par voie liquide et ne nécessite pas une température de process très élevée. Des isolateurs à base d'oxydes de grenat sont réalisés mais les températures élevées lors de leur fabrication empêchent toute utilisation de polymère, silice ou semiconducteurs III-V.

Les matériaux magnétiques peuvent aussi être insérés dans des cristaux photoniques. Les cristaux photoniques sont des arrangements périodiques à 1, 2 ou 3 dimensions de plusieurs matériaux de constantes diélectriques différentes. Cette structuration peut se retrouver sous la forme de multi-couches, de barreaux entrecroisés ou encore de billes structurées [6, 26, 37, 39, 49]. Ainsi, la réflexion de Bragg va mettre en évidence un effet d'amplification optique. Ces matériaux artificiels vont présenter une bande interdite photonique (BIP) : pour une gamme de longueur d'onde de la lumière la transmission optique sera nulle. Yablonovitch [37] a été le premier a proposé une telle structure: Dans une certaine gamme de longueur d'onde, la propagation de la lumière peut être améliorée, alors que dans la BIP, la transmission optique est fortement diminuée. Ce matériau est une structure 3D cubique face centrée (cfc). La différence d'indices de réfraction est importante. Cette structure théorique est proposée par empilement de billes de polystyrène ou de motifs hexagonales noyés dans un verre.

Lopez *et al*. ont fabriqué des réseaux 3D, appelés aussi opale direct, en empilant des billes de polystyrène dans une matrice de silice. La taille de ces billes a une influence sur la position de la longueur d'onde centrale de la bande interdite photonique:

$$\lambda_c = 2d_i cos\theta \sqrt{\frac{2}{3}\left[f_{sph}n_{sph}^2 + \left(1 - f_{sph}\right)n_{bg}^2\right]} \quad \text{Eq 1}$$

D'après la loi de Bragg, λc correspond à la position centrale de la bande interdite, f_{sph} est le facteur de remplissage des billes de polystyrène (dans une structure cfc parfaite, le facteur d'entassement atomique est égale à 0,74), n_{sph} et n_{bg} sont respectivement l'indice de réfraction des billes et l'indice de réfraction de la matrice. d_i est l'espace mesuré interplanaire correspondant à la distance entre les plans cristallins. d_i est donné par la relation $d_i = 0{,}816.d_{sph}$ où d_{sph} correspond au diamètre des billes. Enfin, θ est l'angle d'incidence du faisceau laser. Lopez *et al*. ont mis en évidence la position de la longueur d'onde centrale de la BIP en fonction du plan d'arrangement cristallin de la structure [54].

Nishijima *et al*. ont fabriqué et caractérisé des opales directs et inverses à trois dimensions en utilisant la technique sol-gel. Les dimensions des billes sont comprises entre 220 et 600 nm. Les opales directes sont fabriquées à partir de billes de polystyrène calibrées et soumises à une centrifugation. Cette technique permet un arrangement périodique des billes sous une structure cfc (cubique face centrée). Des opales inverses ont été réalisés par l'imprégnation d'une solution de tétraéthyle orthosilicate (TEOS). Après séchage, les billes de polystyrène sont éliminées de la structure par de l'acétate d'éthyle. L'épaisseur de la couche mince obtenue est d'environ 100µm avec une transmission optique de 80 %. L'écart relatif de la position centrale de la BIP, entre la mesure et la valeur théorique, est de 1 % pour les opales directs et inférieure à 7 % pour les opales inverses. λ_C est liée à la méthode d'élaboration. Ainsi avec une même taille de sphères, pour les opales inverses et directs, la valeur de λ_C est décalée. De plus, Nishijima et al. ont mis en évidence le lien entre la valeur de λ_C et la taille des billes [6].

Des études ont été réalisées afin d'obtenir une rotation Faraday la plus élevée possible. Levy *et al*. ont simulé des structures periodiques (1D CMP) de couches minces d'indices différents : matériaux isotrope à 1,926 et magnétique à 2,21. Avec différents arrangements, il a obtenu une rotation Faraday de -45 ° [2].

Des cristaux photoniques à base de grenat ($Bi_3Fe_5O_{12}$) dopé erbium ont été simulés par Grishin *et al*. La bande interdite photonique est centrée sur 1532 nm. La rotation Faraday et le

facteur de mérite simulés peuvent atteindre respectivement -45 ° et -277 ° avec 128,6 μm d'épaisseur de grenat[42].

Inoue *et al*. ont réalisé des cristaux photoniques 1D avec une alternance de Ta_2O_5 et SiO_2, et une microcavité au centre de cette périodicité. Cette microcavité est constituée d'un matériau aux propriétés magnéto-optiques connues (YIG substitué Bismuth). L'épaisseur de la couche mince Bi:YIG est de 230 nm. La longueur d'onde centrale de la BIP est voisine de 650 nm, et la rotation Faraday est de -0,80 °. Ils ont aussi montré, par simulation, une amélioration de la rotation de Kerr en utilisant du cobalt comme matériau magnétique [1, 4].

Dans la littérature, la plupart des composites magnétiques 3D a été réalisé en utilisant des opales de silice (SiO_2) [1, 45-47]. Les matériaux magnétiques utilisés sont la maghémite, le Terbium-gallium-grenat (TGG) ou encore le YIG substitué Bismuth [1, 45]. Le taux de remplissage de billes de silice est de 75%. Les BIP ont été observées aux mêmes longueurs d'ondes que l'opale direct de SiO_2, à 590 nm, pour des diamètres de billes de 300 nm. La rotation Faraday a été observée dans tous les cas dans les BIP.

Une solution de glycérol saturée de dysprosium-nitrate a été testée par Koerdt *et al*. afin de mettre en évidence l'influence de cet arrangement sur la BIP, sachant que les billes de glycérol ne sont pas magnétiques. Mais tous ces auteurs obtiennent des longueurs d'onde bien inférieures à l'objectif fixé pour le fonctionnement des matériaux dans l'infra-rouge (1550 nm) [47].

Le développement de nouveaux matériaux magnétiques est inévitable afin de développer des composants optiques qui permettent le passage ou non d'une onde lumineuse. Ce dispositif doit être compatible avec les technologies classiques, c'est à dire pouvoir être intégré et fabriqué à de faibles températures.

Le laboratoire LT2C élabore des couches minces comportant une matrice de silice dopée de nanoparticules ferromagnétiques (ferrite de Cobalt) [8, 27]. La matrice de silice est élaborée à partir de la technique sol-gel, technique ne nécessitant pas de températures de process trop élevées (90 °C au maximum). Les films minces obtenus permettent d'obtenir à 820 nm, 220 °.cm^{-1} de rotation Faraday pour 1% en volume de nanoparticules. Des mesures à 1550 nm ont aussi mis en évidence une rotation Faraday de 200°.cm^{-1} et un facteur de mérite

de 7 °. Cette dernière longueur d'onde correspond au domaine visé des télécommunications. Cependant, le facteur de mérite est encore faible.

Basé sur la littérature, les effets magnéto-optiques peuvent être augmentés en utilisant une structure dénommée « cristal photonique » au lieu d'une simple couche mince. L'objectif de ce travail est le développement d'un matériau artificiel à partir d'un arrangement périodique tridimensionnel et des compétences acquises sur l'élaboration de nanoparticules de ferrite de cobalt dans une matrice sol-gel de silice.

I. CHAPTER: Magneto-Optical Materials

This chapter gives the general information required to fix the main issues of this study. Firstly, the technologic and scientific context of this study is explained using the example of the optical isolator. Few scientific elements are given on the Faraday rotation which is the basic property of the isolator in order to present the problem of the integration of this function inside Photonic Lightwave Circuits. Secondly, a short review of the magneto-optical materials used for the integration of optical isolators will introduce the interest of the "composite" approach developed by the LT2C for several years using magnetic nanoparticles. The following section will be concerned by a presentation of the potentialities of the Magneto-photonic crystals with a short review of the 3D photonic crystals and a special attention to the enhancement of the non-reciprocal effects in 1D and 3D structures. Finally, the goals of the study will be given.

I.1. Technologic and scientific context

The rapid progress of data transmission capacities has led to the development of optical communication techniques via glass fiber in the near infrared. The light sources that are used are usually III-V laser diodes, which are very sensitive to the reflected light. This reflection can cause amplitude modulation and frequency shifts which in high power source laser can cause damage. Furthermore, in long distance fiber telecommunications, optical amplifiers are required in order to increase the signal power which is attenuated by the fiber absorption. A schematic view of such an optical amplifier is given on ***Figure I-1***, through the example of an Erbium Doped Fiber Amplifier (EDFA).

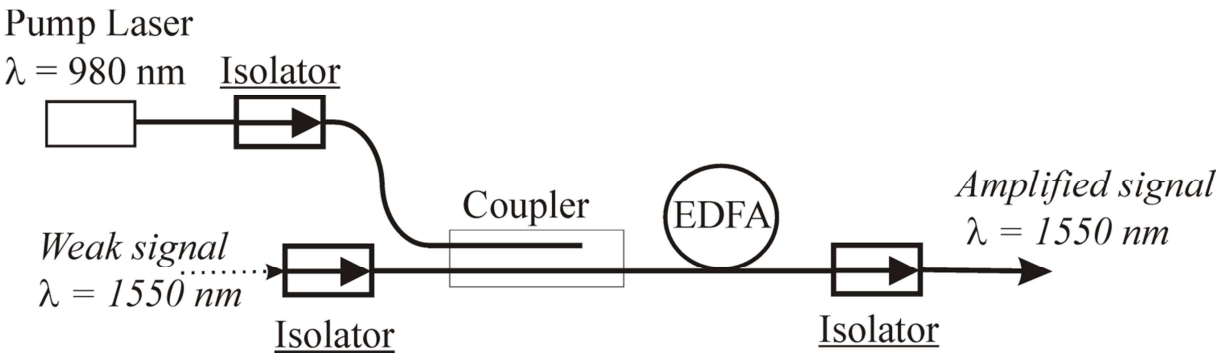

Figure I-1: Schematic view of the use of an Erbium-Doped Fiber Amplifier (EDFA). Three optical isolators are required in this arrangement

Due to their large sensitivity to the backtravelling light, the laser pump source and the EDFA are protected by several optical isolators. Such isolators play the role of optical diodes by allowing the propagation of the light in the main direction but blocking it in the other one. This is a non-reciprocal behavior which is based on the use of magneto-optical material submitted to a longitudinal magnetic field. This non-reciprocity is well known through the Faraday rotation.

The following section details its physical origin and how it can be used to obtain an isolation behavior [8].

I.1.1. Faraday rotation

The Faraday rotation (FR) is the main magneto-optical effect. Observed by Michael Faraday in 1845, it was the first evidence of the relation between the magnetism and the light. The FR is the polarization rotation observed on a light beam in a magneto-optical medium submitted to a longitudinal magnetic field. (Magnetic field direction is parallel to the light beam) [9].

Indeed, the application of a magnetic field on a material with a direction parallel to the light beam (O_z) produces an off-diagonal element ε_{xy} in the permittivity tensor $\hat{\varepsilon}$:

$$\hat{\varepsilon} = \begin{bmatrix} \varepsilon_{xx} & +\varepsilon_{xy} & 0 \\ -\varepsilon_{xy} & \varepsilon_{xx} & 0 \\ 0 & 0 & \varepsilon_{xx} \end{bmatrix} \quad \text{Eq I.1}$$

where $\hat{\varepsilon_j} = \varepsilon'_j + i\varepsilon"_j$ elements have real and imaginary parts, where *j=xx or xy* [10].
For diagonal elements $\varepsilon'_{xx} = n^2 - k^2$ and $\varepsilon"_{xx} = 2nk$, where n is the refractive index of the material and k is the extinction coefficient. Obviously, the magnitude of the off-diagonal elements depends on the kind of material.

For such a permittivity tensor, eigenpropagation modes are circular (left and right) due to the circular symmetry created by the magnetic field. Furthermore, the left and right rotating circular polarizations propagate with different propagation constants given in terms of refractive index through:

$$\nu_L = \sqrt{\varepsilon_{xx} + \varepsilon_{xy}} \qquad \text{Eq I.2}$$

$$\nu_R = \sqrt{\varepsilon_{xx} - \varepsilon_{xy}} \qquad \text{Eq I.3}$$

where ν_l is the left and ν_r is the right circular vibration. $\nu_L - \nu_R$ is the optical birefringence between left and right circular polarization.

Let's consider an electromagnetic waves travelling through such a material. Before the material, it is linearly polarized. At the input of the material, it is divided into right and left circular polarizations with identical magnitude and phase. At the output, due to their different refractive index, these two eigenmodes are phase-shifted and do not possess the same magnitude. Thus, their recombination is made through an elliptical polarized vibration (***Figure I-2a***). The polarization modification is written in terms of Faraday rotation θ_F and the Faraday ellipticity ϵ_F, which are expressed as:

$$\theta_F = \left(\frac{\pi h}{\lambda}\right) Re\,(\nu_L - \nu_R) \sim \left(\frac{\pi h}{\lambda}\right) Re\left(\frac{\varepsilon_{xy}}{\sqrt{\varepsilon_{xx}}}\right) \sim \left(\frac{\pi h}{\lambda n}\right) Re\,(\varepsilon_{xy}) \qquad \text{Eq I.4}$$

$$\epsilon_F = \frac{\pi h}{\lambda} Im\,(\nu_L - \nu_R) \qquad \text{Eq I.5}$$

where h is the thickness of the material and λ is the wavelength.

If the electromagnetic wave travels through the material and back, the polarization is not coming back into its initial state, but supports double Faraday rotations ($2\theta_F$) (***Figure I-2b***). It

is due to the fact that the sign of the off-diagonal element depends whether the magnetic field is parallel to the light beam or anti-parallel. This phenomenon is the simplest demonstration of the non-reciprocity.

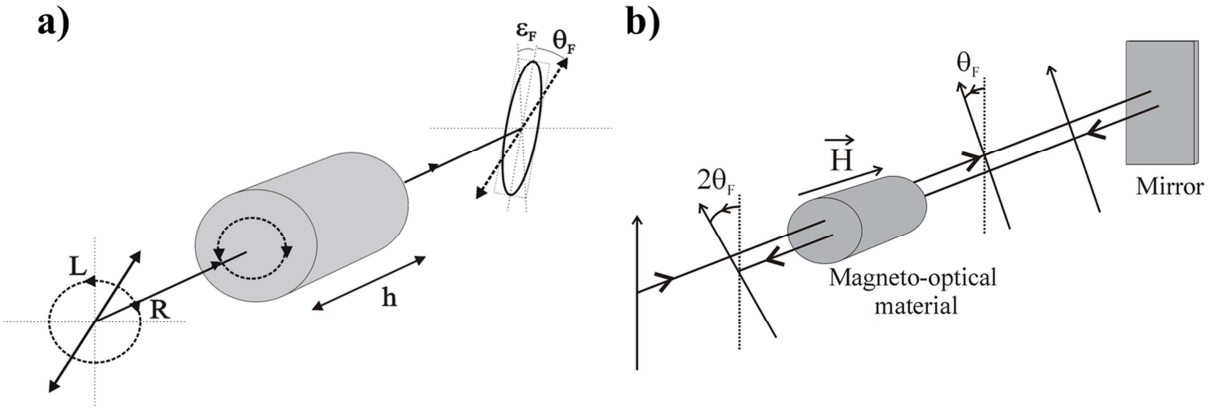

Figure I-2: Schematic view of the Faraday effect (a) and of the non-reciprocity of the rotation (b)

Such a non-reciprocal rotator is the basic element of the optical isolator. A schematic view of an integrated type isolation is given on ***Figure I-3***.

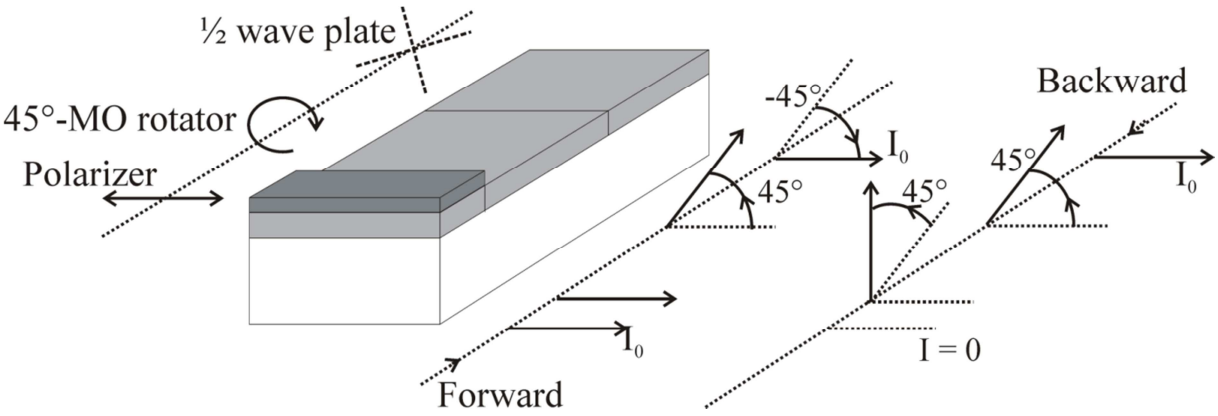

Figure I-3: Schematic view of an integrated optical isolator based on a non-reciprocal Faraday Rotator

In order to obtain an isolation function, the MO rotator is combined with a half wave plate whose axis is oriented at 22.5 ° of the plane, and a polarizer. In the forward direction, after travelling through the polarizer, the MO rotator and the half wave plate, the polarisation direction of the wave remains the same, so it can propagate. But in the backward direction, the direction of the polarization is perpendicular to the direction of the polarizer. Thus, it is blocked and the propagation is stopped.

This schematic example shows that to construct an optical isolator, it is required to have a magneto-optical Faraday rotator with an angle of 45 °. But there is another factor which can also affect the efficiency of the device: the absorption (α). Generally, it is mainly due to the magnetic material. For this reason, a merit factor has been defined also. This is a quality factor of the material and expresses the competition between the rotation and the absorption of the material [11]. It is given by:

$$M(°) = \frac{\theta_F\left(\frac{°}{cm}\right)}{\alpha\left(\frac{1}{cm}\right)} \qquad \text{Eq I.6}$$

α is the absorption coefficient which can be determinated from the Beer-Lambert's law:

$$I = I_0 e^{-\alpha h} \qquad \text{Eq I.7}$$

where is I is the transmitted electromagnetic (EM) wave, I_0 is the incident EM wave and h is the path length or the thickness of the material.

These two parameters, the Faraday rotation and the merit factor are suitable to determine the ability of a material to be used in devices, such as optical isolators.

I.1.2. Isolator realizations

In current optical networks, optical isolators only exist through bulk forms with magneto-optical rotators, which are mainly made of ferrimagnetic garnet oxide like Yttrium Iron Garnet (YIG), or Bismuth/Cerium-substituted Yttrium Iron Garnet (Bi/Ce:YIG), depending on the working wavelength. This kind of material possesses a Faraday rotation, which can reach 3000 °·cm^{-1} associated with a merit factor about 2500 °. Thus, the isolators on the market have very interesting properties with an isolation ratio about 40 dB and insertion loss about 0.4 dB [12].

But, telecommunication systems need to develop new optical integrated elements, which are faster, more compact, cheaper and easy to realize. So, an integrated version of the optical isolator is highly desirable. Such a device should, at least, possess an extinction ratio about 20

dB, with insertion loss lower than 1 dB. However, in spite of their interesting magneto-optical properties, the garnet oxide class of material cannot be grown on the common substrates used for optoelectronics or photonic integrated circuits [13]. Indeed, the crystallization of this garnet requires an annealing temperature as high as 700 °C to be magneto active [14]. This temperature is evidently not compatible with integrated optical technologies. Furthermore, in order to respect the lattice distance, these materials have to be grown on gadolinium gallium garnet substrate (GGG) which is not commonly used in integrated optics technologies based on III-V semiconductor, silica, silicon and polymer.

To overcome this problem, researchers have worked on two different approaches. The first deals with the hybrid integration of YIG on planar lightwave circuits by insertion in grooves [15] or by direct bonding on classical substrate: silicon [16] or glass [17] for example. The second is the development of novel magneto-optical materials compatible with classical technologies. This second approach has led to the development of different interesting materials in view of an integration on optical chip.

I.2. Magneto-optical materials for integration

Different kinds of materials have been developed this last decade in order to obtain the well desired integrated optical isolators. To compare their properties, the merit factor of several magneto-optical materials used in integrated devices or candidate for such devices are gathered in ***Table I-1***. To our knowledge, the larger value has been obtained by Zayets *et al.* [18] in a diluted magnetic semiconductor CdMnTe at a wavelength of 730 nm on GaAs substrate. Shimizu *et al.* [19,20], and Lesuffeur *et al.* [21] have used materials with low figure of merit, but they were then associated to an active core waveguide and the whole structure works as a non-reciprocal loss/gain propagator on semiconductor substrate. Among the materials offering an operation about 1550 nm telecommunication wavelength, the larger values have been obtained with Fe-doped InGaAsP (540 °) on semiconductor substrate also, and with Ce-substituted-YIG on Gadolinium Gallium Garnet substrate (2500 °). The difficulty to use YIG-derived films in integrated devices has already been pointed out.

Material	M (°)	λ (nm)	Substrate	Authors
CdMnTe	4000	730	GaAs	Zayets *et al.* [18]
InAlAs:MnAs	0,26	1550	InP	Shimizu *et al.*[19]
GaAs:MnAs	0,08	1550	GaAs	Shimizu *et al.*[20]
$Co_{50}Fe_{50}$	1,38	1300	GaAs	Lesuffleur *et al.*[21]
γ-Fe_2O_3 as NP	0,3-0,8	633	Glass	Royer *et al.*[22]
YIG	44	1550	GGG	Huang *et al.*[23]
Bi:YbIG	130	1550	GGG	Huang *et al.*[23]
Ce:YIG	2500	1550	GGG	Shintaku *et al.*[24]
Fe:InGaAsP	540	1550	InP	Zaman *et al.*[25]
Fe-doped $SrTiO_3$	4,7	1550	$LaAlO_3$	Kim *et al.*[26]
Fe_3O_4 NP PMMA	2,1	980	Polymer	Lopez-Santiago *et al.*[27]

Table I-1: Merit factor of different magneto-optical materials. The operating wavelength is given in each case

Finally, this table shows that lots of efforts have been made to develop novel magneto-optical materials compatible with semiconductor technologies. Nevertheless, no approach has allowed the full integration of a magneto-optical material with glass waveguides which cannot stand temperature higher than 500 °C. The laboratory LT2C has initiated several years ago a "composite "approach that is compatible with glass technology.

I.3. The "composite" approach

This approach consists of fabricating magneto-optical material via sol-gel method. Fully crystallized magnetic nanoparticles are dispersed in a sol-gel liquid preparation in order to obtain, after the gelation, a magneto-optical silica-based material [1,11]. The obtained matrix possesses low refractive index (about 1.5) which can make easier the interconnection with an optical fiber (***Figure I-4***). As illustrated on ***Figure I-4a)*** the size of the magnetic nanoparticles is about 10 nm, which is low enough to avoid any large scattering by a laser beam. The SEM picture reported on ***Figure I-4b)*** illustrates the good random distribution of the particles in the matrix without any aggregates. That is due to the good compatibility of the magnetic fluid used for the doping with the sol gel initial solution.

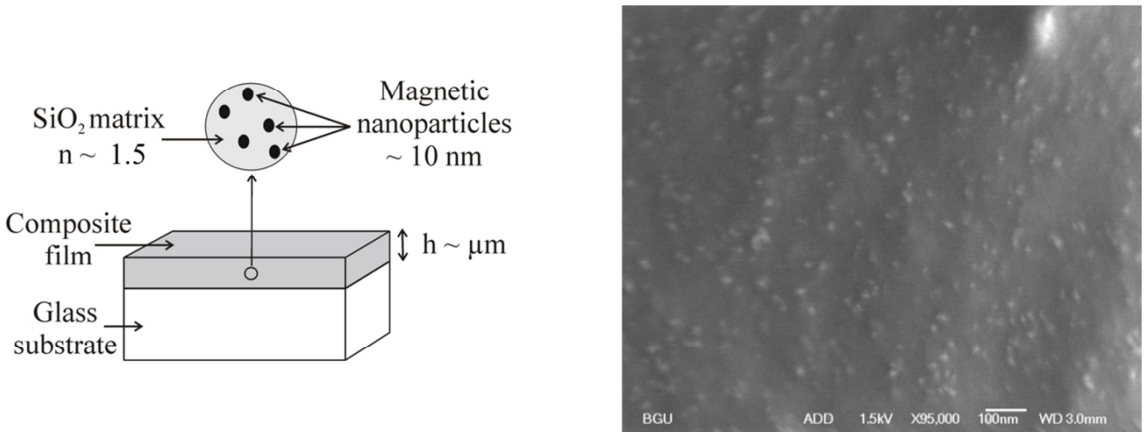

Figure I-4: Schematic view of a composite film made of magnetic nanoparticles embedded in a silica matrix. This film can easily be coated on glass substrate (a); SEM picture of such a composite film which proves the random distribution of nanoparticles inside the matrix without any aggregates (b)

Cobalt-ferrite nanoparticles were mainly [9,11,28] used to develop this magneto-optical composite material. ***Figure I-5*** and ***Figure I-6*** show the transmittance curve and the Faraday rotation of such cobalt-ferrite nanoparticles dispersion as a function of the wavelength. The transmittance of this composite material sharply increases at 700 nm until 1050 nm, after the transmittance remains stable.

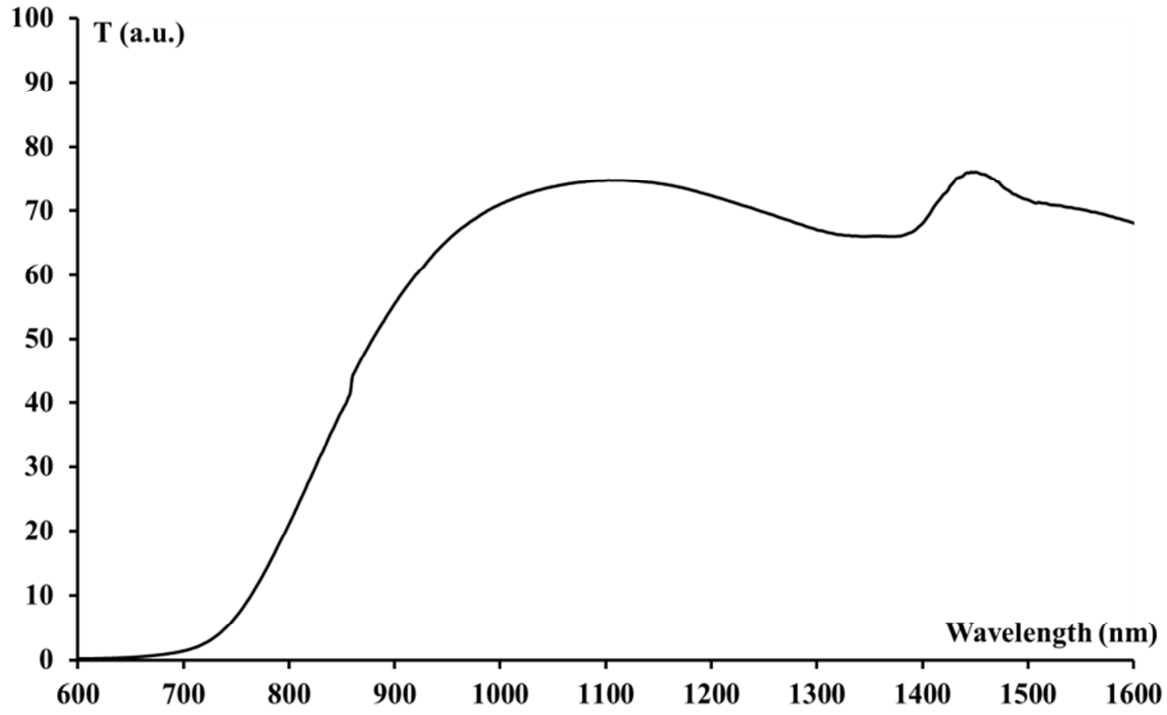

Figure I-5: Transmittance spectrum of cobalt-ferrite dispersion, where the optical path is 1 mm (volume fraction=0.15 %)

The specific Faraday rotation, plotted for 1% volume fraction (VF), shows general behavior which is similar to those reported by Donatini *et al.* [29] on various types of cobalt-ferrite ferrofluids. One can observe two resonance peaks: one narrow at 750 nm (θ_F ~ 220°·cm^{-1}) and a broader about 1550 nm (θ_F ~ 200 °·cm^{-1}). Thus, the following studies presented in this work concerning the magneto-optical activity of films or silica opals doped by cobalt-ferrite nanoparticles will focus on these spectral areas. One attractive point is that the magnitude of the Faraday effect (200 °·cm^{-1} at 1550 nm, VF=1 %) is close to that of YIG [23]. Of course, substituted YIG would give a larger effect (500°·cm^{-1} at 1550 nm) [23]. But it seems interesting to note that even if we use composite material with a small amount of magnetic nanoparticles, the same order of effect than that of a classical magneto-optical material can be obtained.

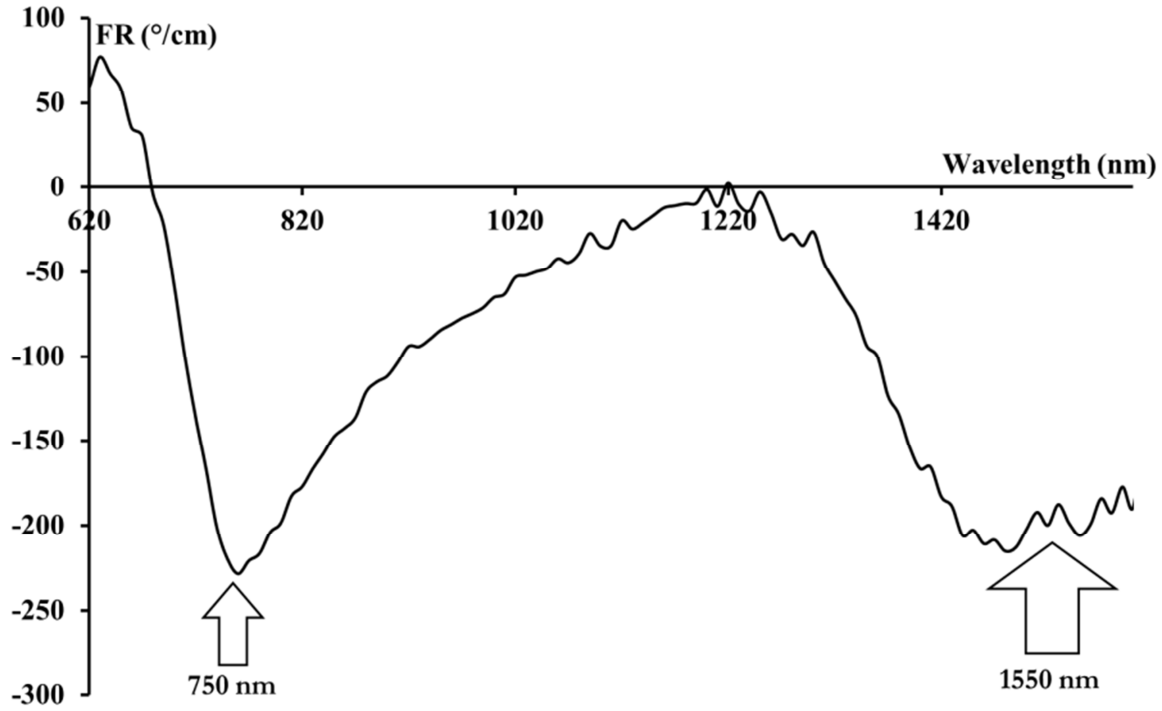

Figure I-6: Faraday rotation curve of Cobalt-ferrite dispersion as a function of the wavelength, where the optical path is 1 mm (volume fraction=1 %)

To compare the magneto-optical quality of such a material with those presented in the previous paragraph, the relevant parameter is the merit factor. At a given wavelength, the specific Faraday rotation θ_F and the absorption α ($\alpha = -ln(T)$) are both proportional to the nanoparticles volume fraction [30]. Based on the data of ***Figure I-5*** and ***Figure I-6***, we have plotted on ***Figure I-7*** the merit factor of the composite material as a function of the

wavelength. It presents wide peaks near 900 nm and 1550 nm, which correspond respectively to a merit factor of about 2 ° and 7 °. The larger value obtained in the 1550 nm area combines its location in the transparency band of the material (***Figure I-5***) with one of the resonance peaks of the Faraday effect (***Figure I-6***).

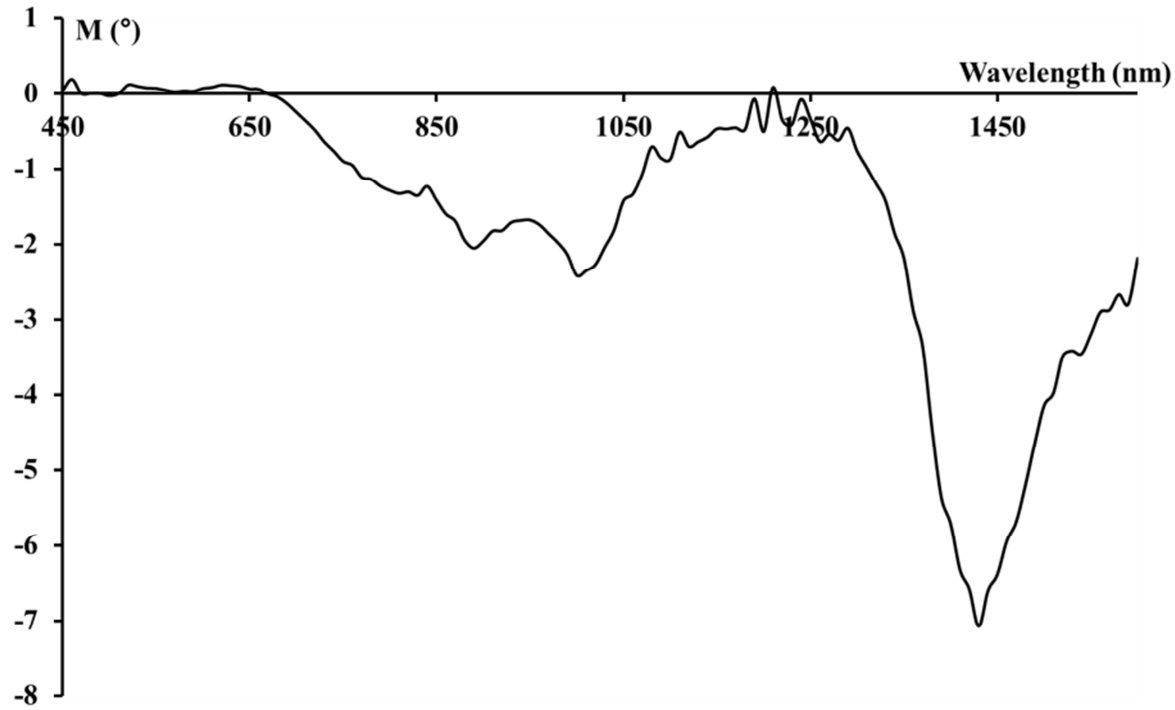

Figure I-7: Merit factor of Cobalt-ferrite dispersion as a function of the wavelength

The best value obtained about 1450 nm stands in the area of the telecommunications wavelength. One should note that this value can reach 10 ° if the size of the nanoparticles is reduced from 9 to 6 nm [11]. Compared to those presented in ***Table I-1***, such a composite material has a middle value of merit factor. Thus, one can summarize its properties as follows:

- Good Faraday rotation: 200 °·cm^{-1} for 1 % of nanoparticles
- Best operating wavelength in telecommunication window :~ 1500 nm
- Middle value of merit factor : ~10 °
- Full compatibility with glass waveguides (certainly also with silicon or polymer)

Based on these interesting properties and in order to go further on the integration of this material, the laboratory LT2C has decided to adapt the composite approach with the glass ion-exchanged integrated technology, which is one of the prominent technologies in the field of integrated optics. This is the subject of on-going works with IMEP-LAHC in Grenoble.

The goal is to realize integrated magneto-optical mode converter. On ***Figure I-8a)*** is reported a schematic of such a structure. A composite film is coated on an ion exchanged glass waveguide. Due to the low thermal treatment (~ 100 °C) required by the composite, no damage is made on the guide during the process.

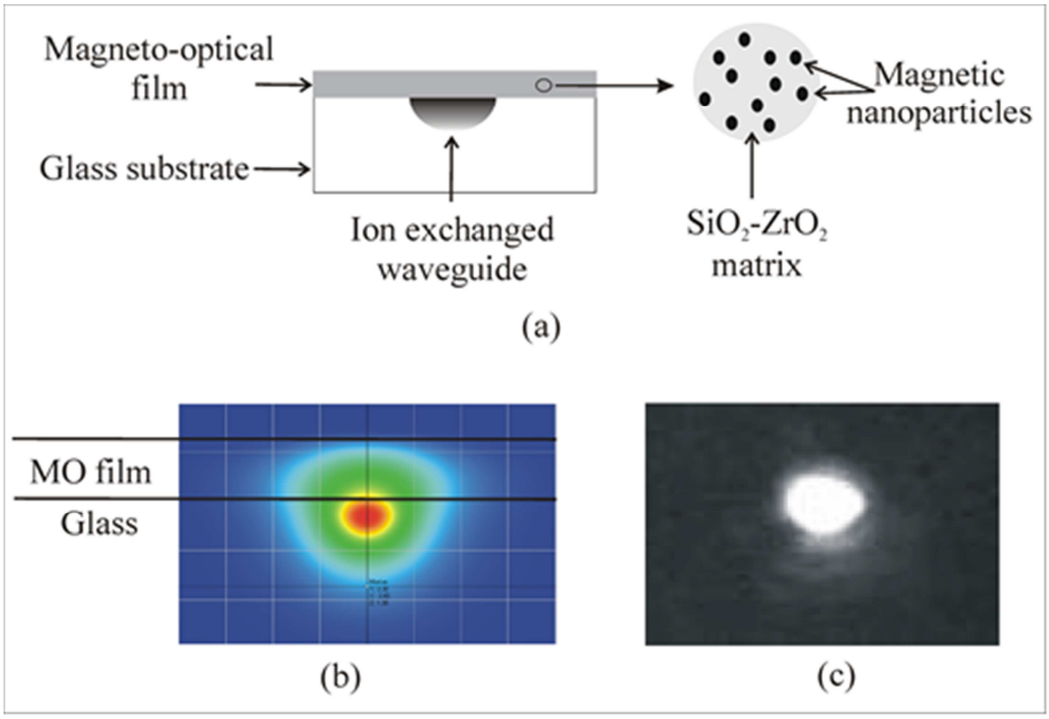

Figure I-8: Schematic of a hybrid magneto-optical waveguide. A composite film is coated on an ion-exchanged waveguide (a). Field distribution in such a structure obtained using a semi-vectorial mode solver (Optiwave) (b) Output light intensity of the hybrid structure measured at 1550 nm (c)

The refractive indexes of the composite film and the guide have very close to each other leading to a light propagation at the interface between these two elements (***Figure I-8b)***). The output light intensity reported on ***Figure I-8c)*** shows that such a hybrid structure can be used as a waveguide. It demonstrates the ability of the composite film to be integrated in Photonics Lightwave Circuits [31]. Furthermore, a magneto-optical mode conversion has been demonstrated in such a structure[32].

The properties gathered in this paragraph evidence that the composite approach developed by the LT2C is promising in terms of integration and polarization conversion. The remaining drawback is the quite low merit factor of the material. In order to increase this value, it appears interesting to use a magneto-photonic crystal obtained through a periodic

patterning of the core material. The Laboratory LT2C has chosen, through this study, to apply the composite approach to the realization of 3D magneto-photonic crystals. Thus, the next section is concerned by a state of the art of these structures.

I.4. Magneto-Photonic Crystals (MPC) structures

As it will be detailed later in the text, magneto-photonic crystals have demonstrated, for about a decade, their ability to enhance the magneto-optical effects in the area of their photonic band gap. Moreover, some groups have also shown that it seems possible to improve the magneto-optical merit factor. This is for example the work of Khartsev *et al.* [33], who show an increase of such a factor from 25 to 33 °, in a one dimensional magneto-photonic crystal based on YIG multilayer. Even if, to our knowledge, there is no demonstration of such an increase on 3 dimensional structure, the use of a 3D periodic arrangement looks promising.

To understand the behavior of photonic crystals and the role played by a periodic arrangement on the magneto-optical properties, this paragraph is concerned by a state of the art of these structures.

Among all the demonstration one can find in the literature, some of these crystals have another major advantage for us: they can be elaborated by the sol-gel method. Thus we will mainly focus on them in this review.

The Photonic crystals can be classified like one, two and three dimensional crystals, due to the $\hat{\varepsilon}$ dielectric constant which spatially varies periodically in one, two or three specific directions, respectively.

One dimensional photonic crystal, which is shown on ***Figure I-9***, is the multilayer structure, where the layers of high and low refractive index materials are alternated.

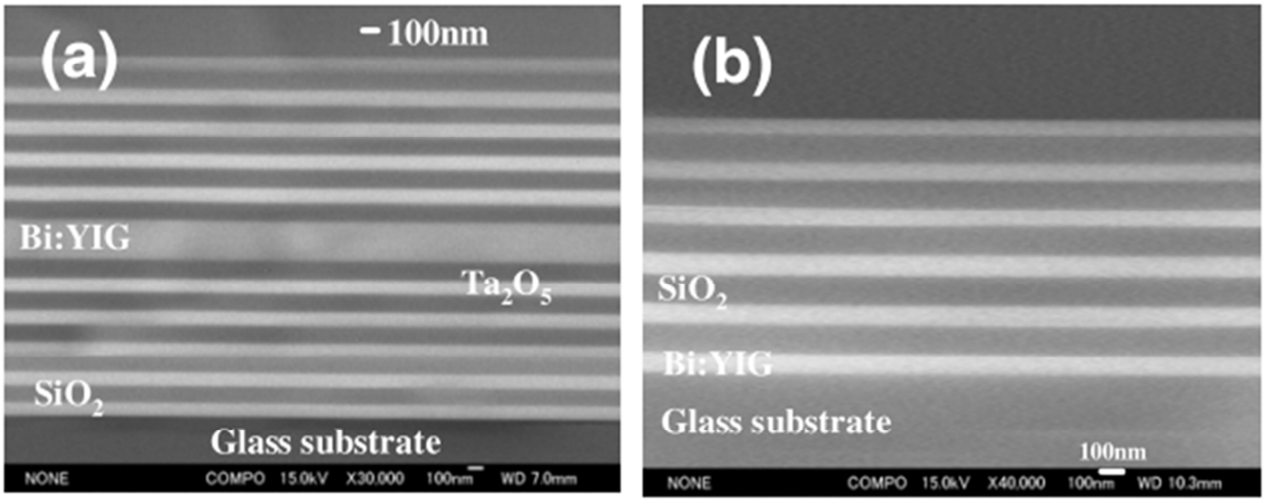

Figure I-9: One dimensional photonic crystal structure from the work of Inoue et al.[34] *a) "microcavity" structure ($Ta_2O_5/SiO_2)_5$/Bi:YIG/($SiO_2/Ta_2O_5)_5$ and b) "periodic structure (Bi:YIG/$SiO_2)_5$/Bi:YIG (Bismuth-substituted yttrium iron garnet)*

The structure of air and magnetic rods or columns called 2D photonic crystals (***Figure I-10***), where the axes of the intersections of the two present materials gives the two dimensional arrangement in a perpendicular plane.

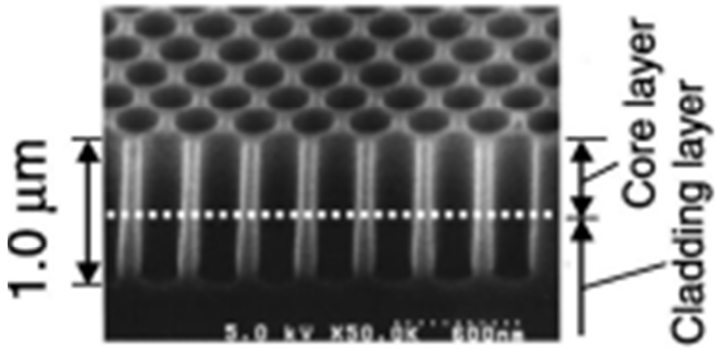

Figure I-10: Two dimensional photonic crystal made by Sugimoto et al.[35]

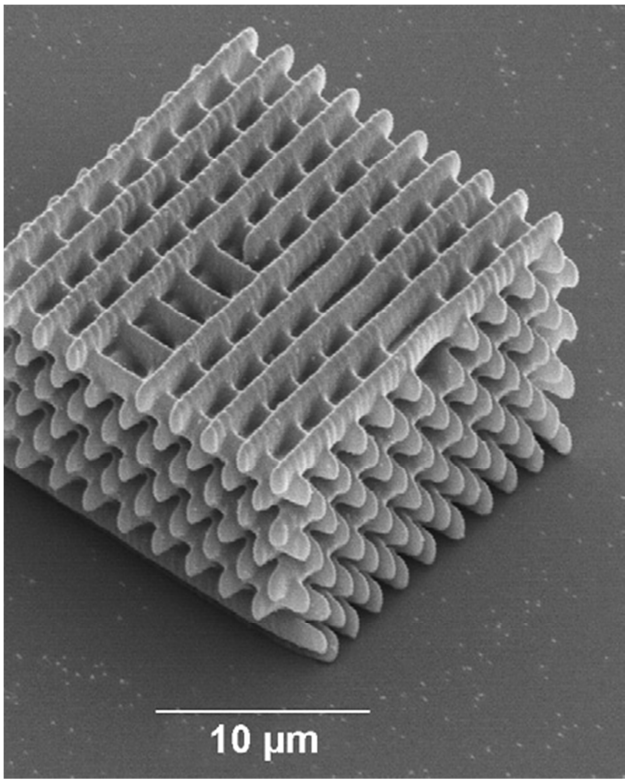

Figure I-11: Three dimensional photonic crystal, "Yablonite" [36]

For three dimensional structure (***Figure I-11***) the dielectric constant varies periodically in three different spatial directions.

I.4.1. Photonic Crystals (PC)

The property of the PC, such as the wavelength control, makes this material very important in the telecommunications. ***Table I-2*** presents the most important results of three dimensional photonic crystals.

The first thought of such a three dimensional structure was made in 1987. Yablonovitch tried to find the solution for the lasing threshold of the semiconductor lasers, where spontaneous emission causes important loss. With minimizing loss his problem can be solved. This idea leads to the PBG material, which can be used to control the light, and in the chosen path the propagation can be enhanced, but in the unwanted range, it can be decreased. The result was a theoretical assumption for a creation of 3D face center cubic (fcc) structure with the length scale ~ 1000 times larger than the atoms. He determinated that, with the large refractive index difference, the PBG can appear between the density states. He noted that the

realization, such a 3D arrangement, needs further development, and proposed the assay of the PBG made by polystyrene spheres or hexagonal-closed-packed glass [37].

A few month later, Sajeev John published an article, where he was constructing a new hypothesis of the three dimensional photonic superlattice with the moderate disorder to develop strong photon localization in non-dissipative materials with real dielectric constant all over the structure [38]. It was the first time that three dimensional structure with an appropriate refractive index constant was given as a solution for the light wave localization problem.

Successful realization of three dimensional direct opal of monodisperse silica spheres was made by sedimentation method by Lopez *et al.* [39]. Optical transmission was made in normal incidence using 535 down to 220 nm diameter size of the spheres. With growing diameter size the PBG was tuned to the higher wavelength region. Using the well-chosen diameter size of the spheres, the whole visible and infrared spectrum could be covered (***Figure I-12***).

$$\lambda_c = 2d_i cos\theta \sqrt{\frac{2}{3}\left[f_{sph}n_{sph}^2 + (1 - f_{sph})n_{bg}^2\right]} \qquad \text{Eq I.8}$$

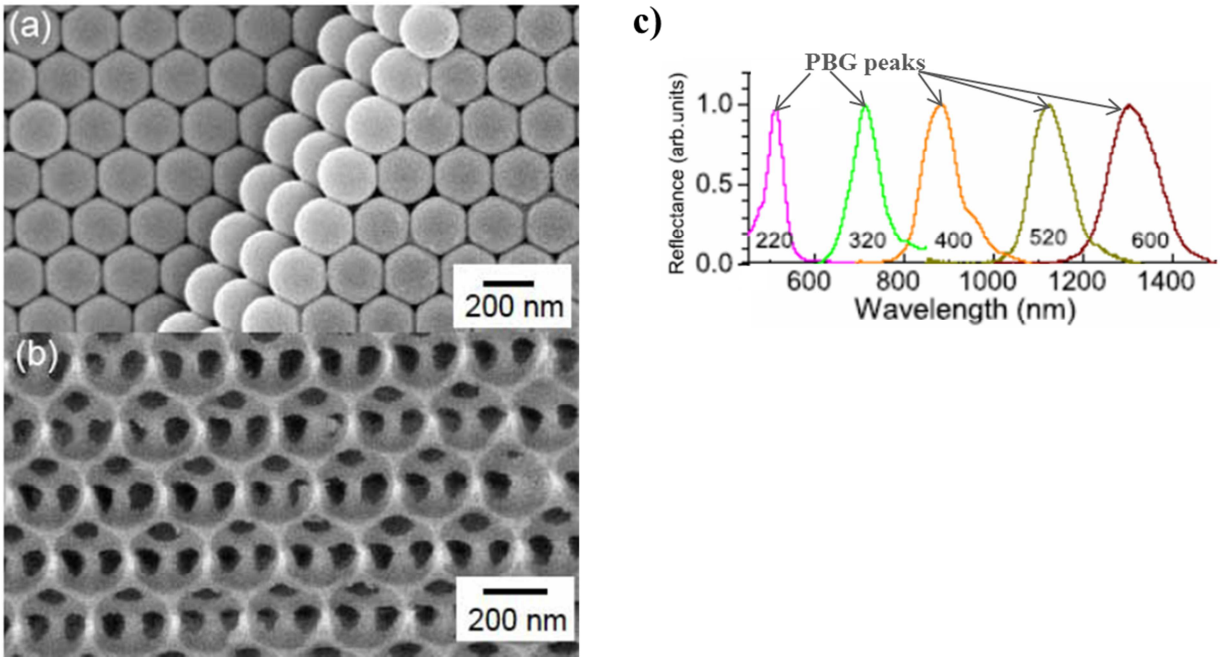

Figure I-12: Example of 3D a) direct opal, b) inverse opal and photonic band gap (PBG) peaks made by 220, 320, 400, 520, 600 nm diameter size of polystyrene spheres from the work of Nishijima et al.[7]

In the Bragg law the λ_c means the position of the band gap, f_{sph} is the filling factor of the polystyrene spheres, n_{sph} is the refractive index of the spheres and n_{bg} is the background refractive index. Fitting the measured interplanar space value (d_i) into the Bragg law (Eq. I.8) (distance between the crystalline planes), it was determinated as $d_i = 0.816 \cdot d_{sph}$, where d_{sph} is the diameter of the spheres. The refracted index was calculated in the same way too, and found equal to n_{sph}=1.349, which is extremely close to the theoretical value n_{sph}=1.348. The incidence varying from 0 ° to 50 ° the transmittance spectrum was observed as a function of the wavelength using the direct opal with 440 nm diameter spheres. Two PBG was found in the wavelength spectrum, which belongs to the 220 and 111 crystalline planes. At normal incidence the PBG of 220 plane was placed at 525 nm and in the case of 111 plane the PBG was found at 957.5 nm. While the incidence increase, due to the Bragg law, the position of the PBG tunes to the shorter wavelength.

Ye *et al.* [40] reported self-assembly polystyrene direct opal growing on glass substrate by vertical deposition (VD) method using different temperature. They obtained high quality 3D fcc structure and showed that the use of a bit higher temperature than the room temperature can increase the quality of the fcc direct opal structure, because the spheres have more kinetic energy to found the possible lattice sites. They also noted that too high temperature, because of the too fast evaporation, leads to the faster flux, faster structuration and drying tension. In this way, the arrangement possesses more cracks, defects of vacancies. They state that with increasing disorder the width of PBG is increasing too.

Concerning the structure of opals, Lopez *et al.* [41] also characterized polystyrene direct opal structure. The opal was created with the vertical deposition method at 45 °C. The 3D fcc structure was studied with monochromatic laser beam (0 °). The result of the fcc structure gives hexagonal diffraction patterns. This work proves high quality organization of the 3D PC realization by vertical deposition.

Nishijima *et al.* [7] fabricated and characterized three dimensional direct and invers opals using sol-gel process. This work is interesting for us, because the sol-gel process used in this work is close to the one used by the LT2C to realize the composite matrix. The polystyrene direct opals were created by a centrifugation method. The inverse opals were made by the impregnation of tetraethyl-orthosilicate sol. After the drying process, the polystyrene balls were eliminated from the structure by ethyl-acetate. The thickness was about 100 µm. The relative mismatch between the measured and the theoretical value of the PBG position for

direct opal is 1 % and for inverse opal it is 4-7 %. This last mismatch percentage is due to the shrinkage of the drying sol.

Author	3D Structure and materials	Optical results
Yablonovitch[37] 1987	First 3D fcc structure	Theoretical prevision of wavelight control
John[38] 1987	3D photonic superlattice	Hypotheses for wavelight control
Lopez[39]	3D direct opal of monodisperse silica spheres	Φ= 440 nm PBG=957.5 nm Wavelight control in the order of the Bragg law
Ye[40]	Self-assembly polystyrene opal growing on glass substrate	Vertical deposition method Φ= 310 nm PBG=675 nm
Lopez[41]	3D polystyrene direct opal	Vertical deposition method; Structure study through visible light diffraction
Nishijima[7]	3D polystyrene direct opal → 3D TEOS inverse opal	Direct opal realization : Centrifugation ; Inverse opal realization: Sol-gel method

Table I-2: 3D PC materials and results

I.4.2. Magneto-Photonic Crystals (MPC)

When one of the constitutive elements of photonic crystals has magnetic behavior, the whole structure is called Magneto-photonic crystals (MPC). It can demonstrate unique optical and magneto-optical properties [2].

a) 1D MPCs

1D PCs are known as multilayer film. Several works came to light with the idea of photonic crystal structure which contains magnetic materials for optical applications.

This multilayer structure supports strongly localized mode of light within a PBG originating from the Fabry-Perot structure, made by dielectric material of low and high refractive index. This type of system has been well examined in the last decade (***Table I-3***). Employing periodically alternating materials with large refractive index difference one can reach large width PBG a strong localization of the light in the magnetic defect layer [11].

For example, Faraday rotation enhancement of one dimensional magnetic "periodic" structure was calculated by Levy *et al.* [3]. The structure was created by alternating isotropic material (n_L=1.926) and magnetic material (n_M=2.21). The PBG was positioned at 1550 nm and the film thickness was less than 40 µm. They built two different structure, one with three-phase shifts like $(LM)^a(ML)^b(LM)^b(ML)^a$, and one with four-phase shifts $(LM)^a(ML)^b(LM)^c(ML)^b(LM)^a$, where a, b and c are integers of the repetition of (LM) layer couple. If they use for a=14 and b=29, the Faraday rotation value was found at -45° for the three-defect (***Figure I-13***) structure. Same polarization rotation result was calculated in the case of four-defect structure composed by a=12, b=26 and c=28 repetitions.

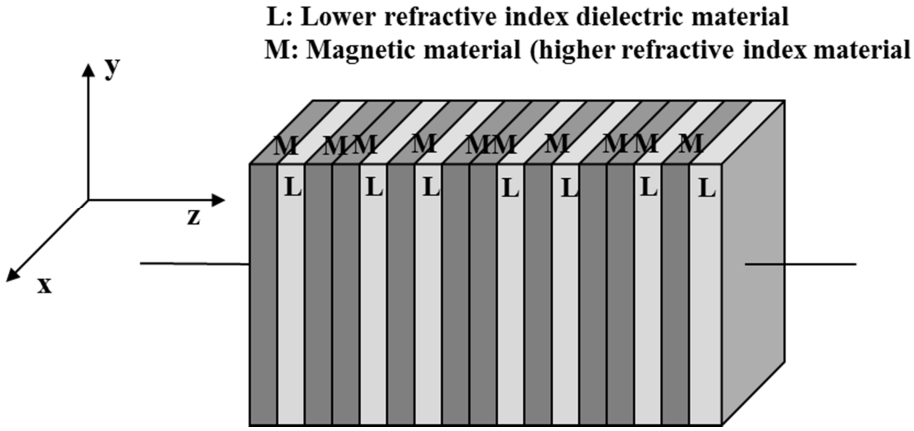

Figure I-13: Three defect one dimensional multilayer structure

Inoue *et al*. realized two different types of 1D magneto-photonic crystal: the "periodic" and the "microcavity" (MC) structure. In this case, Ta_2O_5 was used as high refractive index material, and SiO_2 as low refractive index material. Bi: YIG was centered in the middle, like a magneto optical defect ***Figure I-14a***. For MC structure where the thickness of the Bi:YIG is 230 nm, they have resonant transmission in the middle of the PBG at ~650 nm with a Faraday rotation of ~ -0.80 ° [2]. They reported the modification of the Faraday rotation due to the change of the electronic structure, comparing to Bi:YIG single layer film. They observes the PBG position of the "periodic" structure between 750-1050 nm, where Faraday rotation enhancement was found at the edge of the photonic band gap.

The calculation for multilayer system with the cobalt magnetic layer was made by Inoue *et al.* [5]. The "microcavity" system was alternated like $(SiO_2/SiN)^4/Co/(SiN/SiO_2)^4$, where the thickness of the SiO_2, SiN and the Co layer was 111, 88.5 and 50 nm, respectively. In the

reflectance curve a PBG was present about 780 nm, and a large Kerr rotation enhancement appears in this band gap.

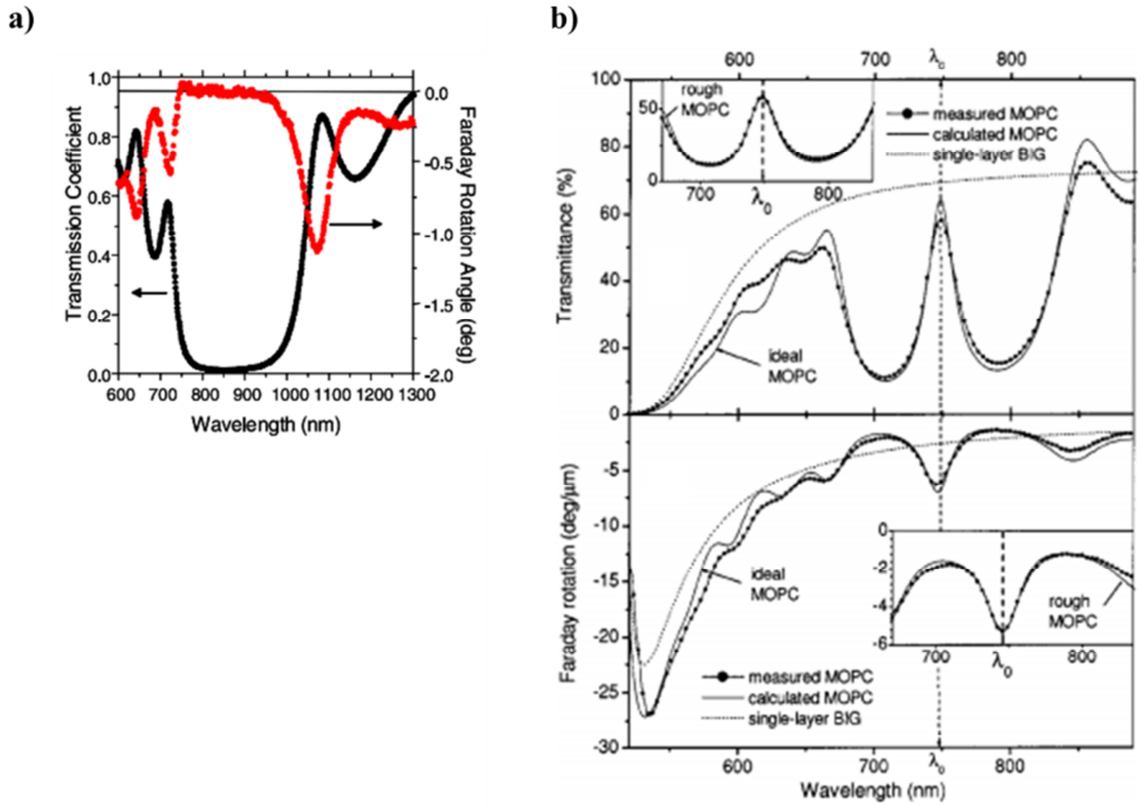

Figure I-14: Examples of transmittance and Faraday rotation curves as a function of the wavelength of a) "periodic" and of b) "microcavity" structure a) figure is made by alternating $(SiO_2/Bi:YIG)_5$ made by Inoue et al. [2]; b figure shows BIG monolayer and $(BIG/YIG)_4BIG_4/YIG/BIG)_4$ multilayer made by Kahl et al. [6]

Kahl *et al.* [6] also realized a "microcavity" structure by alternating $(BIG/YIG)^4BIG^4/(YIG/BIG)^4$ on GGG substrate. The centered layer thickness is 670 nm. They compared the multilayer systems with equivalent BIG monolayer. The multilayer structure shows BPG at 748 nm, where the reached Faraday rotation value is -6.3 $°\cdot\mu m^{-1}$ compared to -2.6 $°\cdot\mu m^{-1}$ for the monolayer (see on ***Figure I-14b)***. With such an arrangement the merit factor is enhancement from 7 ° to 11.6 °.

Another interesting idea has been proposed by Grishin *et al.* [42], who calculated Transmittance and Faraday rotation of Er-doped $[Bi_3Fe_5O_{12}/Gd_3Ga_5O_{12}]^m$ (BIG) garnet . The photonic band gap was centered at 1532 nm. Intensive luminescence is necessary to get optical gain media. BIG layers were designed with the thickness of 3.7 μm at 1532 nm. Without pumping, the Faraday rotation was -11.1 °. With pumping this value increased until -45° with 128.6 μm thick $Bi_3Fe_5O_{12}$ garnet composite.

Author	1D Multilayer Structure and materials	Results
Levy[3]	Alternating isotropic and magnetic materials with 3 and 4 phase shifts	FR= -45 ° in both cases
Inoue[2]	« Microcavity » structure (Ta_2O_5/SiO_2)|Bi:YIG|(SiO_2/Ta_2O_5)	PBG= 650 nm FR=-0,80 °
Inoue[5]	"Microcavity" structure $(SiO_2/SiN)^4$ |Co| $(SiN/SiO_2)^4$	Kerr rotation enhancement in the PBG
Kahl[6]	$(BIG/YIG)^4BIG^4/YIG/BIG)^4$	PBG=748 nm, FR=-6.3 °•μm^{-1}
Grishin[42]	Er doped BIG garnet inside 1D MPC	With intensive luminescence pumping FR= -45 °

Table I-3: One dimensional magneto photonic crystal results

b) 2D MPCs

The activity on 2D magneto-photonic crystals is clearly less intensive than on 1D multilayer system. We can notice two kind of works. The first is based on the one dimensional patterning of magneto-optical YIG waveguide which result in 2D MPC. The studies of the group of Levy are very interesting [43] and are useful to realize sensors. The second is the study of full 2D photonic crystals, with a real 2D periodic variation of the permittivity. This is, for example, the work of Vanwolleghem *et al*. [44] who demonstrated the existence of unidirectional band gaps in magnetized 2D magneto-photonic crystals. The authors have designed a special geometrical symmetry of the elementary motifs which allows such a behavior.

c) 3D MPCs

Obviously, there is not a lot of demonstration of 3D magneto-photonic behavior. It seems that it is not so easy to obtain a 3D arrangement with the YIG which is the most common magneto-optical material. Thus, in the literature most of the 3D magnetic composite were made using silica opals. ***Table I-4*** lists the important optical results and material of three dimensional magneto photonic crystals.

SiO_2 opals-maghemite, -TGG and -Bi:YIG, three different, three dimensional immersed opals were made by the group of Inoue [2,45]. The volume fraction of the void was about 25 %. The PBGs were observed in the same position as the PBG of the direct SiO_2 opal, at ~590 nm using 300 nm diameter size of the SiO_2 artificial opal. They found that the absorption is

decreasing with the increasing magnetic volume fraction, because of the light absorption. The intensity of the PBG of the opal-magnetite composant was decreased compared to the pure opal sample. And they evidence a considerable change in the Faraday rotation spectrum inside the (111) photonic band gap.

Pavlov *et al.* [46] also worked with silica spheres-maghemite composites. Here the diameters of the spheres were 290 nm, the pore volume fraction were 20 % and 70 % of the maghemite and the silica spheres, respectively. The thickness of the composant was about 5 µm. The PBG in transmission was found at ~689 nm. Faraday rotation change was observed in the same place with the value about -0.1 °.

Koerdt *et al.* [47] has made silica opals with a diameter size of 260 and 275 nm and impregnated it with saturated glycerol solution of dysprosium-nitrate. They found the photonic stop gaps at 630 and 573 nm, respectively. A Faraday rotation change was achieved inside the PBG. The Faraday rotation outside the PBG follows the behavior of the liquid solution multiplied by its volume fraction.

Very recently, magnetic inverse opal was fabricated by Caicedo *et al.* [48]. Polystyrene self-assembly spheres were applied on a glass substrate on a use of vertical deposition. Then Al_2O_3 layers were grown by atomic layer deposition on the polystyrene spheres. The polystyrene spheres were eliminated from the Al_2O_3 structure with toluene. Finally, the holes were filled with Ni nanoparticles. Three types of inverse opal were made with 15, 8 nm and random diameter size of Nickel nanoparticles. The photonic band gap appeared in the case of the direct opal at ~537 nm, which was red shifted after the magnetic nanoparticles infiltration. The magnetic circular dichroism (MCD) showed two prominent shoulders at the edge of the PBG waverange. To our knowledge, and even if the effect is weak, it is the first experimental demonstration of a magneto-optical enhancement at the edge of the band gap in a 3D magneto-photonic crystal.

Author	3D Structures and materials	Optical results
Inoue[2,45]	**SiO_2 opal-maghemite** **SiO_2 opal-FGG** **SiO_2 opal-Bi:YIG**	**FR enhancement in the PBG**
Pavlov[46]	**Silica spheres maghemite**	**PBG=689 nm** **FR=-0.1 °**
Koerdt[47]	**Silica opals impregnated saturated glycerol of dysprosium-nitrate**	**PBG=630 and 573 nm** **FR inside the photonic band gap**
Caicedo[48]	**AL_2O_3 Inverse opals infiltrated with Ni nanoparticles**	**MCD band edge enhancement**

Table I-4: Three dimensional magneto photonic crystal results

I.5. Motivations, goals and research plan

As detailed in the first section, an integrated version of the optical isolator is highly desirable. But, the YIG or substituted YIG, which are the conventional materials used for such a device cannot be embedded by classical integrated technology.

Among the different novel magneto-optical materials which can be integrated the composite developed by the LT2C is promising because it combines a high value of the Faraday rotation at 1550 nm, with a full compatibility with, at least, the glass integrated technology. A hybrid magneto-optical converter are thus been demonstrated with an ion-exchanged glass waveguide. But, to improve the quality of the material, it seems relevant to increase its magneto-optical merit factor.

Several authors have demonstrated the ability of 1D magneto-photonic crystals to enhance the Faraday rotation in the area of their band-gap, and in some particular cases the merit factor also. Furthermore, the realization of 3D photonic crystals using a sol-gel approach is easily possible using polystyrene direct opals through a low annealing process.

The composite matrix developed by the LT2C being based on a sol-gel process with a starting solution doped by magnetic nanoparticles, the group has planned to realize 3D magneto-photonic crystals with polystyrene opals inverse by a doped sol-gel solution. The desirable final structure is given on ***Figure I-15***.

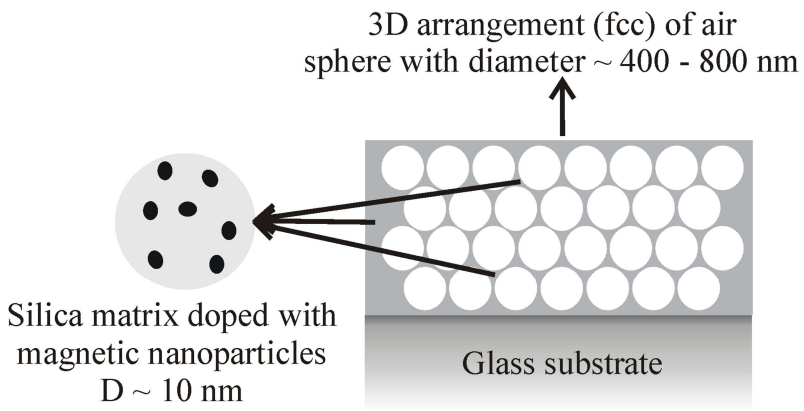

Figure I-15: Schematic of a 3D MPC based on a fcc arrangement of air spheres in a silica matrix doped by magnetic nanoparticles. Average size of nanoparticles and air spheres are given.

The crystal should consist of fcc arrangement of air spheres in a silica matrix doped by cobalt ferrite nanoparticles. The diameter of the sphere should be about 400-900 nm in order to work in the visible, near-infrared spectral range. The size of nanoparticles is about 10 nm, which is smaller than the spheres diameter.

Finally, the goals of this work can be resumed as:

- Check the ability of our composite matrix (n ~ 1.5) to work as a photonic crystals, and as a magneto-photonic crystals. That will be presented in the final sections of the 2nd chapter.
- Identify and develop the tools to elaborate and characterize direct and inverse opals and to move our doped sol gel preparation to an inversion of opals. (3rd chapter)
- Elaborate direct and inverse opals and study their optical properties and physical structure (4th chapter)
- Evidence the magneto-photonic behavior of these structures (4th chapter) and check their capacity to enhance the Faraday rotation and/or the merit factor.

II. CHAPITRE: Arrangement Periodique
(resumé francais)

Un des élément clé de ce travail est l'arrangement périodique d'un matériau, et son influence sur les propriétés optiques et magnéto-optiques de cette structure. Il est nécessaire de montrer comment une structure dite photonique peut jouer un rôle sur l'effet Faraday d'un point de vue théorique. Ainsi, des calculs sont effectués sur une structure 1D utilisant la méthode de matrice de transfert afin de montrer l'influence d'une organisation stricte dans un matériau sur la rotation Faraday.

La périodicité à l'échelle manométrique influence la propagation de la lumière qui obéit à des règles spécifiques dans les cristaux photoniques. Il est donc nécessaire d'utiliser un formalisme particulier pour comprendre et interpréter les propriétés des ondes se propageant.

Le comportement des photons dans les cristaux photoniques peut-être expliqué par le comportement des électrons dans les semi-conducteurs. Lorsqu'une structure est périodique et que cette périodicité correspond à la longueur d'onde du faisceau lumineux incident, la propagation de la lumière pour une gamme de longueur d'ondes est annulée et une bande interdite photonique (BIP) est créée. Une similitude entre la bande électronique interdite séparant la bande de valence de la bande de conduction, avec la bande interdite photonique est envisagée. Fondamentalement, les diagrammes de bande définissent les propriétés électriques et optiques des matériaux. Ces BIP, où les photons ne peuvent se propager, peuvent apparaître dans un système composé d'une alternance de couches de matériaux à indices de réfraction élevé et faible. A l'intérieur de ce gap photonique, la dissolution de l'onde transmise est le résultat d'interférences destructrices des ondes diffusées par les éléments de la structure périodique. Car dans une direction, si les ondes réfléchies sont en phase avec l'onde incidente, elles se recombinent et arrêtent la propagation, créant ainsi la BIP.

Une BIP apparaît aussi avec un organisation en 3D, par exemple avec un empilement structuré de billes, les indices de réfraction étant différents entre les billes et les interstices.

Les équations de Maxwell permettent de comprendre la propagation des ondes dans les couches et sont à la base de l'explication mathématique de ce phénomène. Ainsi, pour séparer la partie spatiale et temporelle des équations de Maxwell, l'analyse de Fourier a été utilisée. La résolution des équations des matrices permet d'obtenir la relation de dispersion $\omega - \vec{K}$, ce qui explique la propagation de la lumière dans les cristaux photoniques. Mais, en raison de la périodicité particulière des cristaux photoniques, un formalisme particulier est nécessaire. Ainsi, la transformation de Fourier et les fonctions de Bloch permettent d'obtenir les solutions de l'équation de Helmholtz. Pour arriver à la relation de dispersion $\omega - \vec{K}$, la structure du cristal photonique 3D est expliquée de façon mathématique en utilisant la physique du solide. Ainsi pour le matériau étudié possédant une structure cubique face centrée, le réseau réciproque (octaèdre tronqué) permet de réaliser ces calculs.

Les calculs permettent de mettre en évidence que le changement du paramètre de maille de la structure modifie la position de la BIP.

Une telle relation est calculée dans un système 1D simple et ensuite appliquée au matériau magnétique étudié pour montrer comment une structure photonique intervient sur l'effet Faraday. Dans un premier temps, cette simulation montre que l'utilisation d'une structure périodique (alternance de couches d'indices de réfraction différents), interrompt le spectre $\omega - \vec{K}$, pour une certaine gamme de fréquences. Une BIP est créée autour de cette discontinuité et à la limite de celle-ci, la courbe de le relation de dispersion s'aplatit. Cela indique un ralentissement de la vitesse de propagation de l'énergie électromagnétique. Dans un second temps, une structure identique est utilisée, mais la couche haut indice de réfraction est maintenant magnétique. Pour étudier l'effet Faraday la relation de dispersion $\omega - \vec{K}$, a été calculée, en utilisant un tenseur diélectrique. Les calculs ont montré qu'une grande différence du vecteur d'onde est observée à proximité de la BIP. Ainsi, la rotation Faraday est plus importante aux bords de la BIP pour un réseau périodiques de Bragg.

Dans l'étude précédente, le matériau était transparent et son tenseur de permittivité constant. Afin de prévoir le comportement du facteur de mérite, la simulation a utilisé l'indice de réfraction et le tenseur de permittivité d'une monocouche de ferrite de cobalt. Ces calculs prennent en compte l'absorption de la matière et la dispersion du tenseur de permittivité. Des simulations ont été réalisées pour deux structures différentes dénommée "microcavité" et "périodique". La première est une alternance de couches d'indice de réfraction faible et élevé, avec au centre de cette structure une couche de matériau magnétique. La seconde est une

structure identique sans la couche magnétique. Ces deux structures ne présentent pas le même comportement spectral. A 1550 nm, dans le cas de la structure "microcavité" la simulation montre que la rotation Faraday augmente dans le centre de la BIP, alors, que cette augmentation se produit aux bords de la BIP, dans le cas de la structure "périodique". Le résultat le plus important est que nous pouvons également augmenter le facteur de mérite deux fois en utilisant de structure périodique.

II. CHAPTER: Periodic Arrangement

This chapter presents the influence of a periodic arrangement on the optical and magneto-optical properties of a material or a structure. The first part deals with a theoretical analysis of the propagation of light in periodic system, through the resolution of the master equation. It is shown how such equation can be solved using Bloch modes in order to obtain an $\omega - \vec{K}$ dispersion relation. Such a relation is calculated in a simple 1D system and then applied to our magnetic material to show how a photonic structure can play a role of the Faraday effect.

In the second part of this chapter, calculations are made on 1D structure using 4x4 matrix transfer method. These calculations take into account the absorption of the material and the dispersion of the permittivity tensor element. The results are related to the Faraday rotation and merit factor behavior.

II.1. General properties of Photonic Crystals

The propagation of light obeys to specific rules in photonic crystals because of their periodicity at the wavelength scale. It is thus necessary to use a specific formalism to understand and interpret the properties of the propagating waves. But, firstly, it seems relevant to focus on the interest of such photonic crystals.

II.1.1. What is the interest of Photonic Crystals?

Information technology has been built with the ability to control the flow of electrons in semiconductor. In photonic telecommunication systems PCs promise to give us similar control of photon through their periodic optical nanostructure. Their properties and their capacity of the wavelength control is explained in this part.

When the periodicity of the structure is commensurable with the wavelength of the light, there are certain wavelength ranges (PBGs), which prohibit the propagation of the light. The photon behavior in PC is analog to the electron one in semiconductor.

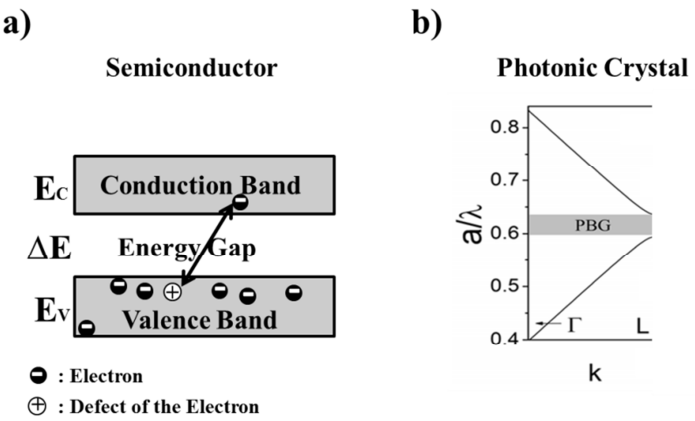

Figure II-1: Simplified energy band diagram of a) semiconductors and of b) photonic crystal

Basically, band diagram defines electric and optical properties. ***Figure II-1*** shows two different kind of energy band diagram, one represents a semiconductor material and the second the photonic crystal. In ***Figure II-1a)***, in the case of the semiconductor, there are different energy levels of the electrons. The conduction and the valence band are shown on a simplified band diagram, which are non-forbidden energy levels for electrons. Between the valence and conduction energy band there is the forbidden state, called energy gap, where electrons cannot be present. ***Figure II-1b)*** shows an example graph of $\omega - \vec{K}$ dispersion relation simulation of a three dimensional photonic crystal. Y axis represents ω as $a \cdot \lambda^{-1}$ ($\frac{a}{\lambda} = \frac{a \cdot \omega \cdot n}{2\pi \cdot c}$, where n is the refractive index of the material, a is the lattice parameter and c is the velocity of the light in vacuum), and X axis is the K wavevector. It can be drawn a parallel between the two graphs, because ω angular frequency is proportional with the energy ($E = \hbar\omega$). In ***Figure II-1b)*** the energy gap appears as in semiconductor, and it is called a photonic band gap. Thus, the photonic crystal behaves like a semiconductor material, with an energy gap. Such PBG, where the photons cannot propagate, can appear in a multilayers system alternated by high and low refractive index material.

Inside the photonic band gap, the attenuation of the transmitted wave is a result of destructive interferences among the waves scattered by the periodic structure in the forward direction. Such phenomenon is schematically given on ***Figure II-2*** and ***Figure II-4***.

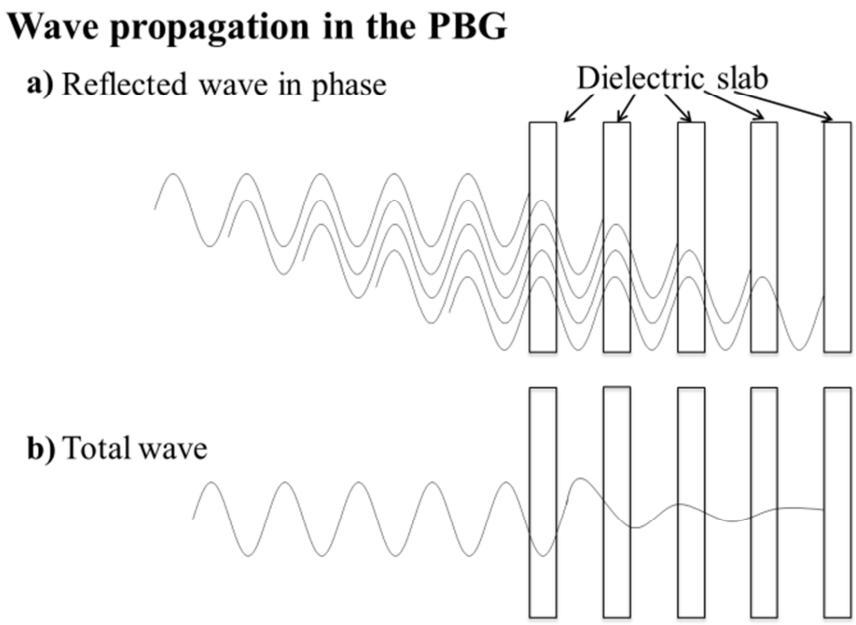

Figure II-2: Explication of the wave propagation in phase in the PBG in one dimensional photonic crystal

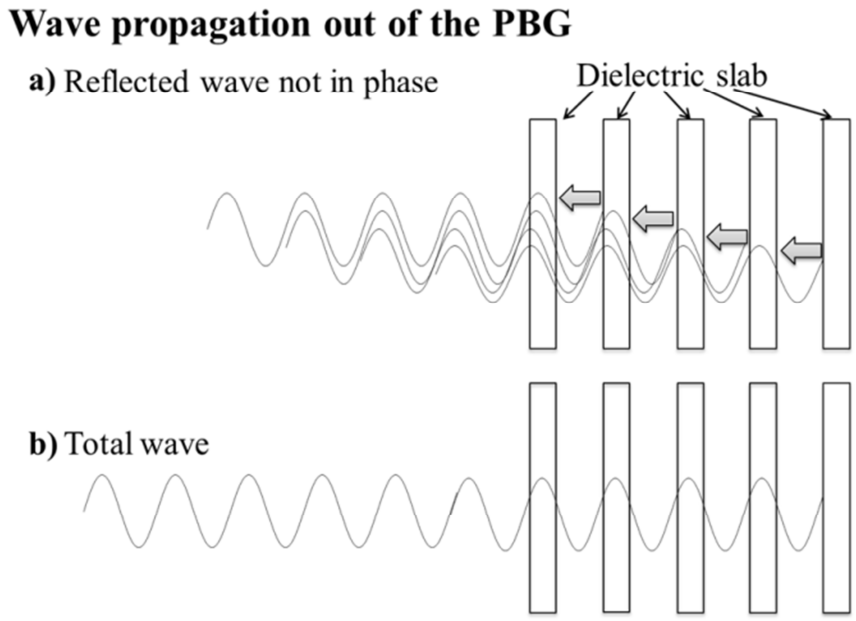

Figure II-3: Explication of the wave propagation out of phase in the PBG in one dimensional photonic crystal

When the incident wave impinges the one dimensional photonic crystal, the wave is partially reflected by each crystal layers. A high reflectivity is obtained when the partial reflected waves are all in phase. This wave cannot get through the material (***Figure II-2***). On the opposite, ***Figure II-3*** shows the case of propagation through the multilayer slabs, where

the reflected waves are not in phase. Although, the light brooks reflexions from each slab, they cannot cancel each other. In this way the light can propagate through the material.

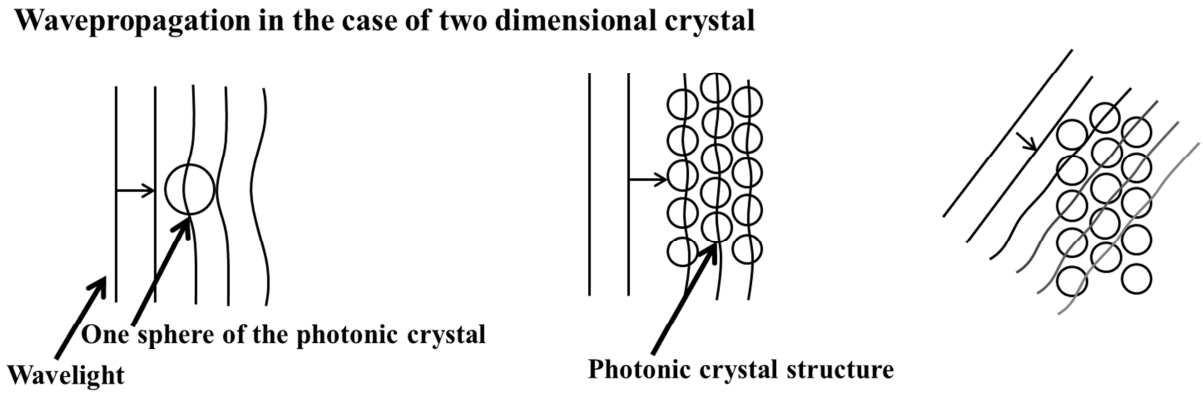

Figure II-4: Explication of the wave propagation for photonic crystal

Figure II-4 shows the propagation in two dimensional photonic crystal. Every unit of this structure reflects back the propagation wave, in all direction of the incident wave. If in one direction, the reflected waves are in phase, they recombine and stop the propagation to create BPG [49].

II.1.2. Propagation of light in Photonics Crystals: from Maxwell equation to "Master equation"

This part presents the electromagnetic Master equation. Two coupled time varying vector fields, the electric and the magnetic fields are used to interpret the electromagnetic phenomenas. The Maxwell's microscopic equations for continuous media without free charges or currents are given by [50–52]:

$$\nabla \vec{D}(\vec{r},t) = 0 \qquad \text{Eq II.1}$$

$$\nabla \times \vec{E}(\vec{r},t) = -\frac{\partial}{\partial t}\vec{B}(\vec{r},t) \qquad \text{Eq II.2}$$

$$\nabla \vec{B}(\vec{r},t) = 0 \qquad \text{Eq II.3}$$

$$\nabla \times \vec{H}(\vec{r},t) - \frac{\partial}{\partial t}\vec{D}(\vec{r},t) = 0 \qquad \text{Eq II.4}$$

Where $\vec{D}$ is the electric displacement field, $\vec{\mathrm{B}}$ is the magnetic induction field, $\vec{\mathrm{E}}$ is the macroscopic electric field and $\vec{\mathrm{H}}$ is the macroscopic magnetic field.

For PC who contains no magnetic materials in the structure, the magnetic induction field and the dielectric displacement constant are equal to that in free space:

$$\vec{B}(\vec{r},t) = \mu_0 \vec{H}(\vec{r},t) \qquad \text{Eq II.5}$$

$$\vec{D}(\vec{r},t) = \varepsilon_0 \varepsilon_r(\vec{r})\vec{E}(\vec{r},t) \qquad \text{Eq II.6}$$

where ε_0 is the free space dielectric constant and $\varepsilon_r(\vec{r})$ is the relative dielectric constant for photonic crystal. The dielectric constant is real, isotropic and perfectly periodic with the spatial coordinate $\vec{r}$ and does not depend on frequency.

To separate the spatial and time dependence part of the Maxwell's equations we have to expand the fields into harmonic modes. So, Fourier analysis has been invited to create the appropriate combination of the harmonic modes:

$$\vec{H}(\vec{r},t) = \vec{H}(\vec{r})e^{-i\omega t} \qquad \text{Eq II.7}$$

$$\vec{E}(\vec{r},t) = \vec{E}(\vec{r})e^{-i\omega t} \qquad \text{Eq II.8}$$

The results for these curl relation using (Eq II.7) and (Eq II-8) equations into (Eq II-2) and (Eq II.4) are:

$$\nabla \times \vec{E}(\vec{r}) - i\omega\mu_0 \vec{H}(\vec{r}) = 0 \qquad \text{Eq II.9}$$

$$\nabla \times \vec{H}(\vec{r}) + i\omega\varepsilon_0\varepsilon_r \vec{E}(\vec{r}) = 0 \qquad \text{Eq II.10}$$

After dividing the (Eq II-10) relation by ε_r, then curl it and finally use the (Eq II-9) equation to eliminate $\vec{E}(\vec{r})$, the result is the "Master equation" or Helmholtz equation:

$$\nabla \times \left(\frac{1}{\varepsilon_r} \nabla \times \vec{H}(\vec{r})\right) = \left(\frac{\omega}{c}\right)^2 \vec{H}(\vec{r}) \qquad \text{Eq II.11}$$

With the similar procedure $\vec{E}(\vec{r})$ can also be determinated from Eq.II.9 and 10, and it results the following equation:

$$\nabla \times \nabla \times \vec{E}(\vec{r}) = \left(\frac{\omega}{c}\right)^2 \varepsilon(\vec{r})\, \vec{E}(\vec{r}) \qquad \text{Eq II.12}$$

where $c = \frac{1}{\sqrt{\varepsilon_0 \mu_0}} = 299.79 \cdot 10^6\ m \cdot s^{-1}$ is the vacuum speed of light.

The resolution of the "Master equation" gives the $\omega - \vec{K}$ dispersion relation, which fully explains the light propagation in the photonic crystal. But, due to the special periodicity of the crystal, such resolution needs to use a special formalism. Thus, in the next part Fourier transformation method and Bloch functions are detailed in order to obtain the solutions of the Helmholtz equation.

II.1.3. Reciprocal lattice and Brillouin zone

To determinate the $\omega - \vec{K}$ dispersion relation, the structure of the three dimensional photonic crystal has to be explained in a mathematical way.

In the solid state physics the primitive translation vector or primitive vector signifies the presents of the periodicity. This means that any two points in space like r and r' are the same for all values of the integers of m_1, m_2 and m_3. In a periodic medium, in one, two and three dimension the space is generated by three primary translation vectors on the lattice like a_1, a_2 and a_3. Each primary translation vector belongs to the directional axes x, y ,z. In this way r' is expressed as:

$$\overrightarrow{r'} = \vec{r} + m_1\vec{a}_1 + m_2\vec{a}_2 + m_3\vec{a}_3 \qquad \text{Eq II.13}$$

where $\vec{R} = m_1\vec{a}_1 + m_2\vec{a}_2 + m_3\vec{a}_3$ is the lattice translation vector.

For three dimensional periodic structure as face-center-cubic (diamond) lattice, the primitive cell is an off-axis cubic. These cubic axes are the primitive vectors which determinate the

lattice unit cell. With the repetition of the crystal translation operations the unit cell fills the whole crystal space.

Fourier transformation of the lattice points forms another set of points called reciprocal lattice. This is the sum of the components in Fourier space, where the spatial properties of the crystal structure can be determinated. Due to the strict periodicity of the physical properties, like permittivity $\hat{\varepsilon}(\vec{r})$, are invariant to the translation by $\vec{r}$, so:

$$\hat{\varepsilon}\left(\vec{r}+\vec{R}\right)=\hat{\varepsilon}(\vec{r}) \qquad \text{Eq II.14}$$

To expand this periodic property in three dimension, its Fourier series have to written as:

$$\varepsilon(\vec{r})=\sum_{G}\varepsilon_{G}\exp(-j\vec{G}\cdot\vec{r}) \qquad \text{Eq II.15}$$

where $\vec{G}=n_1\vec{g}_1+n_2\vec{g}_2+n_3\vec{g}_3$ is the reciprocal lattice vector determinated by g_1, g_2 and g_3 primitive vectors and n_1, n_2 and n_3 integers.

The fundamental vectors for reciprocal space are:

$$g_1=2\pi\frac{a_2\times a_3}{a_1\cdot a_2\times a_3} \qquad \text{Eq II.16}$$

$$g_2=2\pi\frac{a_3\times a_1}{a_1\cdot a_2\times a_3} \qquad \text{Eq II.17}$$

$$g_3=2\pi\frac{a_1\times a_2}{a_1\cdot a_2\times a_3} \qquad \text{Eq II.18}$$

Because g_1 is orthogonal to a_2 and a_3 but inversely proportional to a_1,

$$g_1 \cdot a_2 = 0 \qquad \text{Eq II.19}$$

and

$$g_1 \cdot a_3 = 0 \qquad \text{Eq II.20}$$

but

$$g_1 \cdot a_1 = 2\pi \qquad \text{Eq II.21}$$

In a similar way, g_2 is orthogonal to a_1 and a_3 but inversely proportional to a_2, and g_3 is orthogonal to a_1 and a_2 but inversely proportional to a_3. In this way, $G \cdot R = 2\pi$.

For three dimensional face-centered-cubic (fcc) photonic crystal structure the form of the reciprocal lattice is a truncated octahedron:

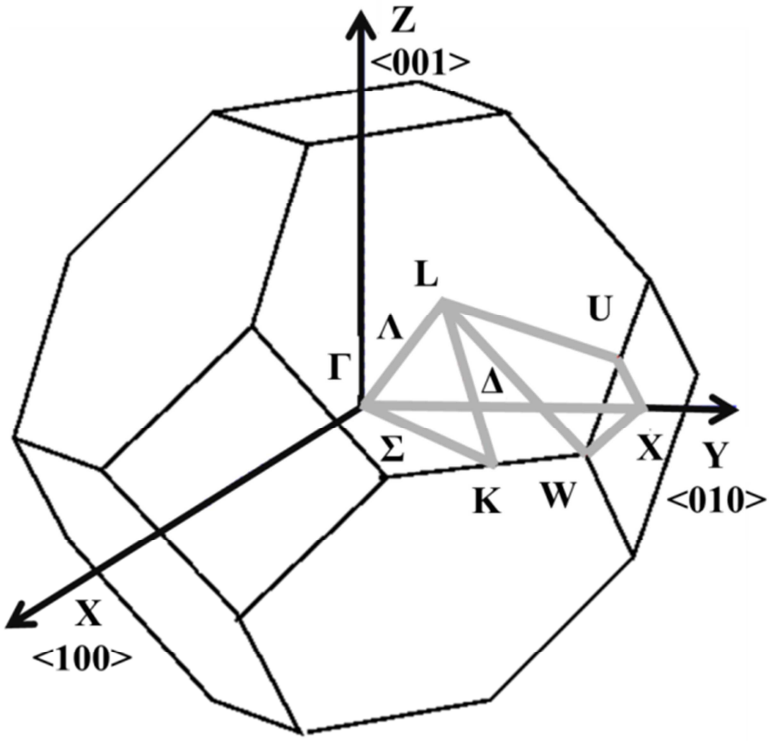

Figure II-5: Brillouin zone of the fcc structure

Figure II-5 shows the Brillouin zone of the fcc (diamond) structure, where the points with high symmetry are signed with the standard crystal of solid physics notations.

The First Brillouin zone is defined as a primitive cell of the reciprocal lattice. For fcc structure the First Brillouin zone is centered on a reciprocal point which is bounded to planes that cut in half the reciprocal lattice vectors.

The behavior of the wave in the strictly periodic medium can be defined by the solutions of the Bloch function in a First Brillouin zone.

II.1.4. Bloch mode

The shape of the wave modes for 3D periodic medium does not change under a translation by the $\vec{R}$ lattice vector, because the physical properties of the crystal are invariant. The Floquet-Bloch theorem states that the eigenfunction for such a system may be written as the product of a plane wave envelope function and a periodic function. The Bloch form of these modes is:

$$p_K(\vec{r})\exp(-j\vec{K}\cdot\vec{r}) \qquad \text{Eq II.22}$$

$$\vec{p}_{n\vec{K}}(\vec{r}) = \vec{p}_{n\vec{K}}(\vec{r}+\vec{R}), \qquad \vec{r}\in R \qquad \text{Eq II.23}$$

Where $p_K(\vec{r})$ is a periodic function for three dimension, $\vec{K}$ is the Bloch wavevector and $\exp(-j\vec{K}\cdot\vec{r})$ is the form of the harmonic function.

The Bloch functions generalize the familiar plane-wave on homogeneous media on a base of infinitesimal and discrete translation symmetry. With the boundary conditions ($\nabla\cdot\{\varepsilon_r\vec{E}(\vec{r},t)\}=0$), (Eq II.1, Eq II.3) of primitive cell, the solution can be expected as infinite with discretely spaced eigenvalues.

In this way for all modes the consideration of the value of $\vec{K}$ is sufficient in the Brillouin zone.

Based on this formalism, and especially the Bloch mode, two kind of method can be used to obtain the dispersion relation from the Helmoltz equation:

- The first is based on expanding the periodic function $\eta(\vec{r})$ of the medium and the periodic function $p_K(\vec{r})$ of the Bloch modes in Fourier series and converting Helmoltz equation into a set of algebraic equations. This method will be resumed in paragraph II.1.5 for 3D crystals

- The second approach is applicable to layered media with planar boundaries. It is based on the matrix propagation method of layered media [53]. Il will be used in paragraph II.1.6 for 1D crystal.

II.1.5. Dispersion relation for 3D crystals

$\omega - \vec{K}$ dispersion relation shows the propagation properties in the material. The ω range without corresponding $\vec{K}$ vectors define a photonic band gap.

To build the $\omega - \vec{K}$ dispersion relation for the modes the Bloch wavevector $\vec{K}$ are obtained by solving the Helmholtz equation like:

$$\nabla \times \left[\eta(\vec{r})\nabla \times \vec{H}\right] = \frac{\omega^2}{c_0^2}\vec{H} \qquad \text{Eq II.24}$$

where c_0 is the velocity of the light in free space and the impermeability is $\eta(\vec{r}) = \frac{\varepsilon_0}{\varepsilon(\vec{r})}$ ($\frac{\varepsilon_0}{\varepsilon(\vec{r})} = \frac{1}{\varepsilon_r(\vec{r})}$, where ε_0 is the vacuum permittivity, $\varepsilon(\vec{r})$ is the complex absolute permittivity and $\varepsilon_r(\vec{r})$ is the relative permittivity.

$\omega - \vec{K}$ is a periodic function with multiple values of $\vec{K}$ on a g periodic function ($g = \frac{2\pi}{a}$), generally plotted on a Brillouin zone [53].

In three dimension Fourier method is used to solve the Helmholtz equation for the determination of the $\omega - \vec{K}$ dispersion.

Because the impermeability $\eta(\vec{r})$ is periodic with the period of a, the Fourier series can be written as:

$$\eta(\vec{r}) = \sum_G \eta_G exp(-j\vec{G}\cdot\vec{r}) \qquad \text{Eq II.25}$$

where the reciprocal lattice vector is given like:

$$\vec{G} = n_1 g_1 + n_2 g_2 + n_1 g_1 \qquad \text{Eq II.26}$$

where g_1, g_2 and g_3 primitive vectors and n_1, n_2 and n_3 integers.

Expanding the $p_K(\vec{r})$ periodic function of Bloch wave into a 3D Fourier series gives:

$$p_{\vec{K}}(\vec{r}) = \sum_G C_G \exp(-j\vec{G}\cdot\vec{r}) \qquad \text{Eq II.27}$$

The generalization of the Bloch wave from the Helmholtz equation to get the magnetic field vector $H(\vec{r})$ is like:

$$H(\vec{r}) = p_K(\vec{r})\exp\left(-j\vec{K}\cdot\vec{r}\right)\hat{e} = \sum_G \eta_G exp\left[-j(\vec{K}+\vec{G})\cdot\vec{r}\right]\hat{e} \qquad \text{Eq II.28}$$

where $\hat{e}$ is a unit vector in the direction of the polarization.

The solution of the eigenvalue problem of "Master equation" for three dimensional periodic medium is:

$$\sum_{G'} F_{GG'}C_{G'} = \frac{\omega^2}{c_0^2}C_G, \text{ where } F_{GG'} = \left[\left(\vec{K}+\vec{G}\right)\times\hat{e}\right]\times\left[\left(\vec{K}+\overrightarrow{G'}\right)\times\hat{e}\right]\eta_{G-G'} \qquad \text{Eq II.29}$$

where $F_{GG'}$ is a Hermetian matrix and $C_{G'}$ is the Fourier coefficient. $\overrightarrow{G'} = mg$ which m (m=0, ±1, ±2, …) contributes to the optical wave-harmonic of spatial frequency. In the last equation $\eta(\vec{r})$ is real: $\eta_{G-G'} = \eta^*_{G'-G}$. This result explains that for each $\vec{K}$ Bloch wavevector the $\frac{\omega^2}{c_0^2}$ eigenvalues give multiple ω values.

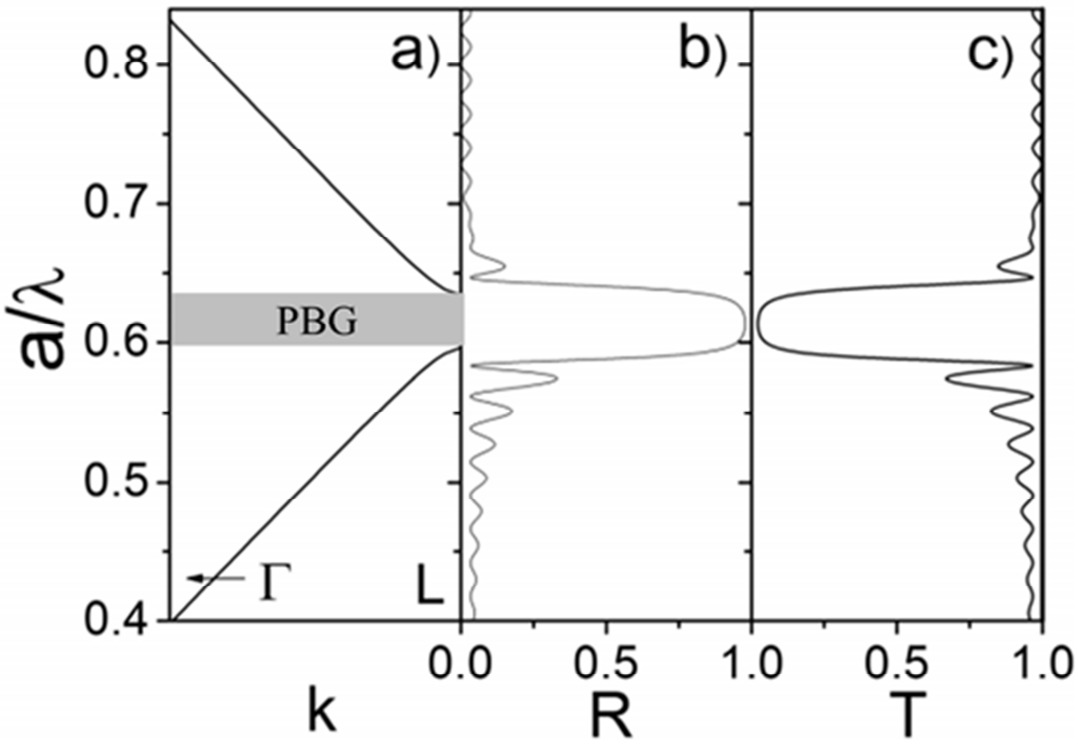

Figure II-6: a) Calculated dispersion relation of infinite polystyrene direct opal in the direction of ΓL (normal incident on the 111 planes parallel to the surface) b) and c) simulation curves show the reflectance and transmittance spectrum of a direct opal with 25 layers. (The calculations were made by Lopez et al. [54]*)*

Figure II-6 shows an example of the calculated three dimensional $\omega - \vec{K}$ dispersion relation. ***Figure II-6a)*** represents the lattice parameter divided by frequency ($a \cdot \lambda^{-1}$) values which is a type ω representation as a function of ΓL direction of wavevector ($\frac{a}{\lambda} = \frac{an\omega}{2\pi c}$, where n is the refractive index). ΓL direction is the 111 planes of the fcc opal, where the propagation of the light is perpendicular to this 111 planes. The dispersion relation curve split up at a certain ω angular frequency. If a lattice parameter changes it modifies the position of the PBG. Thus, the position of the photonic band gap, i.e. the propagation, can be controlled by changing the periodicity.

In the same place, where the bang gap is ***Figure II-6b)*** the reflectance and ***Figure II-6c)*** the transmittance presents a maximum and a minimum, respectively.

II.1.6. 1D dispersion relation

In this part, the calculation of the $\omega - \vec{K}$ dispersion relation of a 1D photonic crystal is presented. It was calculated in the case of "periodic" structure, which alternates a high refractive index layer (n_H=1.5; d_H=258 nm) with the low refractive index layer (n_L=1; d_L=387 nm), see ***Figure II-7***. The high index is close to that of the composite material and the low is that of air. The idea is to make a calculation on a structure which is close to the MPCs experimentally made in this project. The central Bragg wavelength (λ_C) of the photonic crystal is fixed to 1550 nm. It is linked to the thickness layer by: $h_i = \frac{\lambda_C}{4n_i}$.

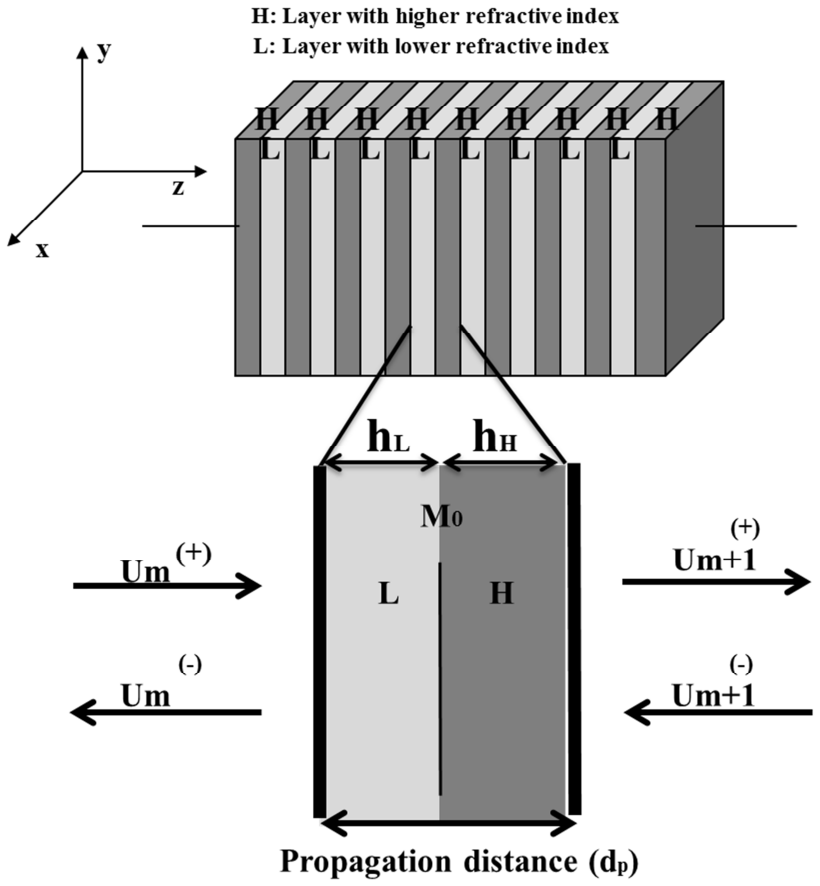

Figure II-7: Wave-transfer matrix representation

The matrix propagation method was used to determinate such $\omega - \vec{K}$ dispersion relation. ***Figure II-7*** represents a wave-transfer matrix for periodic slabs. If at the initial z position ($z=md_p$, where d_p is the propagation distance and m is the unit cell) the m-th

amplitude $\left\{U_m^{(\pm)}\right\}$ is known, the amplitude at the other position can be determinated by using the corresponding wave-transfer matrix.

$$\begin{bmatrix} U_{m+1}^{(+)} \\ U_{m+1}^{(-)} \end{bmatrix} = M_0 \begin{bmatrix} U_m^{(+)} \\ U_m^{(-)} \end{bmatrix}, m = 1, 2 \dots \quad \text{Eq II.30}$$

with

$$M_0 = \begin{bmatrix} \frac{1}{t^*} & \frac{r}{t} \\ \frac{r^*}{t^*} & \frac{1}{t} \end{bmatrix} \quad \text{Eq II.31}$$

where t and r are the complex amplitude of the transmittance ($T = |t^2|$) and reflectance ($R = |r^2|$)^2 [53].

Based on Bloch theory, in a periodic medium the self-reproducing wave can be written as:

$$\begin{bmatrix} U_{m+1}^{(+)} \\ U_{m+1}^{(-)} \end{bmatrix} = e^{-j\Phi} \begin{bmatrix} U_m^{(+)} \\ U_m^{(-)} \end{bmatrix}, m = 1, 2 \dots \quad \text{Eq II.32}$$

where Φ Bloch phase can be determinated as a multiplication of K Bloch wavevector and d_p propagation distance:

$$\Phi = K d_p \quad \text{Eq II.33}$$

Using the M_0 wave transfer matrix, the eigenvalue problem can be written as:

$$M_0 \begin{bmatrix} U_0^{(+)} \\ U_0^{(-)} \end{bmatrix} = e^{-j\Phi} \begin{bmatrix} U_0^{(+)} \\ U_0^{(-)} \end{bmatrix} \quad \text{Eq II.34}$$

where $e^{-j\Phi}$denotes the eigenvalue and $U_0^{(\pm)}$ are the eigenvectors for infinite number of segments [53].

The eigenvalues are determined by equating the determinant of $M_0 - e^{-j\Phi} \cdot I$ to zero. It gives [53]:

$$\cos(Kd_p) = Re\left(\frac{1}{t}\right) \quad \text{Eq II.35}$$

Furthermore, the transmittance can be written as [53]:

$$Re\left\{\frac{1}{t}\right\} = \frac{(n_H + n_L)^2}{4n_H n_L} cos(\varphi_H + \varphi_L) - \frac{(n_H - n_L)^2}{4n_H n_L} cos(\varphi_H - \varphi_L) \quad \text{Eq II.36}$$

Thus, for an ω angular frequency, the K wavevector is the solution of the equation:

$$\cos(Kd_p) = \frac{(n_H + n_L)^2}{4n_H n_L} cos(\varphi_H + \varphi_L) - \frac{(n_H - n_L)^2}{4n_H n_L} cos(\varphi_H - \varphi_L) \quad \text{Eq II.37}$$

Where $\varphi_H = n_H \frac{\omega}{c} d_H$ and $\varphi_L = n_L \frac{\omega}{c} d_L$ are the phases of the two layer segments.

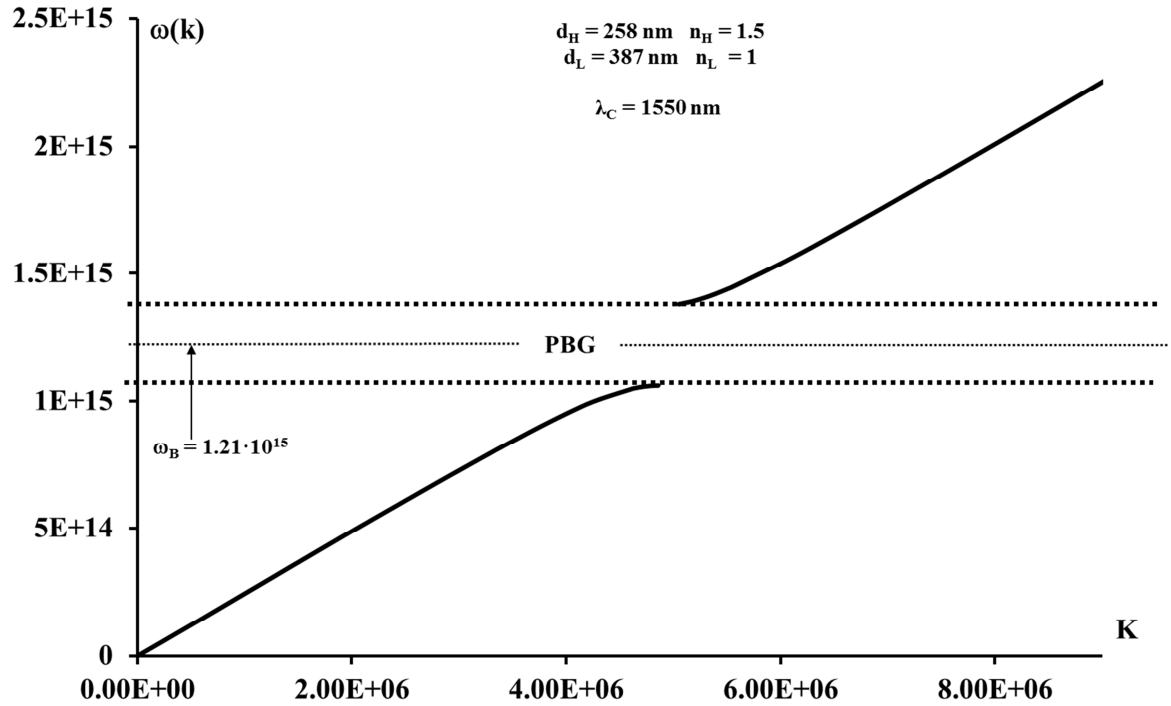

Figure II-8: Dispersion relation graph as a function of the wavevector (K) for "periodic" structure

Figure II-8 shows a graphical solution of this calculation in terms of ω(K) curves. This simulation proves that using periodic structure leads to $\omega - \vec{K}$ spectrum discontinues where the Eq. II-37 has no solution. A photonic band gap is created about this discontinuity and at

the boundary of this PBG the dispersion relation curve flattens. This indicates a slowing down of the electromagnetic energy propagation velocity.

II.2. Dispersion relation of 1D Magneto-Photonic Crystals

Based on the calculation detailled in the previous paragraph, the goal is now to study how a periodic arrangement can play a role on the Faraday effect.

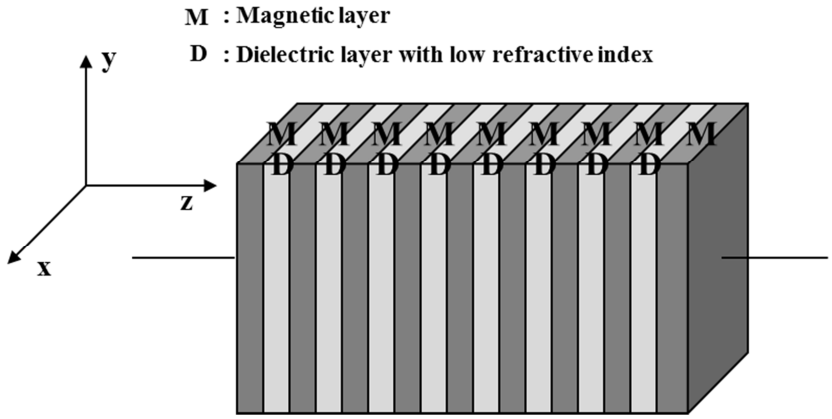

Figure II-9: Schema of the Bragg slab which was used for the calculation where the magnetic (M) and dielectric (D) layers are alternating

The structure is identical to the former one, but the high refractive index layer is now magnetic. To study the Faraday effect the ω(K) dispersion relation has been calculated, depending on the left and right circular vibration, which are the eigenpolarization in such material.

To determinate the left and right circular refractive index inside the magnetic layer, its dielectric tensor has to be invited from Eq.I-1, and using the diagonal and the appropriate off-diagonal elements of this dielectric tensor the left and right circular index can be written as:

$$n_L = \sqrt{\varepsilon_{xx} + \varepsilon_{xy}} \qquad \text{Eq II.38}$$

$$n_R = \sqrt{\varepsilon_{xx} - \varepsilon_{xy}} \qquad \text{Eq II.39}$$

The $n_L - n_R$ difference is the circular birefringence in the magnetic layer.

On ***Figure II-10*** the ω(K) relation for the left and right vibration with $\varepsilon_{xx} = 1.5^2$ and $\varepsilon_{xy} = 2.6 \cdot 10^{-4}$ are plotted. These values correspond to a composite material at a 1550 nm wavelength.

ε_{xy} being small compared to ε_{xx}, the two curves are quite superimposed. The inset of this figure zooms out the angular frequency as a function of the wavevector for the left and right circular vibration next to the PBG. The straight black and the dashed line present the curve of the right and left circular vibrations, respectively. Close to the BPG the (ΔK) wavevector difference between the K_R and K_L increases, because the two curves flattening.

On ***Figure II-11*** the ΔK $(K_R - K_L)$ circular wavevector difference is shown as a function of λ_0 (wavelength in vacuum: $\lambda = \frac{2\pi c}{\omega}$) for the above mentioned periodic structure (***Figure II-9***). It is obvious that the highest wavevector difference can be observed just close to the band gap. One should remind that, for the whole structure, the Faraday rotation emerges from the phase-shift of the left and right polarization of the output. This phase shift is due to the different propagation constant of the left and right polarizations and the Faraday rotation is proportional to the circular wavevector difference ΔK through:

$$\theta_F = \frac{\pi h}{\lambda} Re(K_R - K_L) \qquad \text{Eq II.40}$$

Thus, the biggest Faraday rotation can be predicted at the edge of the photonic band gap for periodic Bragg grating.

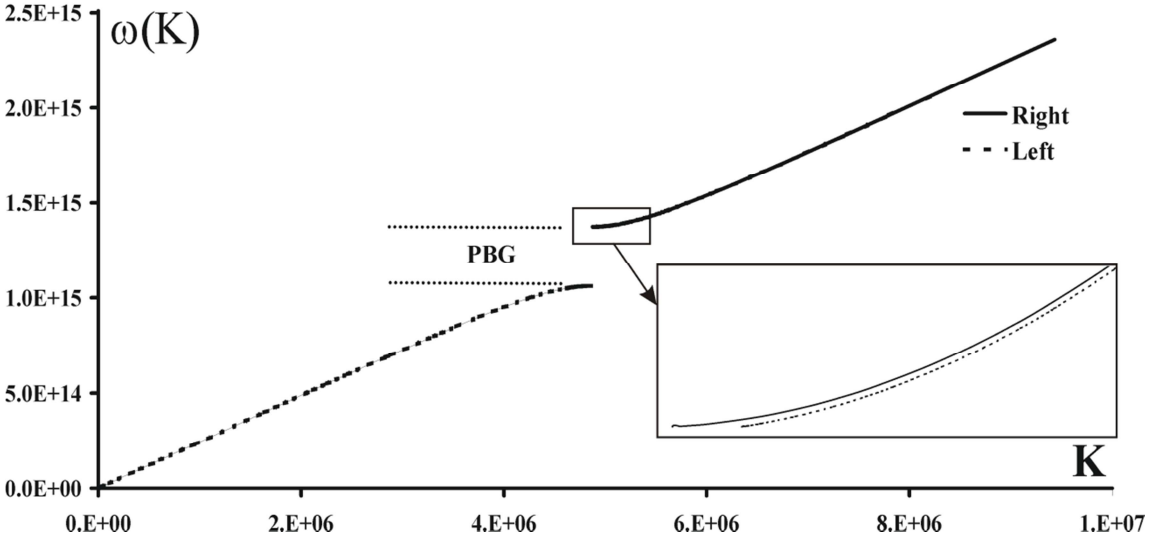

Figure II-10: Angular frequency (ω(K)) as a function of the K wavevector where the left (dashed line) and right (straight line) circular vibration were zoomed out at next the PBG for a "periodic" structure alternating magnetic and air layers; PBG position is at 1550 nm

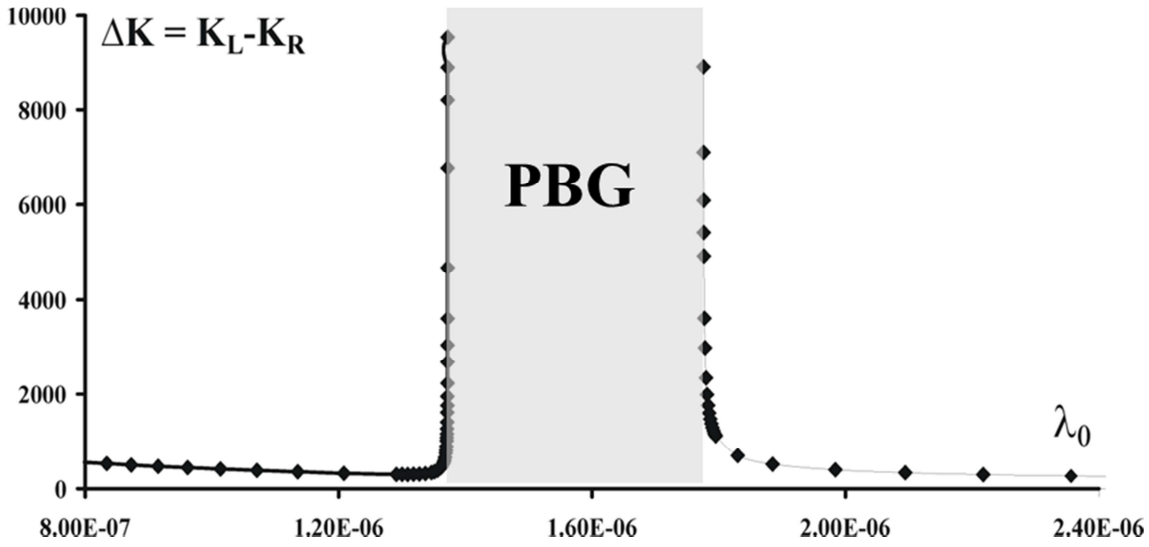

Figure II-11: Circular wavevector difference (ΔK) as a function of the wavelength (in vacuum) for "periodic" structure alternating magnetic and air layers; PBG was calculated at 1550 nm

II.3. One Dimensional Calculations

In the previous sections, we have explained how a periodicity can effect the propagation of an electromagnetic wave. Furthermore, the study of the $\omega - \vec{K}$ relation in a 1D system based on the LT2C composite allows predicting an enhancement of the FR of the edge of the PBG. But, in this study, the material was supposed to be transparent and the permittivity

tensor constant. Using complete one dimensional calculation, the aim is to go further in this study and obtain a good prediction of the behavior of the merit factor.

The 4x4 Transfer Matrix formalism is firstly summarized. Using this method transmittance, reflectance, Faraday ellipticity, Faraday rotation and merit factor can be determinated for 1D magneto-photonic crystal (MPC). For the simulation measured parameters were used, like refractive index or ε_{xy} off-diagonal element from the Faraday rotation of the Cobalt-ferrite monolayer (1% volume fraction).

Due to the special, strict periodic photonic crystal structure, changing the thickness of the layers the position of the photonic band gap (PBG) can be controlled.

The simulation was made for two different 1D MPC structures, called as “microcavity” and “periodic”. These two structures do not present the same spectral behavior, and are compared in terms of merit factor at 1550 nm.

II.3.1. 4x4 Transfer matrix calculations

For theoretical investigation “periodic” and “microcavity” arrangements of one dimensional multilayers structure was calculated by 4x4 matrix method.

Let’s consider a multilayer photonic crystal which is alternating by N number of layers (***Figure II-12***).

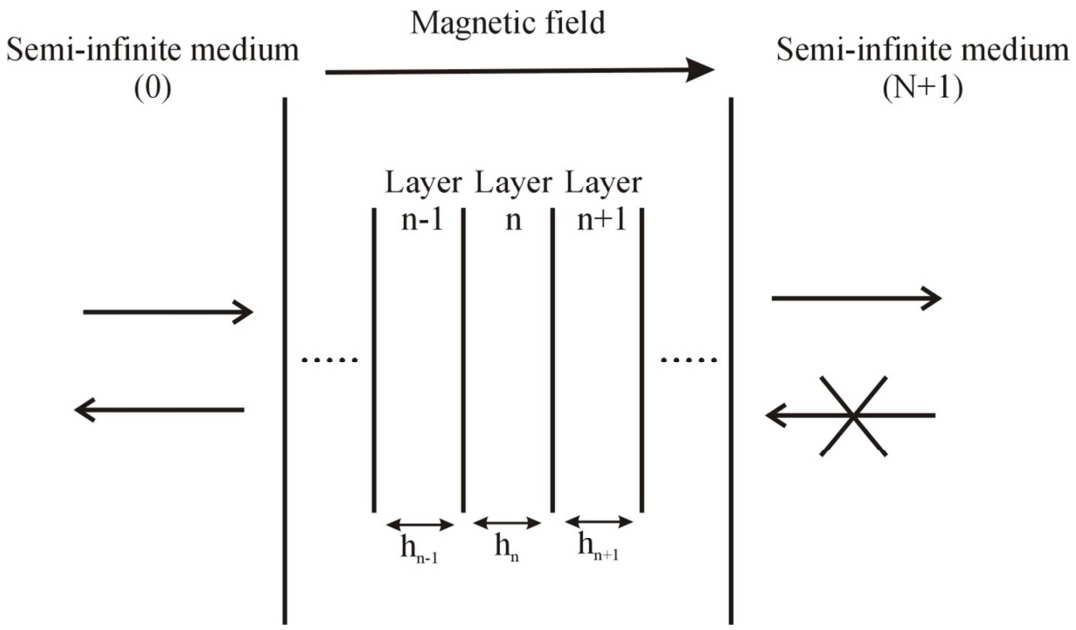

Figure II-12: Wave-transfer matrix representation of the magnetic material

Magnetization direction is perpendicular to the planar interfaces. The permittivity tensor of each layer (n) can be expressed as[53]:

$$\hat{\varepsilon}^{(n)} = \begin{bmatrix} {\varepsilon_{xx}}^{(n)} & i{\varepsilon_{xy}}^{(n)} & 0 \\ -i{\varepsilon_{xy}}^{(n)} & {\varepsilon_{xx}}^{(n)} & 0 \\ 0 & 0 & {\varepsilon_{xx}}^{(n)} \end{bmatrix} \qquad \text{Eq II.41}$$

Eigen modes which can propagate in such medium are circular. Assuming that no light come from the last semi-infinite medium, the relation between the right (+) and left (-) circular polarizations $U_{r,l}^{(i)}$ (*i* as incident), $U_{r,l}^{(r)}$ (*r* as reflected) and $U_{r,l}^{(t)}$ (*t* as transmitted) in the semi-infinite media (0 and N+1) is[55]:

$$\begin{pmatrix} U_{+}^{(i)} \\ U_{+}^{(r)} \\ U_{-}^{(i)} \\ U_{-}^{(r)} \end{pmatrix} = M \begin{pmatrix} U_{+}^{(t)} \\ 0 \\ U_{-}^{(t)} \\ 0 \end{pmatrix} \qquad \text{Eq II.42}$$

The M matrix represents the structure and is obtained by the product:

$$M = \left[D^{(0)}\right]^{-1} \cdot \prod_{n=1}^{N} D^{(n)} P^{(n)} \left[D^{(n)}\right]^{-1} \cdot D^{(N+1)} \qquad \text{Eq II.43}$$

with D: the dynamical matrix representing the continuity of the field at the interface between the layers, and P: the propagation matrix of the four Eigen modes within the layer. These matrixes can be expressed as[55]:

$$D^{(n)} = \begin{pmatrix} 1 & 1 & 0 & 0 \\ \eta_{+}^{(n)} & \eta_{+}^{(n)} & 0 & 0 \\ 0 & 0 & 1 & 1 \\ 0 & 0 & \eta_{-}^{(n)} & \eta_{-}^{(n)} \end{pmatrix} \qquad \text{Eq II.44}$$

$$\text{With } \eta_{\pm}^{(n)} = \sqrt{{\varepsilon_{xx}}^{(\boldsymbol{n})} \pm i{\varepsilon_{xy}}^{(\boldsymbol{n})}}$$

For non-magnetic layers, $\eta_{\pm}^{(n)} = \eta_{\mp}^{(n)}$

And

$$P^{(n)} = \begin{pmatrix} \exp(i\beta_{+}^{(n)}) & 0 & 0 & 0 \\ 0 & \exp(-i\beta_{+}^{(n)}) & 0 & 0 \\ 0 & 0 & \exp(i\beta_{-}^{(n)}) & 0 \\ 0 & 0 & 0 & \exp(-i\beta_{-}^{(n)}) \end{pmatrix} \quad \text{Eq II.45}$$

with: $\beta_{\pm}^{(n)} = \frac{2\pi}{\lambda}\eta_{\pm}^{(n)}h_n$.

d_n is the thickness of the n[th] layer.

The Faraday rotation is expressed as:

$$\theta_F = -i \cdot \left(\frac{M_{11} - M_{33}}{M_{11} + M_{33}}\right) \quad \text{Eq II.46}$$

The transmission amplitudes of the t^+ right and t^- left circular waves are given as:

$$t^+ = \frac{1}{M_{11}} \quad \text{Eq II.47}$$

$$t^- = \frac{1}{M_{33}} \quad \text{Eq II.48}$$

The T transmittance is:

$$T = \|t^L + t^R\| \quad \text{Eq II.49}$$

In this way the simulation for one dimensional photonic crystal is possible to compare the different type of multilayer grating with the simple magnetic monolayer [56,57].

II.3.2. Magneto-optical 1D calculation

Multilayer system is a 1D periodic structure of photonic crystal which supports strongly localized mode of light within a photonic band gap (PBG) originating from the Fabry-Perot resonance, made by dielectric material of low and high refractive index. Several authors have studied such an arrangement, especially Inoue *et al.* [2,3].

Two particular systems have been underlined by the work of Inoue. The first is a "microcavity" system, when a magneto-optical layer is sandwiched by two Bragg mirrors made by alternating high and low refractive index layer (n_H and n_L, respectively). The second is the "periodic" system made by alternating magneto-optical layer as high index material (n_M) with low index layer material.

Inoue have noted that in such systems like "microcavity" and "periodic" an enhancement of the Faraday rotation is observed in the middle of the band gap and the edge of the band gap, respectively.

For the simulation the used data are from the magneto-optical material formed by silica matrix doped with 1 % of cobalt ferrite nanoparticles. The off-diagonal element of this material has been calculated from the Faraday rotation and ellipticity of ***Figure II-13*** using the inverse relations, which derives from the Eq. II-70, 71 equations[10]:

$$\varepsilon'_{xy} = \frac{\lambda}{\pi}(n\theta_F - k\varepsilon_F) \qquad \text{Eq II.50}$$

$$\varepsilon''_{xy} = \frac{\lambda}{\pi}(n\theta_F + k\varepsilon_F) \qquad \text{Eq II.51}$$

The refractive index of the magnetic layer is given by the ***Figure II-14***.

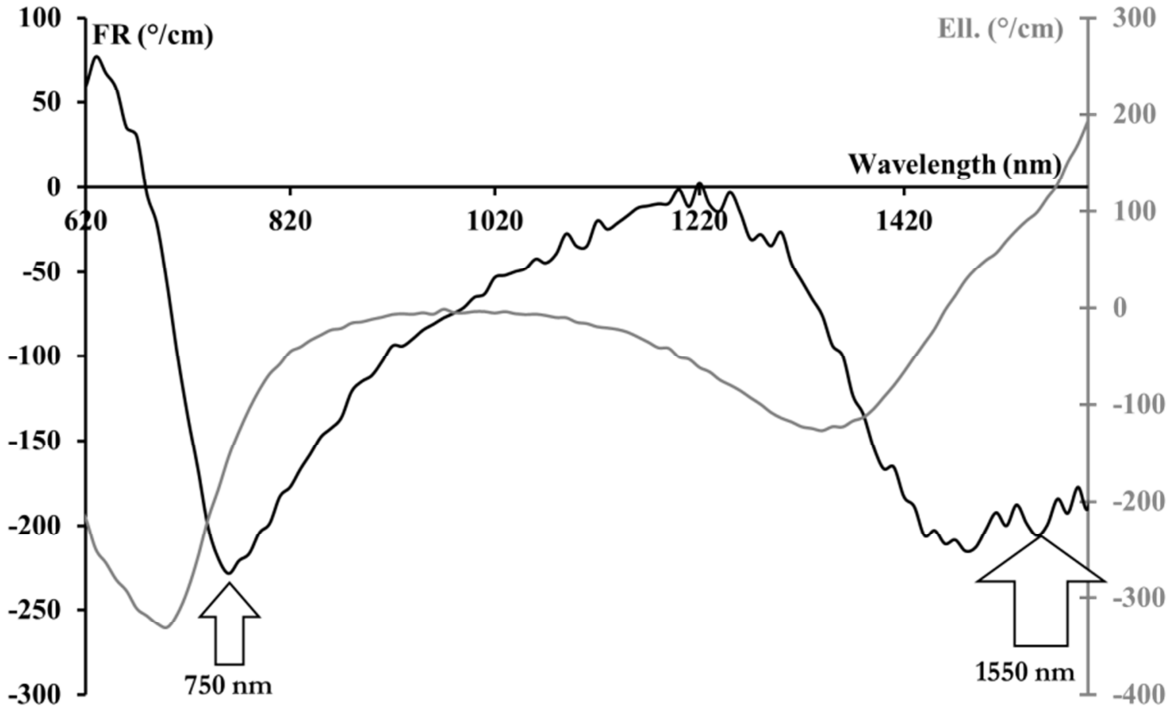

Figure II-13: Faraday rotation and Faraday Ellipticity curve of cobalt-ferrite ferrofluid (1 %)

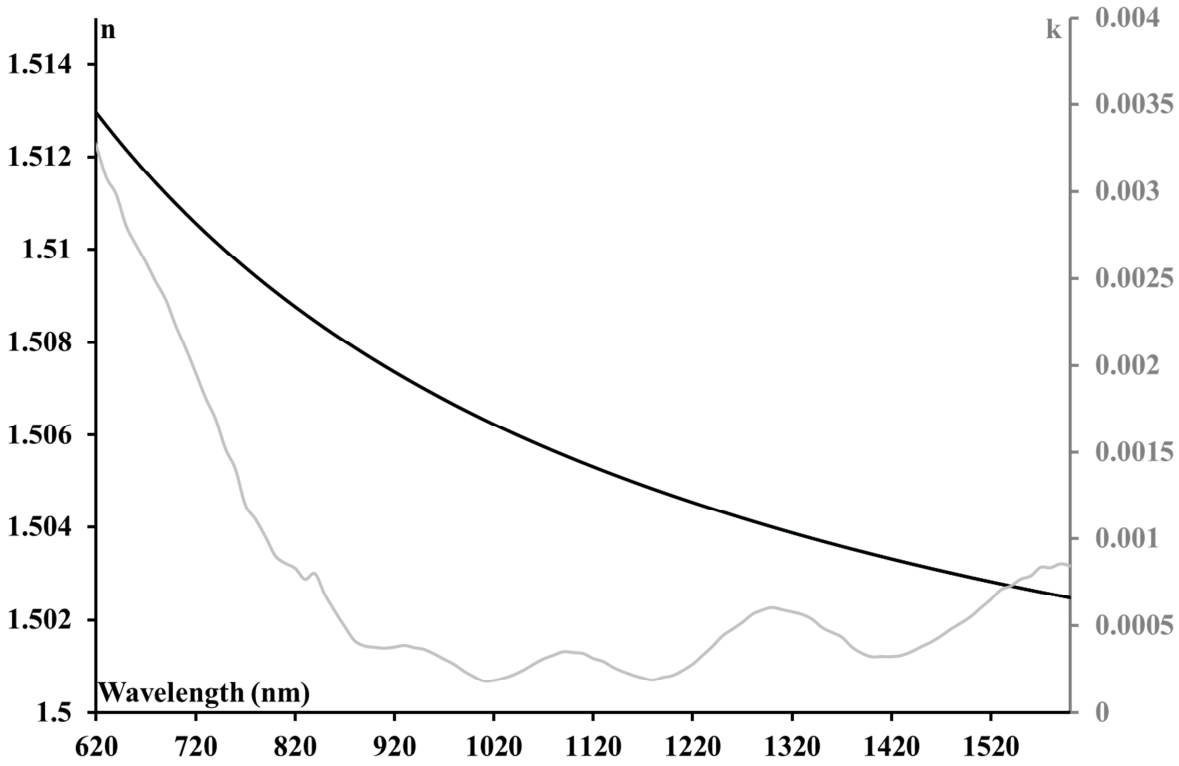

Figure II-14: Refractive index (black line) and the extinction coefficient (gray line) of the magnetic layer as a function of the wavelength (The volume fraction of the magnetic layer is 1 %.)

II.3.3. "Microcavity" structure

Figure II-15 shows the "microcavity" structure arrangement, where in the center a magnetic layer has been placed as a defect layer. The simulation was made for 21 layers, alternating high (n_H) and low (n_L) refractive index layers in the Bragg mirrors. The thickness of the layers is determinated by the desired position of the band gap center λ_C:

$$h_{H/L} = \frac{\lambda_C}{4n_{H/L}} \qquad \text{Eq II.52}$$

$$h_M = \frac{\lambda_c}{2n_M} \qquad \text{Eq II.53}$$

The used refractive index values for the thickness calculation were $n_M = 1.504$, $n_L = 1$ and $n_H = 1.5$.

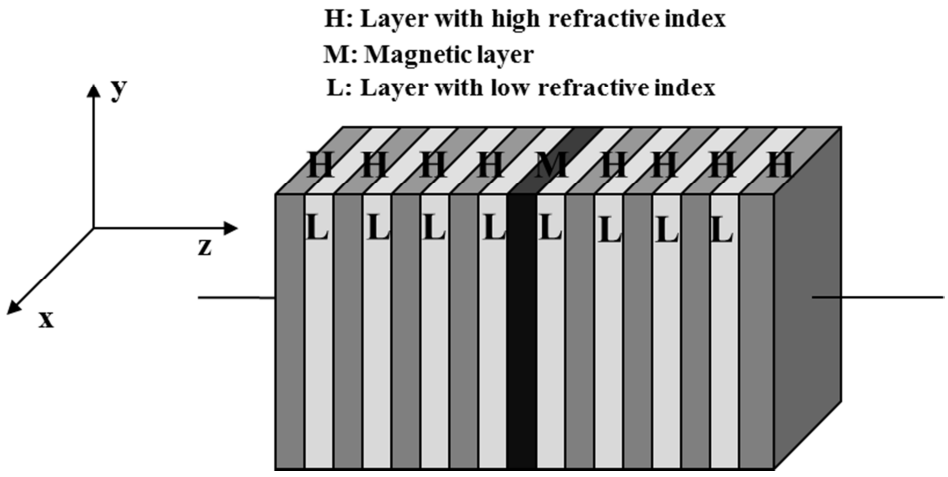

Figure II-15: 1D magneto photonic crystal "microcavity" structure; A magnetic defect is introduced in a Bragg mirror.

II.3.4. "Periodic" structure

The "periodic" system with 25 layers was created alternating by magnetic and non-magnetic layers (***Figure II-16***).

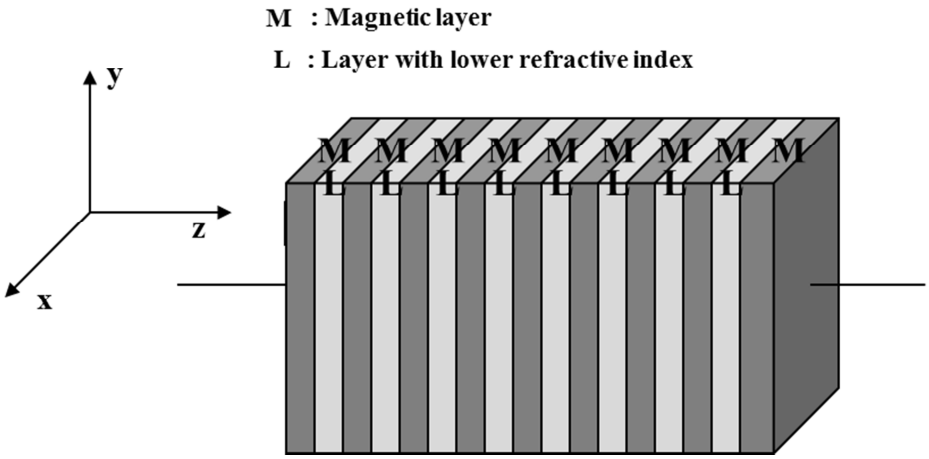

Figure II-16: 1D magneto photonic crystal "periodic" structure alternating by magnetic and air layers

In this special case, we have to remind that the magneto-optical increase is at the edge of the photonic band gap. Thus to compare "periodic" and "microcavity" we have adjust the position of the PBG peak.

$$h_{M/L} = \frac{\lambda_C}{4n_{M/L}} \qquad \text{Eq II.54}$$

The used refractive index values for the thickness calculation were: $n_M = 1{,}504$, $n_L = 1$.

II.3.5. Comparison between the "periodic", "microcavity" and monolayer structure

Using 4x4 matrix formalism, transmittance, Faraday rotation and merit factor graphs have been determined. As expected in ***Figure II-17*** and ***Figure II-18***, the area where the Faraday rotation is increased is located in the center and at the edge of the band gap for "cavity" and

"periodic" structure, respectively. This result is in a good agreement with previous works of Inoue [2].

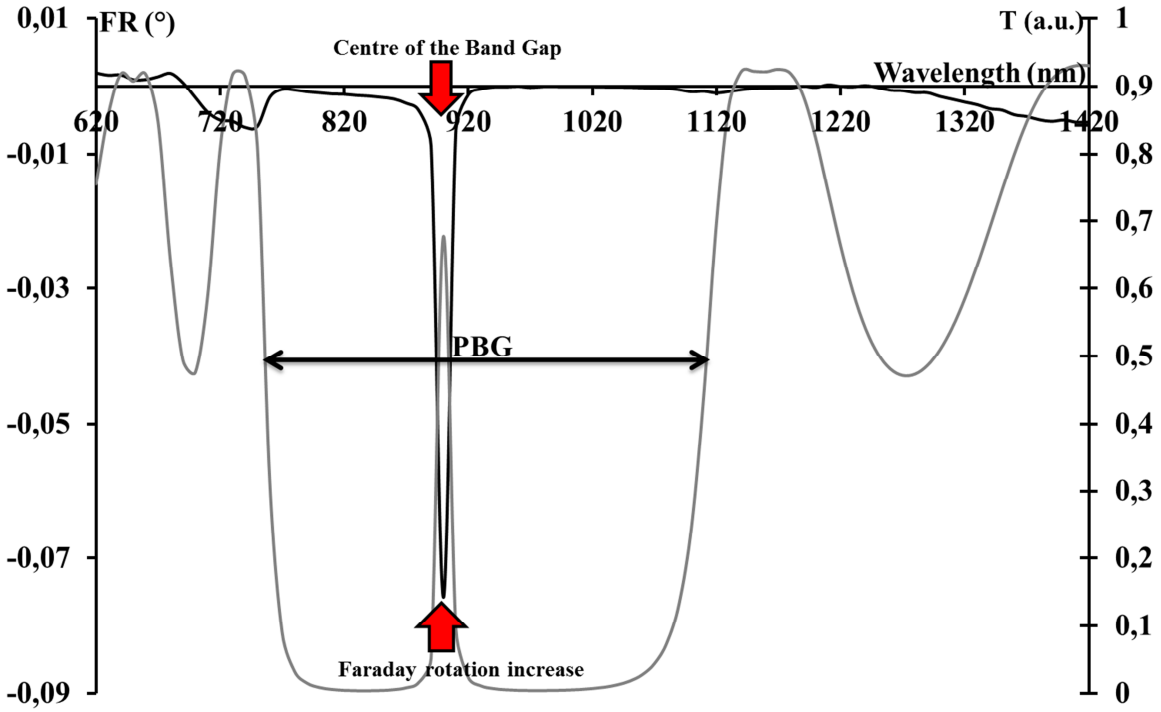

Figure II-17: Calculated transmittance (gray line) Faraday rotation (black line) of "microcavity" for positioning the PBG at 900 nm

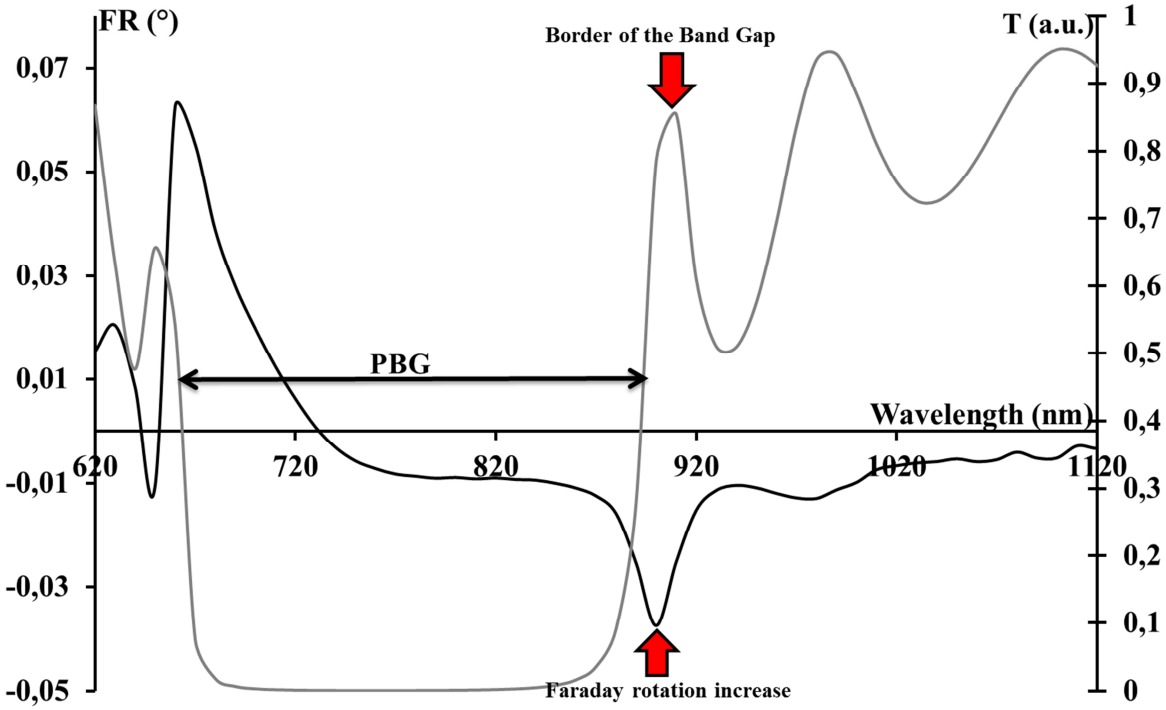

Figure II-18: Calculated transmittance (gray line) Faraday rotation (black line) of "periodic" for positioning the border of the PBG at 900 nm

These results do not show a huge effect in terms of Faraday rotation. This is only because the chosen central wavelength was placed in order to have a full view of the photonic band gap and, the Faraday rotation at 900 nm is quite low. Let's now consider an area where the Faraday rotation is more interesting, such as 1550 nm.

Figure II-19 and ***Figure II-20*** show the Faraday rotation of the "microcavity" and the "periodic" structure compared to an equivalent magnetic monolayer. In the first case, the thickness of the monolayer is the same as the magnetic defect layer. In the second one, the thickness is the sum of all magnetic layer thicknesses.

The two multilayer crystals have high value of Faraday rotation. The Faraday rotation of "microcavity" (***Figure II-19*** black line) and "periodic" (***Figure II-20*** black line) structure are about -0.31 ° and -0.17 °, respectively. However the magnetic monolayer (***Figure II-19***, ***Figure II-20*** gray line) has -0.01 ° and -0.05 ° Faraday rotation values at 1550 nm, respectively.

We can see clearly that in the two cases, the Faraday rotation is enhanced at the chosen wavelength compared to the magnetic monolayer. To finalize this analysis, we have to compare also the merit factor. This is done in the ***Figure II-21***

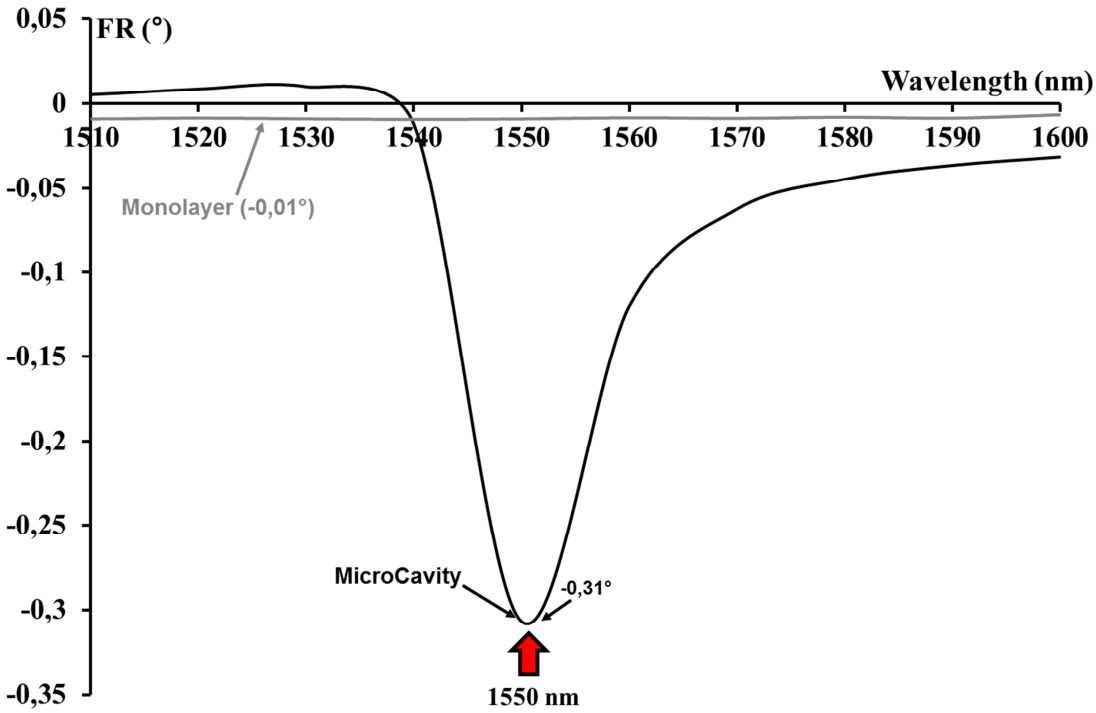

Figure II-19: Calculated Faraday rotation of "microcavity" (black line) and monolayer (gray line) structure for positioning the PBG at 1550 nm (Cobalt-ferrite thickness=516 nm)

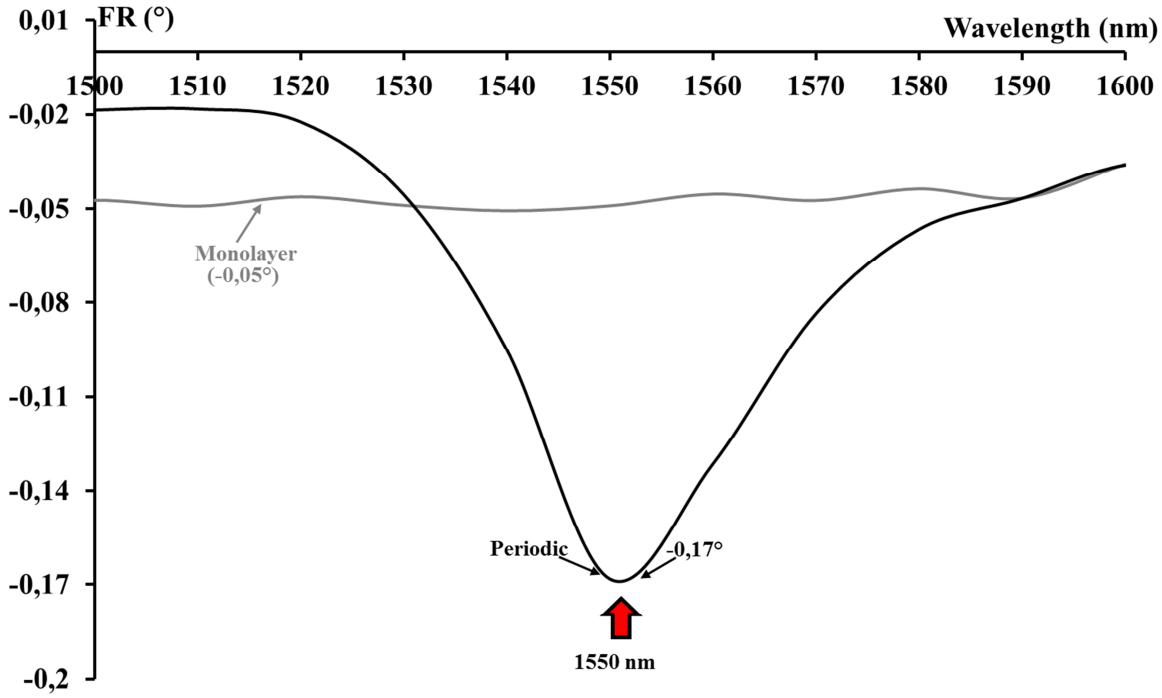

Figure II-20: Calculated Faraday rotation of "periodic" (black line) and monolayer (gray line) structure for positioning the PBG at 1550 nm (Cobalt-ferrite thickness= 2808 nm)

Centering the photonic band gap at the maximum of the Faraday rotation is not enough to obtain a better merit factor compared to a simple monolayer. Indeed, with a Faraday rotation ranging from three times ("periodic" structure), up to thirty times ("microcavity" structure) higher than the monolayer, the merit factor does not show the same enhancement. Thus, optimization of the structures has to be carried out. Numerous simulations have been done, by changing the number of layer and the central peak of the BPG. Without optimization tools, we found that the better merit factor value for the two structures was reached at 1450 nm. In this case, an important increase is observed for the periodic structure. This 1D calculation and the results of Inoue[2,5], Koerdt[47] and Caiedo[48] *et al*. assure the MO effect increase for 3D magneto-photonic crystal.

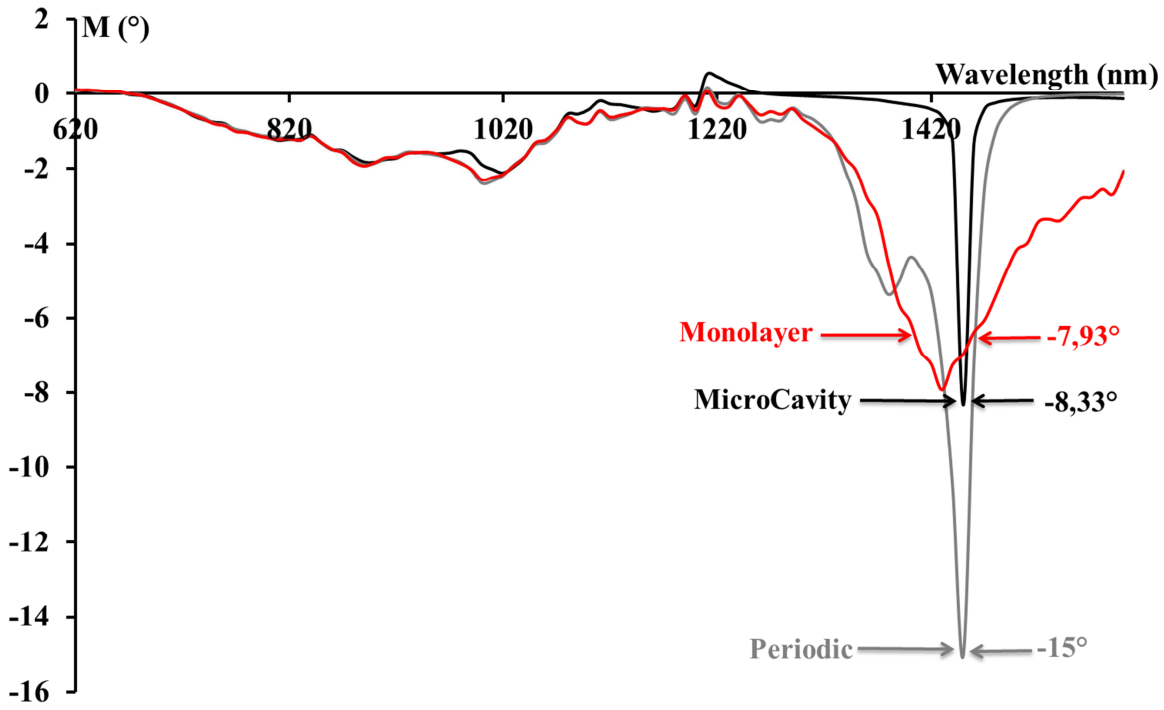

Figure II-21: Calculated merit factor of "periodic" (gray line), "microcavity" (black line) and monolayer (red line) structure for positioning the PBG at 1450 nm

II.4. Conclusion

In the first part of this chapter, we tried to give some clues for a better understanding of the propagation of light in periodic systems. Using Bloch mode theory we have shown the existence of energy bands where the propagation is forbidden. A fine analysis of the $\omega - \vec{K}$ dispersion relation is achieved in a 1D periodic structure. If one of the materials is magnetic the left and right circular polarizations split up and this generates ΔK wavevector difference. This difference is enhanced at the edges of the PBG, inducing an increase of the Faraday rotation.

To go further and study the behavior the merit factor in this area, 4x4 transfer matrix calculations have been led using our magnetic composite material. These calculations take into account the absorption and the spectral behavior of the permittivity tensor.

In the case of "microcavity" structure the simulation shows that the Faraday rotation increases in the center of the band gap, whereas, it occurs at the edge of the photonic band gap, in the case of "periodic" structure.

The most important result is that we can also increase the merit factor under certain conditions.

III.CHAPITRE: Élaboration et caractérization de cristaux magneto-photonique 3D (resumé francais)

Les cristaux magnéto-photoniques 3D peuvent être à base d'opales artificiels. Ces opales ont la possibilité de contrôler la lumière, comme les opales naturels, grâce à un arrangement strictement périodiques de billes et à une différence élevée d'indice de réfraction entre ces billes et une matrice. Dans la gamme d'application visée, (visible, infra-rouge), la modulation spatiale des billes de quelques nanomètres à quelques centaines de micromètres est nécessaire.

L'élaboration de films à base de billes est réalisée par différentes techniques, la structure obtenue est nommée « opale direct ». La méthode, la plus simple d'arrangement, est la sédimentation [60-61]. Les billes sont placées dans une solution à base de solvant. La gravité permet aux billes de s'organiser lors de l'évaporation du solvant. Par cette technique, le contrôle de l'épaisseur est difficile et l'élaboration à grande échelle est impossible.

Pour diminuer les inconvénients de la sédimentation, différentes méthodes ont été développées. La première est le dépôt vertical. Dans ce processus, le substrat est positionné verticalement dans une solution comprenant un solvant et les billes à déposer. Les propriétés hydrophiles du substrat permettent aux billes d'adhérer au substrat. Après l'évaporation de l'eau ou autre solvant, l'opale direct présente une structure cfc sur la surface du substrat. Afin d'optimiser cette technique, Lopez *et al.* a placé le substrat avec un angle de 20 ° [54].

La seconde est une technique de centrifugation. Dans cette méthode, la suspension contenant le solvant et les billes est placée dans un récipient d'une centrifugeuse. La force centrifuge permet aux sphères de s'installer au fond du récipient où est situé le substrat. Des opales directs avec une structure cfc ont été obtenus par Nishijima *et al.*[6].

La troisième, dite technique de Langmuir-Blodgett, consiste en un trempage d'un substrat qui est tiré régulièrement [62], à vitesse constante, hors de la solution contenant le

solvant et les billes. Le mouvement du substrat entraîne le liquide par tension superficielle.

Le quatrième technique est la déposition vertical ou le substrat est positionner verticalement dans un bécher qui contient de solution de billes self-assemblée. Le solvant commence à s'évaporer au niveau du ménisque. Les billes adhèrent à la surface du substrat hydrophile, en raison de la force d'adhérence. Les billes s'accrochent les unes aux autres par une force de répulsion. En général, plusieurs couches de sphères se déposent sur le substrat. L'arrangement est ordonné selon des modèles observés en cristallographie. L'auto-assemblage des billes implique une structure cfc en raison de la force de répulsion entre les sphères, les billes se placent alors dans la position de la plus basse énergie. L'arrangement est réalisé pour donner une structure sous la forme d'un tétraèdre.

Inspiré des travaux de Nishijima, des billes de polystyrène ont été retenues pour réaliser l'arrangement de l'opale direct. L'indice de réfraction de ces billes est de 1,59 à 589 nm. Quatre diamètres de billes ont été testés : 400 nm, 453 nm, 799 nm et 903 nm [6].

Lorsque la structure opale direct est réalisée, il est nécessaire d'obtenir un opale inverse qui peut être défini comme une arrangement de sphères d'air jointes les unes aux autres avec de petits canaux dans une structure 3D régulièrement ordonnée. A partir de l'opale direct obtenu, l'espace vide interstitiel est remplit avec un liquide. Dans la littérature, les sphères sont en général en PMMA [66] ou en polystyrène [6, 67-70]. Le liquide remplissant les interstices sont divers, nous pouvons citer en exemple le SiO_2, TiO_2 ou CeO_2 [66]. Ces liquides sont obtenus sur la base des expériences acquises dans la technique sol-gel. Les billes sont ensuite éliminées par calcination (températures entre 400 à 500 °C [73-78]) ou gravure chimique avec des solvants aromatiques et chlorés, comme le benzène, le chloroforme, le tétrachlorure de carbone, le cyclohexane, le diméthylformamide, le chlorure de méthylène, la pyridine, le tétrahydrofurane, le toluène, le xylène et l'acétate d'éthyle [6, 71-72]. Ces différents travaux montrent que le procédé sol-gel peut être utilisé dans l'élaboration des opales inverses 3D.

La technique sol-gel est un processus où un liquide colloïdal devient une chaîne polymère solide par un enchainement de réactions : l'hydrolyse et la polycondensation. Cette méthode a l'avantage d'être peu coûteuse et de pouvoir être réalisée à basse température. Le matériau précurseur utilisé est le TEOS. Cet alcoxyde métallique est un bon précurseur en raison de la compatibilité aisée avec l'eau. Lors de l'élaboration de la phase liquide, le matrice peut-être dopée avec des nanoparticules magnétiques comme la maghémite [7] ou encore les ferrites de cobalt [8, 10, 21, 28, 84]. Les nanoparticules de ferrite de cobalt sont de faibles tailles (10

nm), isotropes sans champs magnétique. Ces particules peuvent acquérir une anisotropie optique sous l'influence d'un champ magnétique. Cette anisotropie est circulaire en configuration Faraday longitudinale (direction du champ magnétique parallèle à faisceau lumineux) et linéaire dans la configuration de Voigt (magnétique perpendiculaire au champ de faisceau lumineux) [8].

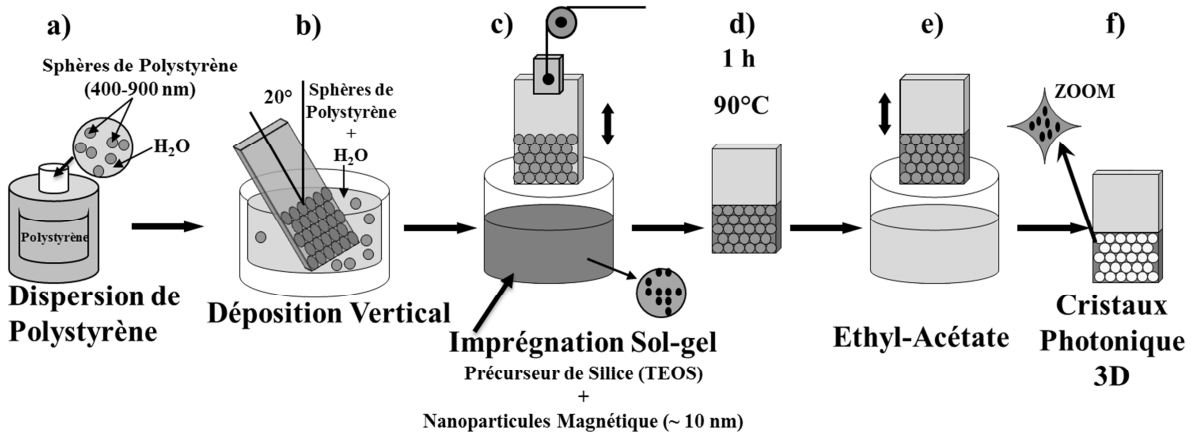

Figure 1. : Process d'élaboration de cristaux photonique

Le processus d'élaboration des échantillons étudiés se décompose suivant cinq étapes (*Figure 1*) :

- préparation du substrat (nettoyage rigoureux de verre en borosilicate),
- dépôt verticale avec un angle à 20 ° pour l'obtention de l'opale direct,
- imprégnation avec une préparation TEOS de l'opale direct. Le TEOS est dopée ou non avec des nanoparticules de ferrite de cobalt,
- processus de séchage (90 °C, 1 heure),
- élimination des billes de polystyrène de la matrice par de l'acétate d'éthyle pour obtenir l'opale inversé.

Les films d'opale direct ou d'opale inverse sont caractérisés par différentes techniques d'analyses afin de les étudier. Le microscope électronique à balayage a été utilisé afin d'observer l'état de surface de ces opales. Cet appareil permet d'obtenir des images précises des films jusqu'à une résolution de 1 nm sous pression contrôlée. Cette technique est basée sur la focalisation d'un faisceau d'électrons de haute énergie sur la surface de l'échantillon. L'énergie dissipée des électrons se trouve sous forme de différents signaux liés aux interactions électrons-échantillon. Les électrons secondaires et rétrodiffusés sont utilisés pour

réaliser l'image de la surface de l'échantillon. Les électrons secondaires permettent de donner des informations sur la morphologie et la topographie des échantillons. Le contraste de l'image donnée par les électrons rétrodiffusés, informe de la composition des échantillons multiphasiques [87-88].

La valeur diélectrique des films est un paramètre important dans le domaine de cristaux photoniques. La seconde technique utilisée est l'ellispométrie qui est basée sur l'étude de la modification de l'état polarisation de la lumière par réflexion de la lumière sur la surface plane d'un échantillon. Par la mesure de différents paramètres en fonction de la longueur d'onde, on peut déterminer la dispersion de l'indice de réfraction et l'épaisseur de la couche. Ceci est réalisé en ajustant les paramètres du modèle théorétique aux données expérimentales à travers un processus d'optimalisation (algorithme de Levenberg-Marquardt [37-38]).

La détermination des propriétés optiques du matériau sol-gel dépose sur couche mince opales directs ou inverses a été réalisée à l'aide d'un ellipsomètre spectroscopique à modulation de phase. Un banc optique (polarimètre spectral) permettant de caractériser les propriétés optique et magnéto-optique a été développé au laboratoire (*Figure 2*). Il se compose d'une source halogène au tungstène (qui peut permettre de couvrir le gamme de longueur d'onde 400-1700 nm) d'un polariseur, d'un porte-échantillon avec des translations en X et Y possibles et d'un microscope. Ce dernière comporte un analyseur pour la mesure de la polarisation et un séparateur de faisceau pour effectuer l'analyse spectrale par un spectromètre CCD. La source de lumière couvre la gamme 360-2000 nm. Deux spectromètres permettent de réaliser cette gamme de mesures. Pour les mesures sous champs, un aimant Néodyme Fer Bore est utilisé et permet d'obtenir un champ magnétique longitudinal pouvant atteindre 350 mT.

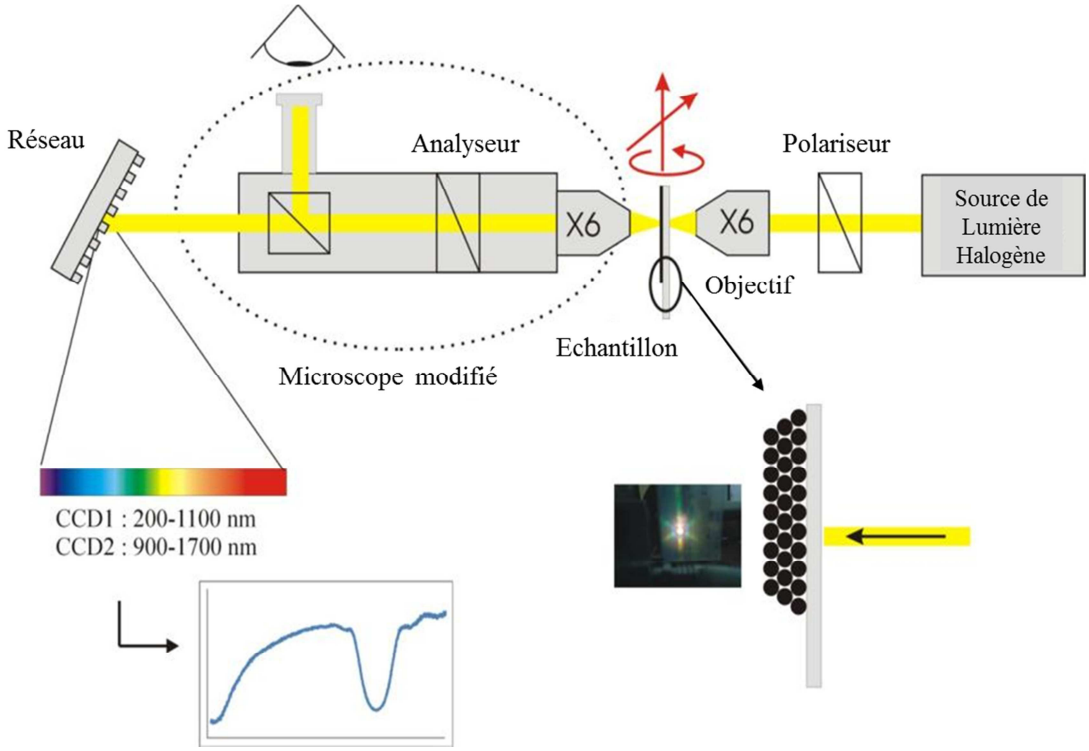

Figure 2. : Spectral Photo-polarimètre

La mesure de la transmittance est réalisée dans toute la gamme spectrale en utilisant la configuration décrite ci-dessus. Ces mesures permettent de déterminer la position des bandes interdites photoniques. En utilisant la loi de Bragg on peut estimer l'espacement interplanaire et l'indice effectif de la structure.

Ce dispositif de caractérisation permet aussi de déterminer la mesure de la rotation Faraday. En effet, le comportement spectral en terme de rotation Faraday des nanoparticules magnétiques devrait être modifié par la présence de la bande interdite photonique. Pour la mesure de la rotation Faraday, le formalisme de Jones (calcul matriciel) a été utilisé. Dans cette méthode, les éléments polarimètrique spectral sont désignés comme une matrice. La multiplication matricielle de chaque élément résulte de la détermination de l'intensité de la lumière transmise. Le facteur de mérite peut également être calculé à partir de cette mesure en par prise en compte de la rotation Faraday et du coefficient d'absorption.

III.CHAPTER: Elaboration and characterization of 3D Magneto-Photonic Crystals

This chapter deals with the thematic of the elaboration and the characterization of 3D photonic and magneto photonic crystals. We firstly give some information about the opal based photonic crystals. This “bottom up” approach allows the realization of direct opal, which is a stacking of polystyrene or silica submicron spheres. This direct opal serves as a template which can be filled with a sol gel solution in order to realize, after the removal of the spheres, an inverse opal.

A review of the self-assembly method is proposed and the properties of the used polystyrene spheres is given. We describe the protocol employed for the synthesis of the sol-gel solution, which can be doped with magnetic nanoparticles issued from a ferrofluid. Then the complete synoptic procedure of the elaboration of magneto photonic crystals is presented.

This chapter ends with the presentation of the characterization equipments: scanning electron microscope, ellipsometry and spectral photo-polarimeter.

III.1. Opal based 3D Photonic Crystals

In this part natural and artificial opal will be represented. Moreover, the realization methods of the three dimensional artificial opals will be explained. This part will reveal the advantage and disadvantage of each opal elaboration. Finally, it will define the face-centered cubic structure, which can be realized by self-assembly materials.

.

III.1.1. Natural opal

Natural opals grow inside earth at relatively low temperature and pressure. The chemical composition is hydrous silicate di-oxide (SiO_2+n H_2O). The word of “opal” probably came from a Sanskrit word of “upala” or a Latin word of “opalus” which means precious stone.

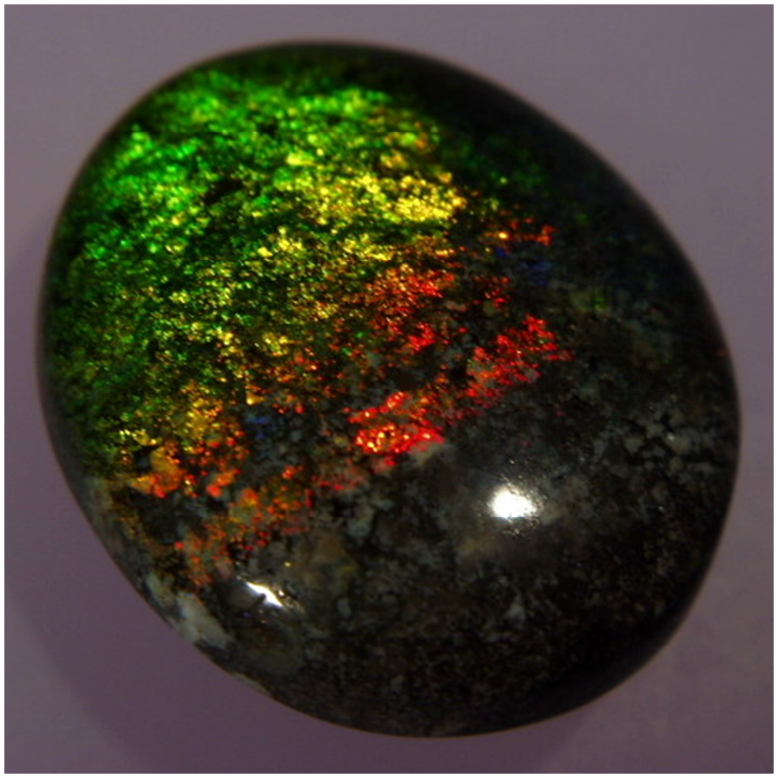

Figure III-1: Natural opal

This hydrated amorphous silica produces iridescent of colors within the opal, presented on ***Figure III-1***. The explanation of this “play of color” or “opalescence” is the wave light scattering from the ordered arrays of the microscopic spheres of silica with size comparable with the wavelength of the light wave. The “opalescence” depending of the arrangement of

the packing and the size of the spheres as the light passes through the strictly ordered opal-network.

Artificial opals are promising possibility of controlling the light, like the natural opals, due to the strictly periodic arrangement and sufficiently high refractive index difference for new photonics technologies.

III.1.2. Artificial opal

Artificial opal was created by copying the nature. Such a strict periodic structure in the nanometer scale can be realized in the laboratory by different chemical process. The created opals also possesses the “opalescence” effect, as a prove of the succeeded fcc structure.

III.1.2.1. Direct opal

Fabrication of photonic crystal implies the structuration of matter in the scale of hundreds of nanometer. To carry out this structuration two ways can be used: the “top down” and the “bottom up” approach. The “top-down” approach is often used in traditional micro fabrication methods where externally-controlled tools are used to cut, mill, and shape materials into the desired shape .Micro patterning techniques, such as photolithography and inkjet printing belong to this category. “Bottom-up” approaches, in contrast, used the chemical properties of single molecules to cause single-molecule components to self-organize or self-assemble into some useful conformation.

Self-assembly method is cheap and well-developed process for the fabrication of artificial opal (***Figure III-2***). The first suggestion of this method was made by Eli Yablonovitch at 1987 [49]. One of the early realization was made at 1995 [58] by Tarhan *et al*.

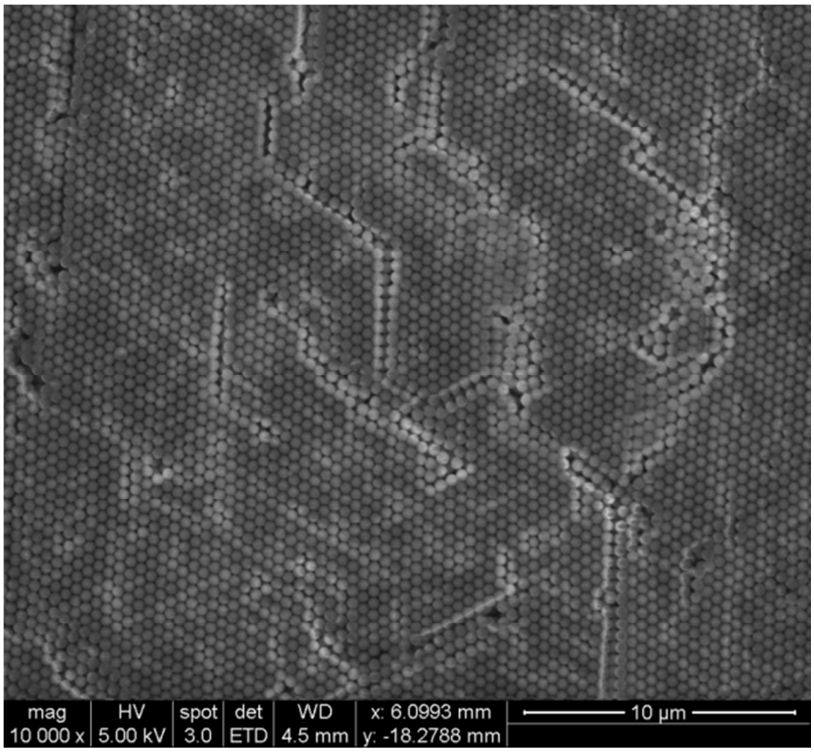

Figure III-2: Direct artificial opal

III.1.2.2. Self-assembly methods

There are four different interesting procedures as self-assembly technique, depending of the final application. Lopez *et al.* [59] insist that all of these techniques the vertical deposition provides the highest optical quality.

III.1.2.2.1. Sedimentation method

The most simple method of the self-assembly is the sedimentation, when due to the gravity the colloid particles settle down during the evaporation of the solvent. The sedimentation cannot give the control of the thickness and produce a large scale of variation of defects.

One drop of aqueous colloid suspension with the wanted concentration was dripped down on a surface of the substrate. As the time passing by, the water evaporates and results self-assembly structure (***Figure III-3***). This organization is not free off cracks and disorders [60,61].

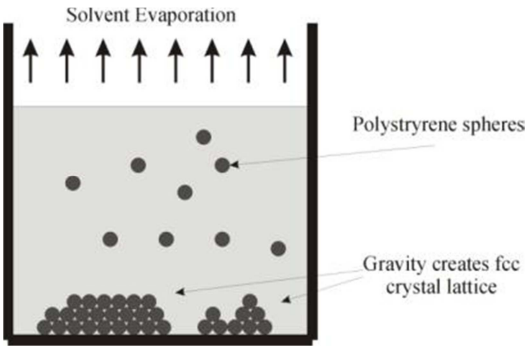

Figure III-3 Sedimentation method

III.1.2.2.2. Vertical deposition method

Vertical deposition was developed to take over the control of the drawbacks of the sedimentation.

During the vertical deposition the direct opal grows until the liquid evaporate and its meniscus is moving forward. The starting point is when the liquid meniscus is under the diameter of the sphere. The hydrofil substrate attaches the particle to surface of the substrate, and due to the repulsive force between the spheres they are organized to each other creating face-centered-cubic structure. After the evaporation of the water from the polystyrene dispersion the structure organization is stabilized by the cohesive force. Generally, more than one layer of spheres grows on the substrate.

The good crystallization rates depends of the density, the size of the spheres, the solvent liquid, the temperature of the evaporation, the shape and cleaning process of the substrate.

Lopez *et al*. found that the highest optical quality yields between the concentration ratio 0.05-0.4 % vol. During the deposition, temperature must be controlled in order to have a steady evaporation rate.. The best optical properties was found with the drying temperature of 45 °C for the spheres with the diameter size lower than 705 nm and 50 °C for higher diameters.

In this process the substrate has positioned vertically in the colloid solution holder beaker. After the evaporation of the water or other colloid carrier liquid, it leaves fcc direct opal on the surface of the substrate.

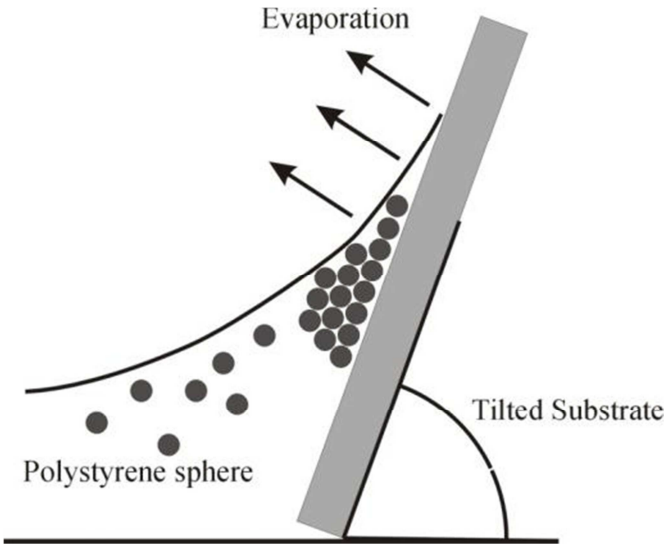

Figure III-4: Vertical deposition

In order to create a well-organized fcc structure this method can be even more effective, if the substrate position angle is not 90 ° (horizontal). Lopez *et al*. [54] founded the best tilt angle for the elaboration of fcc structure at 20 ° with the respect of the vertical (***Figure III-4***). They also established the optimal fix temperature correspondingly to the diameter size of the spheres of the constructed direct opal.

III.1.2.2.3. Centrifugation method

In this method the colloid suspension is dropped in a tube of the centrifuge. Due to the centrifugation force, the colloid spheres should settle down to the bottom (***Figure III-5***). Nishijima *et al*. [7] created direct opals on a use of this process. They interpreted that the direct opals have nice fcc structure. In spite of the well-organized closed packed structure, this method has technical difficulties as deposing the direct opal into the substrate.

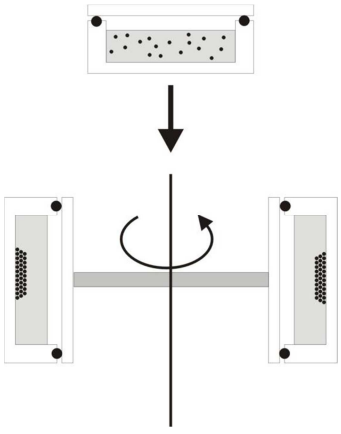

Figure III-5: Centrifugation method

III.1.2.2.4. Langmuir-Blodgett method

This elaboration technique is a motor driven substrate deposition from the aqueous surface of polystyrene particles or amphiphile molecules[62]. The principal of monolayers building is that due to the compression of the polystyrene spheres on the surface of the given subphase, usually water, the polystyrene spheres are extruding to the substrate surface and spreading 2D photonic crystal. The advantage is that the realization of the layer can be completely controllable, but the disadvantage is that it can produce only one layer. Thus, this elaboration is only used for the realization of 2D photonic crystals. (***Figure III-6***).

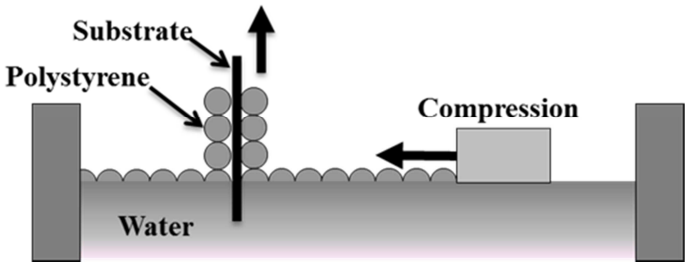

Figure III-6: Langmuir-Blodgett method

III.1.2.3. Fcc arrangement

The advantage of the self-assembly spheres like PMMA (Polymethyl-methacrylate) , SiO_2 or polystyrene that due to the repulsive force between the spheres, they find the lowest energy position, and result fcc structure (***Figure III-7***).

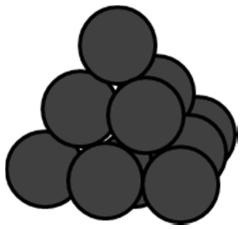

Figure III-7: Perfect fcc organization

In such a structure, some parameters are useful for this study. The first one is the filling fraction also known as Atomic Packing Factor (APF). The value of APF had been well-proven since 1611. Johannes Kepler was the first scientist who stated that the greatest average of density of the arrangement of equally sized spheres is the cubic close packing structure

with the value of ≃0.74. This problem after Kepler had well-studied and predicted a possible solution using by a fast computer by Laszlo Fejes Toth in 1953, and completely had proven and accepted as a theorem by Thomas C. Hales in 2003 [63,64].

The Kepler Conjecture: *"No packing of congruent balls in Euklidean three space has density greater than that of the face-centered cubic packing. This density is* $\pi \cdot \left(\sqrt{18}\right)^{-1} \approx 0.74$*."*

This filling fraction allows us to determine the effective refractive index. n_{Eff} of the structure. It is given by:

$$n_{Eff} = \sqrt{f_{sph} \cdot n_{sph}^2 + \left(1 - f_{sph}\right) \cdot n_v^2} \qquad \text{Eq III.1}$$

where f_{sph} is the sphere filling fraction, n_{sph} is the refractive index of the spheres and n_v is the refractive index of the voids between the spheres [7].

For such a fcc structure we also have to know the interplanar distance d_i (***Figure III-8***), which define the periodicity of the crystal. In this case, it is given by [65]

$$d_i = \sqrt{\frac{2}{3}} d_{sph} \approx 0.816 \cdot d_{sph} \qquad \text{Eq III.2}$$

Where d_{sph} is the diameter of the spheres.

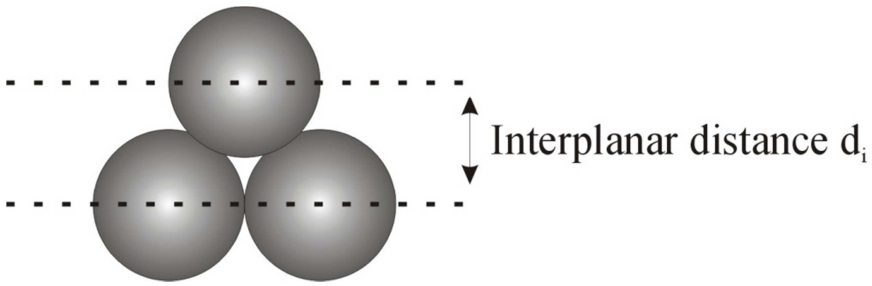

Figure III-8: Schematic image for the interplanar spacing

This strict periodic arrangement causes photonic band gap due to the constructive reflections. The position of the PBG can be calculated due to the Bragg law **(*Figure III-9*)**:

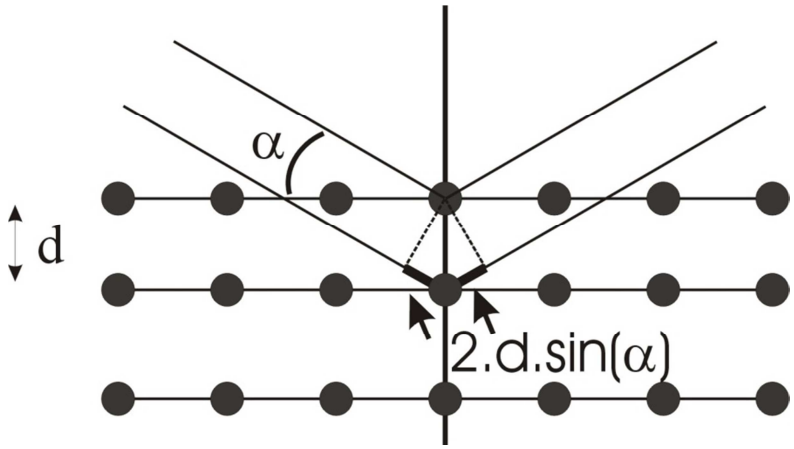

Figure III-9: Bragg diffraction

$$\lambda_c = 2 \cdot \sqrt{\frac{2}{3}} d_{sph} \cdot n_{Eff} \cdot \sin(\alpha) \qquad \text{Eq III.3}$$

where λ_c is the center of the PBG, and α the angle of the beam in the medium.

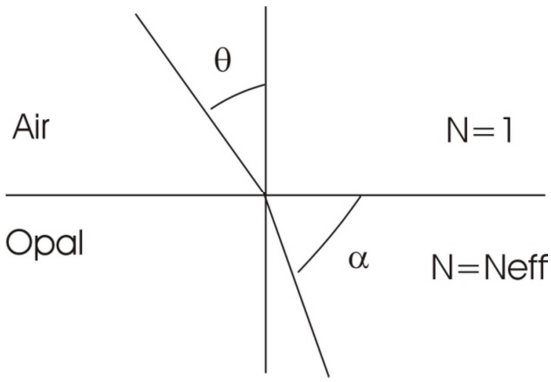

Figure III-10: Interface air/opal

For light coming from air with an angle of incidence θ (***Figure III-10***), the Bragg law can be written as:

$$\lambda_C = 2 \cdot d_i \sqrt{n_{Eff}^2 - \sin^2 \theta} \qquad \text{Eq III.4}$$

III.1.2.4. Inverse opals

Realization of inverse opal is a key element of this thesis.

It can be defined as a collection of air spheres join to each other with small channels in a strict periodically ordered 3D structure, showed on ***Figure III-11***.

Basically, this fabrication starts with creating the colloidal sphere direct opal as a template, then fill the interstitial void space with the wanted material, and finally remove the mask .The last step can be elaborated by calcination, etching or with acid utilization.

Waterhouse *et al.* [66] presented an inverse opal fabrication made by centrifugation on a use of PMMA spheres in aqueous suspension with 280-415 nm diameter size. They infiltrated the void space with SiO_2 or TiO_2 or CeO_2 by sol-gel technique. The template was eliminated with 550 °C calcination. The inverse opals possess the well-ordered fcc array structure.

Cao [67], Abramova [68] and Jin [69,70] *et al*. reported their work using polystyrene template growing with vertical deposition and sol-gel process of the creation of inverse opals. This mask was made by vertical deposition method at 55 °C. Before the infiltration of titania sol (titanium tetra-isopropoxide, anhydrous ethanol, diethanol amine, deionized water with the mass ratio of 1:6.47:0.22:0.1) the polystyrene opal was heated to 80 °C during 30 minutes to ignore the collapse of the 3D lattice. They used vertical impregnation during 1 minute. After the gelation of the sol-gel titania sol, the impregnation process was repeated two times. Then by calcination the polystyrene balls were eliminated from the sample in 500 °C.

Abramova used 450 nm diameters of spheres and created the direct opal at 50 °C. It was impregnated with saturated water-alcohol (1:1) solution of zinc nitrate, and then it was annealed at 300 °C until 12 hours. Jin used 330 nm of diameter of polystyrene balls for the template with the drying temperature at 45 °C. The latex opal was dipped into the Cerium doped barium titanate or cerium doped titania precursor solution. After it was vacuumed until 15 minutes and dried at room temperature. The impregnation was repeated for 3 or 4 times then the sample was annealed at 750 °C. All of the cases resulted high quality of inverse opal three dimensional arrangements. These studies examined the structure and the chemical composition of the structure, but optical measurement was not made.

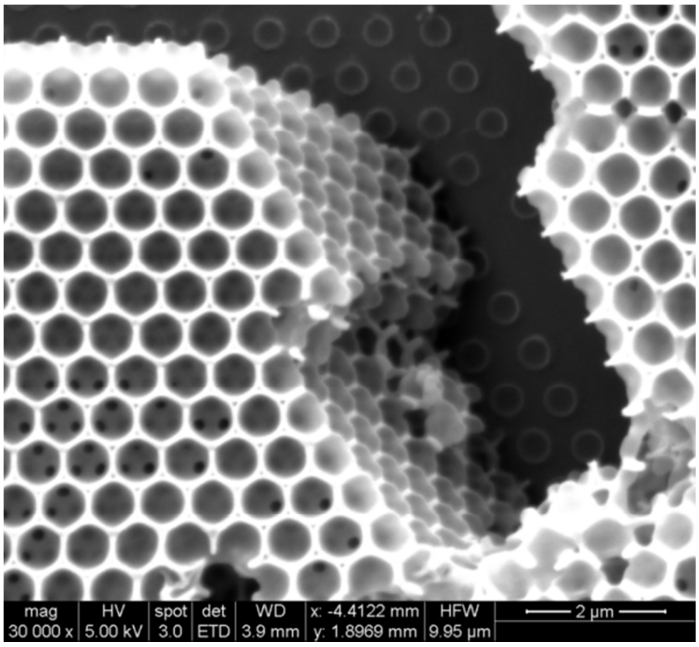

Figure III-11: Inverse opal

Nishijima *et al.* [7] fabricated and characterized three dimensional direct and invers opals using sol-gel process, and optically analyzed the samples. The polystyrene direct opals were created by a centrifugation method. The inverse opals were made by the impregnation of tetraethyl-orthosilicate sol. After the drying process, the polystyrene balls were eliminated from the structure using ethyl-acetate. The thickness of each film was about 100 µm.

Polystyrene was used for the elaboration of direct opal by the group of Caicedo in vertical deposition method [48]. The inverse opal was created by dip-coating into the Al_2O_3 suspension. After this step the polystyrene balls were eliminated by Toluene.

Author	Sphere type	Deposition Technique	Sphere elimination
Waterhouse[66]	**PMMA**	**SiO_2 or TiO_2 or CeO_2 by sol-gel**	**Calcination**
Cao[67]	**Polystyrene**	**Titania**	**Calcination**
Abramova[68]	**Polystyrene**	**ZNO**	**Calcination**
Jin[69,70]	**Polystyrene**	**Cerium doped barium titanate or Cerium doped titania**	**Calcination**
Nishijima[7]	**Polystyrene**	**TEOS inverse opal**	**Ethyl-acetate**
Caicedo[48]	**Polystyrene**	**Dip-coating method into Al_2O_3 colloid suspension**	**Toluene**

Table III-1: Works of the elaboration of inverse opals

These works (***Table III-1***) are interesting for us, because they prove that sol-gel process can be used of the elaboration of the 3D inverse opals.

Creating the inverse opal in the way of the “bottom-up” method, employing polystyrene opal, because of the easy elimination and sol-gel process due to the wide range of material utilization, open the opportunity of easy and low temperature realization of a new 3D MPC.

III.2. Elaboration of 3D opal based Photonic and Magneto-Photonic Crystal

This part deals with the chosen elaboration methods of the three dimensional artificial opals. Firstly, it will explain the used material as a direct opal and its properties. Secondly, it will present the sol-gel low temperature method for the elaboration of the impregnated direct opal. Finally, the elimination of the direct opal template is presented.

III.2.1. Properties of polystyrene sphere

The chosen direct opal material is the polystyrene in aqueous dispersion. The chosen process is the vertical deposition. This part explains the properties of the used material and the difficulties of the used technology of the realization of the direct opal.

III.2.1.1. Material of the direct opal

On the base of the work of Nishijima [7], polystyrene (Poly(1-phenylethane-1.2 diyl) was chosen for the creation of the direct opal.

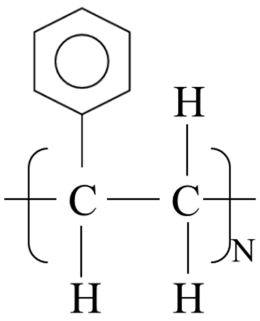

Figure III-12: Schema of polystyrene

Polystyrene ($(C_8H_8)_N$) consists carbon and hydrogen elements, where N is the repetition of the monomer (***Figure III-12***). For the direct opal template, this aromatic hydrocarbon was ordered from Thermo Scientific with the mean diameter of the spheres 400, 453, 799 and 903 nm, respectively. The microsphere density is 1.05 $g \cdot cm^{-3}$. The refractive index at 589 nm is 1.59. The approximate concentration is ~1 % solid.

III.2.1.2. Solubility of the polystyrene spheres

The elimination of the direct opal is essential for the realization of the inverse opal. Polystyrene template is removable with aromatic and chlorinated solvents, like Benzene, Chloroform, Carbon Tetrachloride, Cyclohexane, Dimethylformamide, Methylene Chloride, Pyridine, Tetrahydrofuran, Toluene, Xylene and Ethyl-Acetate [7,71,72].

Polystyrene can be eliminated from the composite material with calcination in high temperature up to 400-500 °C [73–78].

For the realization of inverse opal, we used Ethyl-Acetate acid, in order to keep a low temperature process.

III.2.2. Sol gel process

A Sol is a liquid colloidal suspension with solid, <1 micron size solid particles in dispersed phase.

Gel means a substance which contains solid cadre to cover the continuous liquid phase. The continuous skeleton gives elasticity to the gel. The gel contains also solid and fluid phases in colloidal dimension.

But the definition of Sol-Gel is a process where the colloid liquid suspension becomes solid polymer chain by the reaction of 1) hydrolysis and 2) condensation.

The most thoroughly studied precursor material for sol-gel procedure is tetraethyl-orthosilicate (TEOS=$Si(OC_2H_5)_4$). This is a metal alkoxide (organometallic compound), which contains metal atoms. $Si(OR)_4$ ($R=C_2H_5$) is a good precursor for sol-gel process due to the easy compatibility with water.

1) Hydrolysis:

$$Si(OR)_4 + H_2O \rightarrow HO - Si(OR)_3 + R - OH \qquad \text{Eq III.5}$$

In a case of complete hydrolysis Si loses all of its alkyl groups and becomes $Si(OH)_4$:

$$Si(OR)_4 + 4H_2O \rightarrow Si(OH)_4 + 4ROH \qquad \text{Eq III.6}$$

2) Polycondensation:

From the first reaction equation, the partially hydrolyzed HO-$Si(OR)_3$ bonds with each other create siloxane bond [Si-O-Si] in the condensation reaction:
Water condensation or oxolation:

$$(OR)_3 - Si - OH + HO - Si - (OR)_3 \rightarrow [(OR_3Si - O - Si(OR)_3] + H_2O \qquad \text{Eq III.7}$$

Alcohol condensation or alcoxolation:

$$(OR)_3 - Si - OR + HO - Si - (OR)_3 \rightarrow [(OR_3Si - O - Si(OR)_3 + ROH] \qquad \text{Eq III.8}$$

Due to the step of condensation, water and ROH alcohol molecules leave the system. [(OR_3Si-O-Si($OR)_3$] silicon-containing molecules join together by a polymerization step and build polymer macromolecules [79,80].

III.2.2.1. Preparation of TEOS solution

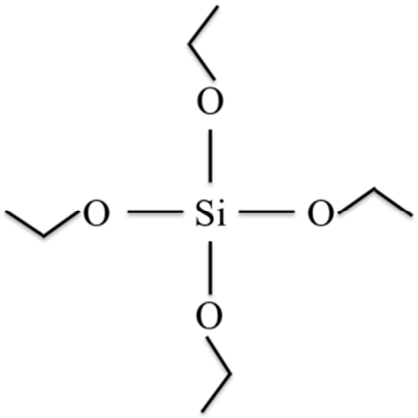

Figure III-13: Schema of Tetraethyl-orthosilicate

Tetraethyl-orthosilicate ($Si(OC_2H_5)_4$) (***Figure III-13***) was used as alkoxide for the sol-gel process (***Table III-2*** and ***Table III-3***). The alkoxysilane was diluted in alcohol before the step of the hydrolysis.

Name of the reagents	Purity
TEOS (tetraethyl-orthosilicate ($Si(OC_2H_5)_4$)	**98 %**
Ethanol (C_2H_5OH)	**98 %**
HCl (acid)	**0.01 N**

Table III-2: Sol-gel reagents

The respected molar ratio is:

$$\frac{n_{TEOS}}{n_{EtOH}} = 0{,}5 \qquad \text{Eq III.9}$$

where TEOS means tetraethyl orthosilicate and EtOH signs ethanol.

The alcohol was added to the alkoxide, because the water is not miscible with the alkoxysilane. In this way the EtOH alcohol is used as a homogenizing agent.

This solution was agitated during 5 minutes on a magnetic agitator with vigorous stirring. The hydrolysis was made by 0.01 N HCl.

The ratio between the water and alkoxysilane is:

$$\frac{n_{H2O}}{n_{TEOS}} = 2 \qquad \text{Eq III.10}$$

And the ratio between the alkoxysilane and hydrogen-chloride (HCl), which catalyze the reaction, is given as:

$$\frac{n_{TEOS}}{n_{HCl}} = 0{,}01 \qquad \text{Eq III.11}$$

where the HCl was calculated for 0,1 N for 1ml.

These latest ratio ensure that the catalyst gives viscous and spinnable solution [79].
He HCl was added carefully, drop by drop to the $Si(OC_2H_5)_4$-ethanol mix to avoid the fast gelification during the agitation. Then the solution was left for a night on the magnetic stirrer with moderate speed. This step is necessary to avoid the nascent bubbles which were presented because of the difficult assimilation of the HCl in the solution.

Name of the reagents	Quality (ml)
TEOS (tetraethyl-orthosilicate ($Si(OC_2H_5)_4$)	**6.17**
Ethanol (C_2H_5OH)	**3.417**
HCl (acid)	**1**

Table III-3: Used quantities of the elaboration of the TEOS "preparation" process

The molar ratio of the components was used by a work of Choi [81] as 1:2:2:0.01 ($Si(OC_2H_5)_4$:ethanol:water:HCl (0.01)).

III.2.2.2. Cobalt-ferrite nanoparticles ($CoFe_2O_4$)

Magnetic liquids (or ferrofluids) are colloidal suspensions of nanometric magnetic particles (≈10 nm) in a liquid. Isotropic in zero magnetic fields, these hybrid media acquire an optical anisotropy under the influence of a magnetic field. This anisotropy is circular in

Faraday's longitudinal configuration (magnetic field direction parallel to light beam) and linear in Voigt configuration (magnetic field direction perpendicular to light beam) [1,82].

The cobalt-ferrite based ferrofluid was synthetized by the coprecipitation of Co(II) and Fe (III) hydroxides [83]. This step was followed by a thermal treatment at 100 °C until 2 hours and it was washed with distilled water three times. To facilitate the incorporation of the magnetic particle nitric acid was added to the solution. As a last step the nanoparticles were dispersed into deionized water.

The result of the synthesis is shown in the ***Table III-4***.

Cobalt-ferrite (S 403-A)	
Volume fraction	**7 %**
Mean diameter of the particles	**9 nm**
PH	**4.2**

Table III-4: Properties of the used cobalt-ferrite ferrofluid

III.2.2.3. Sol-Gel Doping

This method is very interesting for the waveguide technology due to its relatively low temperature utilization. This procedure is compatible with the classical integrated technology like glass [84]. This technique is already utile either in the application of integrated optic or the realization of inverse opals.

To introduce magnetic particles in the sol-gel solution, we have to pay a good attention on the stability of the particles in order to avoid aggregation or sedimentation. This could introduce scattering of light and do not allow a good impregnation of the direct opal.

Thus, the magnetic solution is added dropwise to the TEOS solution, which was frequently stirred with a non-magnetic stirrer and ultrasonic bath was also applied.

Finally, the doped solution is passed through a 0.2 µm filter and is immediately used for the infiltration of direct opal.

III.2.3. Realization of Photonic and Magneto Photonic Crystal

We will present here the elaboration process used for the entire collection of sample studied during this thesis. There are five main steps:

- The preparation of the substrate
- The vertical deposition
- The impregnation with doped or undoped TEOS preparation
- The drying process
- The elimination of the polystyrene spheres from the matrix

III.2.3.1. Preparation of the substrate

For the realization of the direct and inverse opals Borosilicate (Neyco B270: crown glass which was manufactured by the up-draw procedure and it was polished by both sides. It has high transmission in the visible wavelength range.) and simple microscope glass slides were used. The dimension is: 25x75x1 mm.

The surface cleaning is a very important step of the realization of the direct opal. Both hydrophilic substrates have to be perfectly clean without contamination to attract the polystyrene spheres to its surface. The substrate was dipped for 10 minutes into the acetone, ethanol and distilled water using the ultrasonic bath. The substrate was dried with nitrogen gas. As the last step the substrate was cleaned with ethanol using Joseph papers [85,86].

III.2.3.2. Vertical deposition (VD)

The vertical deposition (***Figure III-14b***) was chosen as the elaboration of the direct opal. The realization of this method is easy and cheap even for industrial fabrication. Moreover it produces the nicest results among the elaboration method of self-assembly.

The volume fraction of the direct opal was made between 0.05-0.3 % wt (***Figure III-14a***).

The inclination of the cleaned substrate was set at 20 ° with the respect of the vertical on a base of work of Lopez *et al.* [54]. The temperature was stabilized until the evaporation correspondingly with the diameter size of the chosen polystyrene spheres (***Table III-5***).

d_{sph}	<700 nm	>700 nm
Drying temperature	**45 °C**	**50 °C**

Table III-5: Drying temperature as a function of a polystyrene sphere diameter

The evaporation time depends of the quantity and the volume fraction of the polystyrene dispersion. The thickness of the direct opal can be controlled by the volume fraction of the polystyrene dispersion.

III.2.3.3. Doping

The cobalt-ferrite nanoparticles are introduced in the Teos preparation liquid solution. Because of the acidic PH of the ferrofluid (PH=4.2), to avoid the aggregation and precipitation of the ferroparticles the magnetic fluid was diluted with the same solvent as the original solvent of the ferrofluid; with water. Until PH 5.6 the ferrofluid is homogeneous. This diluted magnetic solution was invited into the Teos sol-gel solution. The compound is then agitated and ultrasonicated.

III.2.3.4. Impregnation

The direct opal is introduced into the Teos preparation solution by dip-coating method (***Figure III-14c***). The opal was hanged on a sample holder which was moving down into the solution with the stable speed. The impregnation time was 10 minutes. After the opal template was drawn out with the slowest speed of the motor of the sample holder to avoid the creation of the monolayer above the impregnated opal. The opal was dried in 90°C during 1 hour (***Figure III-14d***) [7].

III.2.3.5. Elimination of the polystyrene spheres from the silica opal

The polystyrene spheres were removed from the impregnated sample using ethyl acetate (Et-Ac) [7]. This was achieved by dipping the sample into a beaker containing Et-Ac for one hour (***Figure III-14 e, f***).

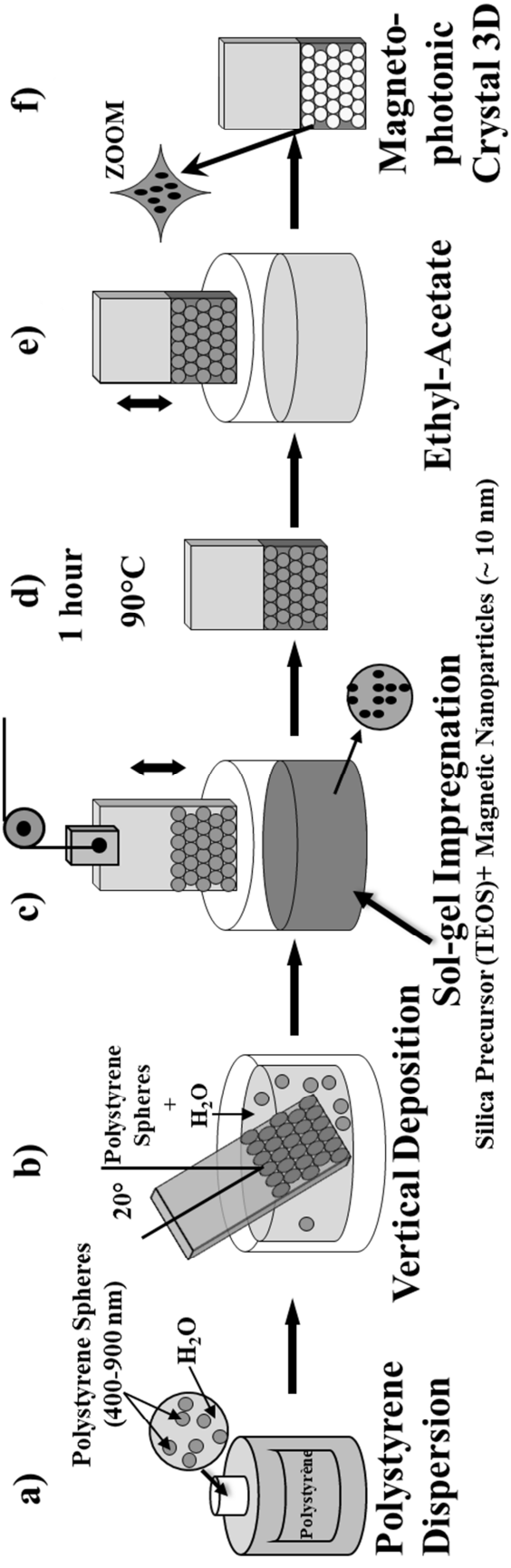

Figure III-14: Realization procedure of the magnetic inverse opal

III.3. Characterization

This part will list the used equipment for the characterization of the 3D magnetic and non-magnetic opals. For the visualization of the nanostructure we used Scanning Electron Microscopy. The thickness of the monolayers was measured with an ellipsometer. Finally, the Faraday rotation was determined with Free Space Ellipsometer for the measurement as a function of magnetic field, and with a Spectral Polarimeter for the measurement as a function of wavelength.

III.3.1. Scanning Electron Microscope (SEM)

For the image analyzing FEI Nova NanoSEM 200 equipment was used (***Figure III-15***).

Figure III-15: FEI Nova NanoSEM 200

High energy electrons are used, as a focused beam, to scan the specimen surface point by point in vacuum. In this electronic microscope low vacuum function is available, where the characterization of non-conducting or contaminating materials is possible.

The set-up of the equipment is shown in ***Figure III-16***, where electrons in the electron gun are emitted from the cathode and accelerated by the anode. The acceleration voltage in high and low vacuum is 15 kV and 3 kV, respectively. Magnetic field was produced by the scan coils. The electron beam was focused by the objective lens, which gives a very fine spot (1-5 nm). The resolution of this SEM in high and low vacuum is 1 nm and 1.8 nm, respectively.

Accelerated electrons carry significant amounts of kinetic energy. This energy is dissipated as a variety of signals produced by electron-sample interactions.

Secondary electrons and backscattered electrons are used for imaging samples. Secondary electrons are gave information about morphology and topography of the samples. Backscattered electrons are most valuable for showing the contrasts in composition in multiphase samples [87,88].

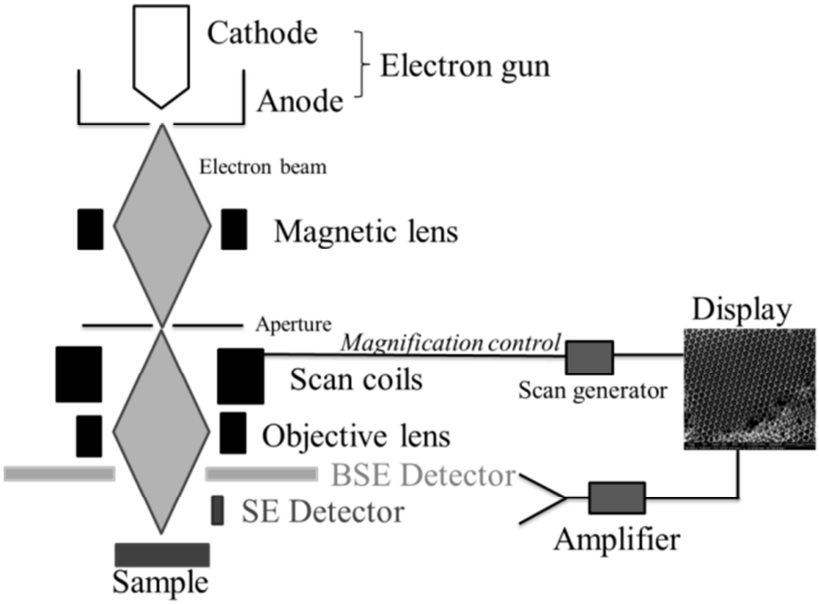

Figure III-16: SEM set-up

III.3.2. Ellipsometry

Dielectric function of materials is an important parameter in the field of photonic crystal. In order to obtain details on elaborated material, we have used ellipsometry technique, which is a powerful analysis tool of optical properties. It is based on the study of the modification of light polarization state upon a non-normal reflection (***Figure III-17***). This

modification is linked to the difference between p and s reflection coefficients (respectively parallel and perpendicular to the plane of incidence).

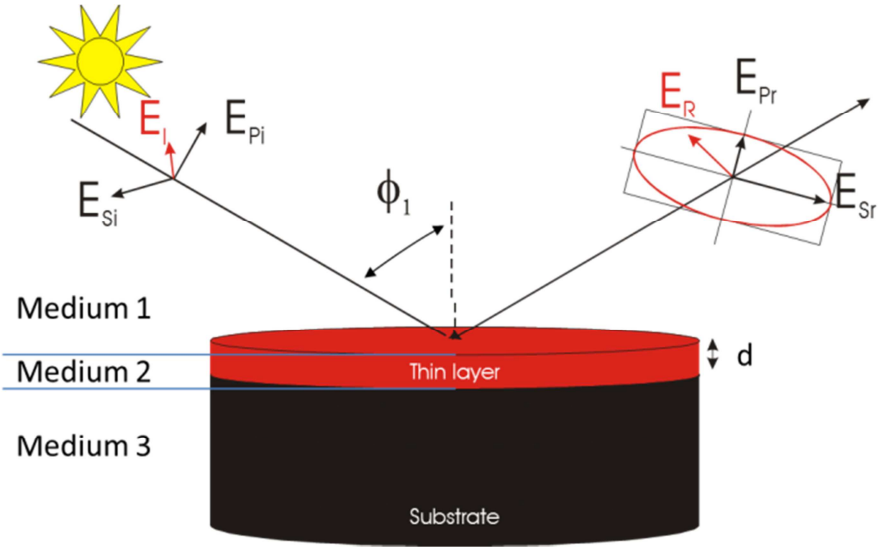

Figure III-17 : reflection of a polarized light on a thin layer

These coefficients denoted as R_p and R_s for a single layer, with d thickness, on a substrate, are given by:

$$R_k = \frac{r_{12}^k + r_{23}^k \cdot e^{-2i\beta}}{1 + r_{12}^k \cdot r_{23}^k \cdot e^{-2i\beta}} \qquad \text{Eq III.12}$$

where $k = p \; or \; s$, and:

$$r_{ij}^p = \frac{n_j \cdot \cos\Phi_i - n_i \cdot \cos\Phi_j}{n_j \cdot \cos\Phi_i + n_i \cdot \cos\Phi_j}$$

$$r_{ij}^s = \frac{n_i \cdot \cos\Phi_i - n_j \cdot \cos\Phi_j}{n_i \cdot \cos\Phi_i + n_j \cdot \cos\Phi_j} \qquad \text{Eq III.13}$$

$$\beta = \frac{2 \cdot \pi \cdot d}{\lambda} \cdot n_2 \cdot \cos(\Phi_2)$$

r_{ij}^k is the reflection coefficient of the ij interface, Φ_i the angle of incidence, β the phasechanging and n_i the refractive index of medium i.

The ρ ratio of the reflection coefficients R_p and R_s can be expressed as:

$$\rho = \frac{R_p}{R_s} = \tan\psi \cdot e^{i\Delta}$$ Eq III.14

Where ψ and Δ are the two angles measured by an ellipsometer.

Thus, by the measure of these two parameters as a function of the wavelength, one can determine the dispersion of the refractive index and the other the thickness of the layer. This is performed by adjusting parameters of the theoretical model to the experimental data via an optimization process (Levenberg-Marquardt algorithm [89,90]).

The determination of the optical properties of our samples has been carried out by a phase-modulated spectroscopic ellipsometer (Jobin Yvon UVISEL) in the photon energy range from 0.70 to 4 eV with a step of 0.02 eV, showed on ***Figure III-18***. The incidence angle of the light source was 60.00°

Figure III-18 : Jobin-Yvon UVISEL ellipsometer

III.3.3. Optical and magneto-optical characterization

The most important part of this research is the measure of the magneto-optical effects. The 3D magnetic opals were analyzed by Spectral Polarimeter. In the next part the function of these optical benches will be explained.

III.3.3.1. Description of the optical bench

The optical and the magneto-optical properties of the prepared samples were measured with a spectral polarimeter (***Figure III-19***). It consists of a tungsten-halogen light source, a polarizer, a sample holder attached to a XY θ stage ***Figure III-19***, a modified microscope which allows the inspection of the focus area. This last contains an analyzer, for polarization measurement. Finally beam splitter carries out the spectral analysis via a CCD spectrometer.

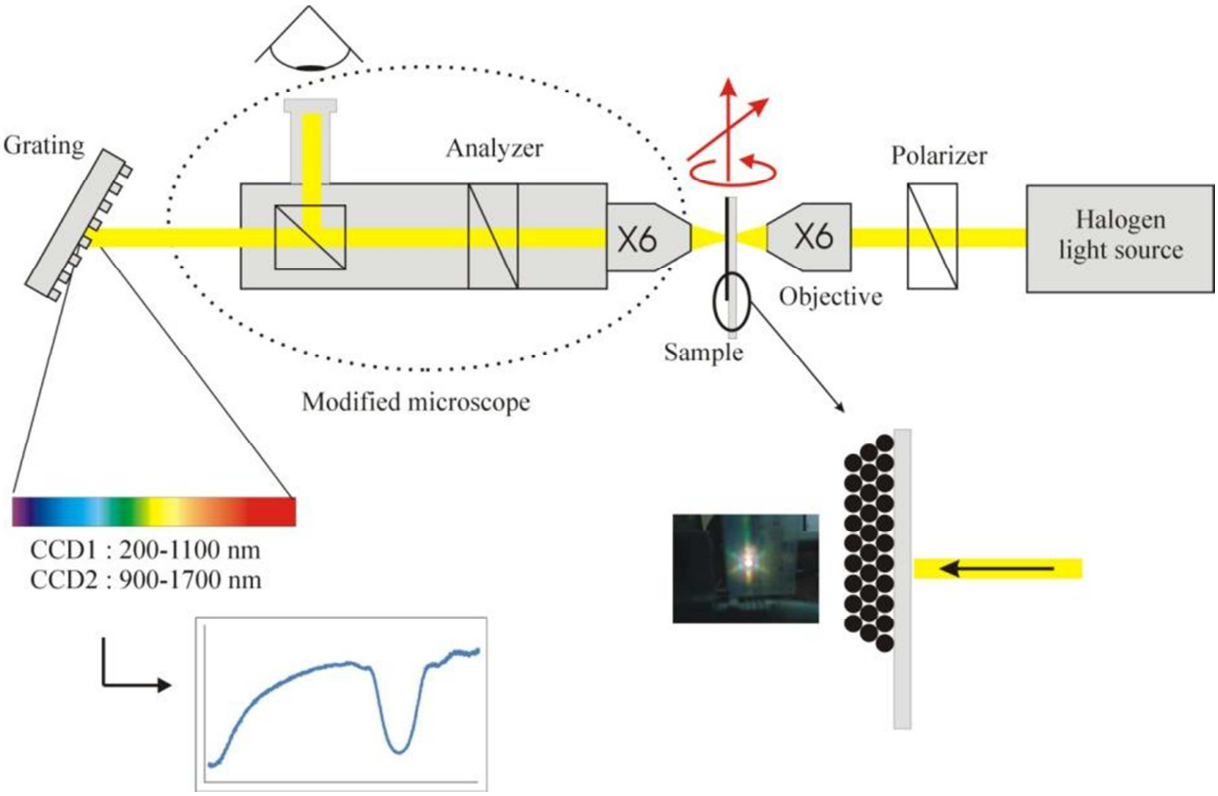

Figure III-19 : Spectral Photo-polarimeter

The 10W Tungsten-halogen light source (HL-2000) and the two spectrometers (MAYA and Nirquest512) were purchased from Ocean Optics. The light source covers the 360-2000 nm spectral range. Maya spectrometer is used in the visible-NIR (200-1100 nm) spectrum, whereas the Nirquest512, based on an InGaAs array detector, can be used in the 900-1700 nm wavelength range.

The two polarizers are high quality Glan-Thomson prisms with an extinction ratio better than 10^{-5}.

The sample holder is attached to a XY translation stage in order to scan the whole surface of the sample. A rotation stage is used to control the angle of incidence.

For magneto-optical measurements, a Neodymium Iron Boron (NdFeB) N45 magnet is placed in the vicinity of the sample. According to the distance between the spot and the magnet, a longitudinal magnetic field up to 350 mT can be applied to the sample.

III.3.3.2. Transmittance measurement

Stop band of photonic crystals can be revealed using transmission spectroscopy. The measurement of the transmittance is realized in the whole spectral range using the setup described above. This can be achieved as a function of the angle of incidence. The reference signal is issued from the measurement of the substrate. Integration time of the spectrometers and number of measurements are adjusted to optimize the signal to noise ratio.

The measurement of the transmittance can give some important information. Indeed, the position of the photonic band gap can be estimated using modified Bragg's law, which takes into account of the refraction of the light at the surface of the sample (***Figure III-20***):

$$\lambda_C = 2 \cdot d_i \sqrt{n_{Eff}^2 - \sin^2 \theta} \qquad \text{Eq III.15}$$

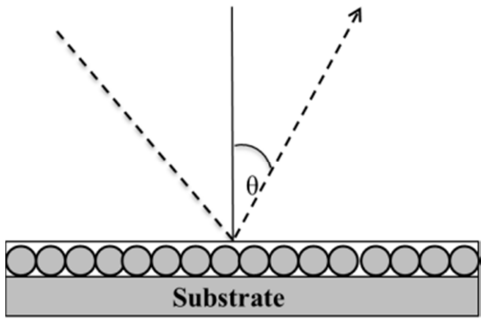

Figure III-20: Schema of the incident light beam on the sample surface

Thus, by plotting λ_c^2 as a function of $\sin^2 \theta$, a straight line should be obtained :

$$\lambda_c^2 = -4 \cdot d_i^2 \cdot \sin^2 \theta + 4 \cdot d_i^2 \cdot n_{Eff}^2 \qquad \text{Eq III.16}$$

The slope ($-4 \cdot d_i^2$) gives the inter-planar spacing d_i, with a theoretical value of $\sqrt{\frac{2}{3}} \cdot d_{sph}$, and the interception of y-axis ($4 \cdot d_i^2 \cdot n_{Eff}^2$) allows the determination of the effective refractive index (n_{Eff}) of the structure.

III.3.3.3. Faraday rotation

The measurement of the spectral Faraday rotation is the most important characterization in this thesis. Indeed, the spectral behavior, in terms of Faraday rotation, of the magnetic nanoparticles should be modified by the 3D structure of the MPC. Using the described setup we can measure the transmission spectrum and the Faraday rotation in the same area. We will describe next, the polarization aspect of the optical bench, starting by the presentation of Jones formalism.

III.3.3.3.1. Jones formalism

Within the Jones formalism [29,91], polarized light can be represented as a 2 complex elements vector. If the light travels along in z direction, these elements describe the x y complex amplitude of the electric field.

$$\vec{U} = \begin{bmatrix} U_x e^{i\emptyset_x} \\ U_y e^{i\emptyset_y} \end{bmatrix} \quad \text{Eq III.17}$$

Intensity of light is given by the hermitian scalar product:

$$I = \vec{U}^* \cdot \vec{U} \quad \text{Eq III.18}$$

Linear optical elements can be represented as a 2 by 2 complex elements matrix (M). When the light passes through an optical element, the emergent light polarization is given by:

$$\overrightarrow{U_{out}} = M \cdot \overrightarrow{U_{in}} \quad \text{Eq III.19}$$

For more optical elements, the final transfer matrix is obtained by multiplying each M_n transfer matrixes of optical component starting by the last one:

$$\overrightarrow{U_{out}} = M_n \cdot \ldots \cdot M_2 \cdot M_1 \cdot \overrightarrow{U_{in}} \quad \text{Eq III.20}$$

The Jones matrix for a polarizer aligned along O_x is:

$$P_X = \begin{bmatrix} 1 & 0 \\ 0 & 0 \end{bmatrix} \quad \text{Eq III.21}$$

The rotation matrix, used to change the coordinate system is given by:

$$R(\alpha) = \begin{bmatrix} \cos\alpha & -sin\ \alpha \\ sin\ \alpha & cos\ \alpha \end{bmatrix} \quad \text{Eq III.22}$$

Usual polarization states are the linear and the elliptical ones. The Jones vector for a linear state of polarization making an angle θ angle with O_x axes is:

$$\vec{U} = \begin{bmatrix} cos\ \theta \\ sin\ \theta \end{bmatrix} \quad \text{Eq III.23}$$

The Jones vector of the elliptical polarization (with ε as ellipticity) making an angle θ angle with O_x axes is:

$$\vec{U} = R(\theta) \cdot \begin{bmatrix} cos\ \varepsilon \\ i\ sin\varepsilon \end{bmatrix} \quad \text{Eq III.24}$$

III.3.3.3.2. Determination of the Faraday rotation

We have used Jones's representation to evaluate incoming light intensity in the spectrometer.

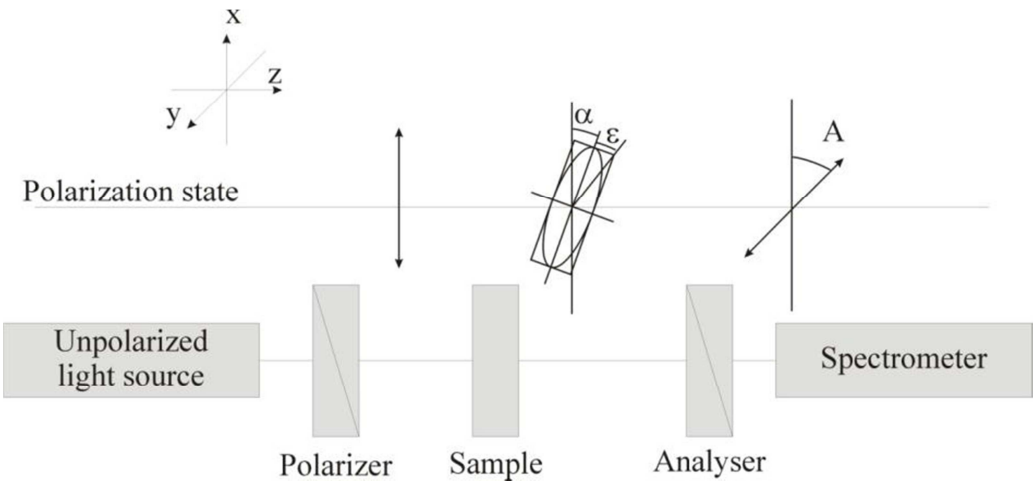

Figure III-21: Polarization considerations for the Spectral Polarimeter

Figure III-21 shows the evolution of the polarization state. The Jones vector of the light after the analyzer can be expressed as:

$$\vec{U} = \begin{bmatrix} 1 & 0 \\ 0 & 0 \end{bmatrix} \begin{bmatrix} cos(A-\alpha) & -sin(A-\alpha) \\ sin(A-\alpha) & cos(A-\alpha) \end{bmatrix} \begin{bmatrix} cos\varepsilon \\ i\ sin\varepsilon \end{bmatrix} \quad \text{Eq III.25}$$

$$\vec{U} = \begin{bmatrix} \cos(-A+\alpha)\cdot\cos(\varepsilon) + i\cdot\sin(\varepsilon)\cdot\sin(-A+\alpha) \\ 0 \end{bmatrix} \quad \text{Eq III.26}$$

where α and ε are respectively the Faraday rotation and Faraday ellipticity angle, and A the azimuth of the analyzer.

The intensity $I(\lambda)$ received by the spectrometer is:

$$I(\lambda) = \vec{U}^* \cdot \vec{U} \quad \text{Eq III.27}$$

$$I(\lambda) = I_0(\lambda) \cdot \left[\frac{1}{2} \cdot \cos(2\varepsilon) \cdot \cos(-2A+2\alpha) + \frac{1}{2})\right] \quad \text{Eq III.28}$$

As shown in ***Figure III-22***, the best azimuth for the analyzer is 45 ° because it gives the better sensibility. Moreover, values of Faraday rotation and ellipticity are small, so we can easily write:

$$\cos(2\varepsilon) \cong 1 \quad \text{Eq III.29}$$

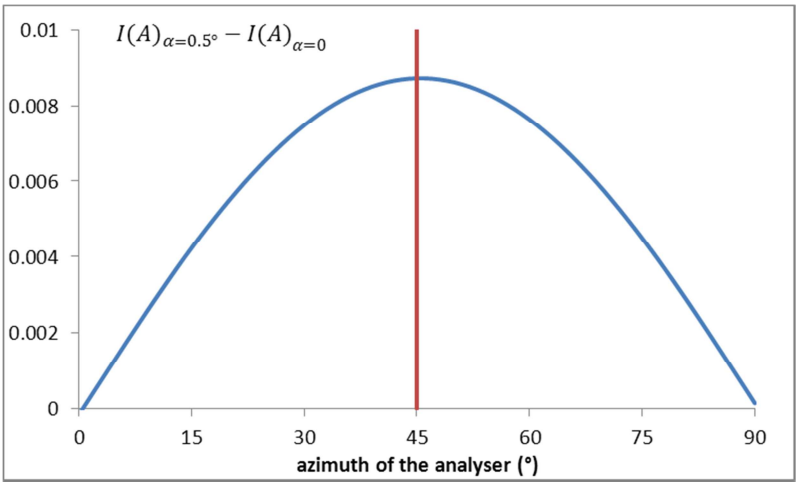

Figure III-22: sensibility of the intensity as a function the azimuth of the polarizer

So, the intensity can be expressed as:

$$I(\lambda) = I_0(\lambda)\left[\frac{1}{2} + \frac{1}{2}\cdot cos\left[\left(\frac{\pi}{2} - 2\alpha\right)\right]\right] \quad \text{Eq III.30}$$

Finally:

$$I(\lambda) = I_0(\lambda)\left[\frac{1}{2} + \frac{1}{2}\cdot \sin(2\alpha)\right] \cong I_0(\lambda)\frac{1}{2}[1 + 2\alpha] \quad \text{Eq III.31}$$

Faraday rotation is a nonreciprocal effect, thus, if we change the direction of the magnetic field, by a half turn of the magnet, the sign of the Faraday rotation changes. Let's note: $I(\lambda)^+$, $I(\lambda)^-$ and $I(\lambda)^0$, the measured intensity with a positive, a negative and without magnetic field, respectively. Then the Faraday rotation can be determined by:

$$\alpha = \frac{I(\lambda)^+ - I(\lambda)^-}{4 \cdot I(\lambda)^0} \quad \text{Eq III.32}$$

So, the measurement of the spectral Faraday rotation consists in the data gathering of three CCD spectra: out of magnetic field and under the two directions of the magnetic field spectrums. The interest of this method is that we can measure the transmittance and the Faraday rotation exactly at the same place.

III.4. Conclusion

In this chapter the potential techniques and materials were explained. From this explication, the chosen materials and technologies for this project were presented. For the

realization of the direct opal, the chosen elaboration is the vertical deposition on a use of self-assembly polystyrene in aqueous medium.

To fill the voids between the polystyrene impregnation technique was chosen, where the impregnated material magnetic and non-magnetic sol-gel silica (TEOS “preparation”). The chemical reaction of the sol-gel process was presented for the application of the Faraday rotator.

The polystyrene can be eliminated from the structure with different acids like Ethyl-Acetate, Benzene or Toluene, or with calcination procedure about 400-500 °C. High temperature process is not welcome in the realization of integrated elements. In this work, to eliminate the polystyrene balls Ethyl-Acetate was chosen.

Finally, the functions of the equipments of the characterization were explained, as Spectral Polarimeter, Ellipsometry and SEM (Scanning Electron Microscopy). The previous equipment gives information of the transmittance and Faraday rotation of the measured 3D MPCs. Ellipsometry provides the dielectric functions of the materials. The Scanning Electron Microscopy can visualize the nanostructure.

The demonstrated techniques and used materials were employed for the realization of 3D Magneto Photonic Crystals (MPC) or 3D Photonic Crystals (PC).

IV. CHAPITRE: Comportement magneto-photoniques des opales élaborés (resumé francais)

Des prototypes à base de cristaux magnéto-photoniques élaborés à basse température et contenant des nanoparticules de ferrite de cobalt devraient permettre l'augmentation de la rotation Faraday dans le domaine des télécommunications. Ce chapitre présente l'étude des propriétés magnétiques de monocouches de silice dopée avec du ferrite de cobalt, puis l'étude des opales directs et inverses, non dopés et enfin les caractérisations sur les cristaux photoniques 3D dopés.

Dans un premier temps, des films minces de ferrite de cobalt ($CoFe_2O_4$) sont étudiés en fonction du champ magnétique appliqué et de la longueur d'onde. Le ferrite de cobalt est inclus dans une matrice de silice. L'objectif est de montrer l'influence de la concentration volumique du $CoFe_2O_4$ par rapport au TEOS sur les propriétés magnétiques, mais aussi de comparer le comportement magnétique de ces films avec le ferrofluide d'origine à base de $CoFe_2O_4$. Les couches minces magnétiques ont été élaborées sur les bases du travail de Choueikani *et al.* [8].

Les parties réelle et imaginaire de l'indice de réfraction et l'épaisseur des monocouches ont été mesurées par ellipsomètrie. L'épaisseur des films minces est fonction de la concentration en matériau magnétique. Ainsi pour une concentration volumique importante, l'épaisseur du film est plus grande : pour des concentrations de 2:2 et de 2:5 (volume de $CoFe_2O_4$ sur volume de TEOS sol-gel), les épaisseurs sont respectivement de 337 nm et 247 nm. De plus, les parties réelle et imaginaire de l'indice de réfraction sont plus élevées pour les concentrations importantes de $CoFe_2O_4$. A partir de 700 nm, la partie imaginaire est quasi constante et est identique pour les différentes concentrations étudiées.

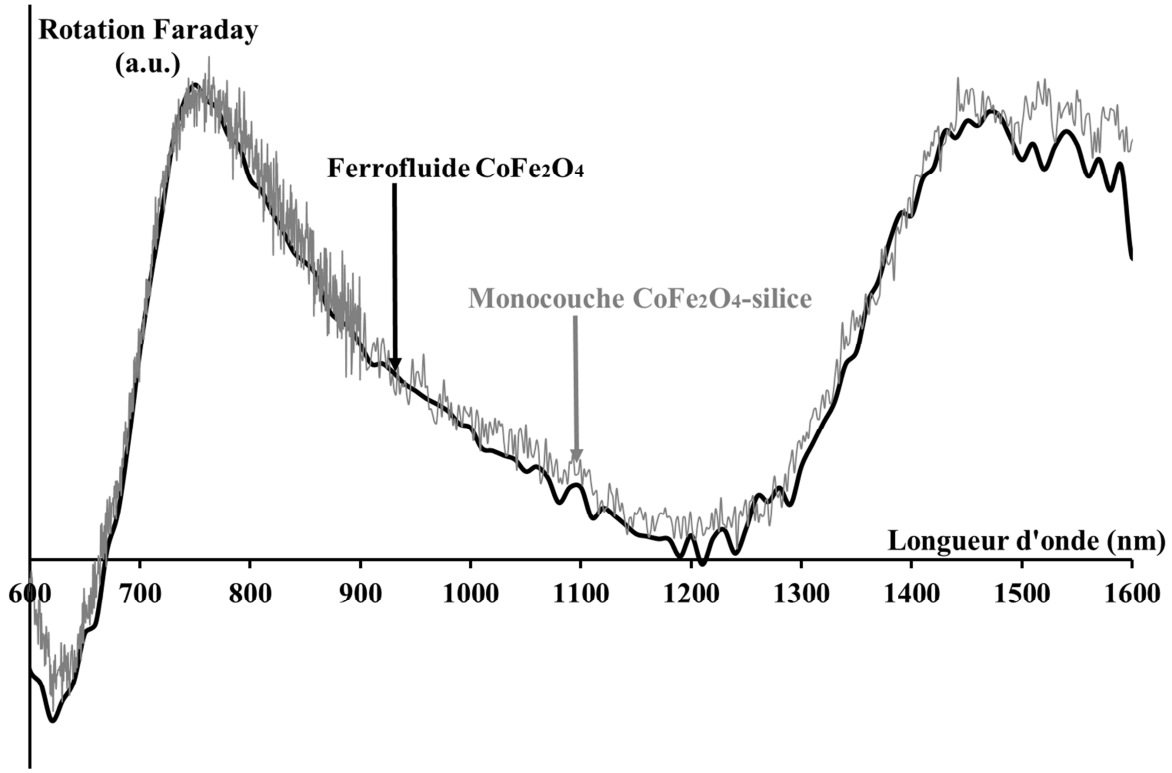

Figure 3.: Les courbes normalisé de rotation de Faraday de la monocouche de silice dopée par $CoFe_2O_4$et le ferrofluide $CoFe_2O_4$ en fonction de la longueur d'onde

La caractérisation de la rotation Faraday met en évidence que cette rotation dépasse 6700 °·cm^{-1} pour la concentration 2:2, alors qu'elle est de 1870 °·cm^{-1} pour 2:5 (à 820 nm). Il faut souligner que la plus forte concentration de 2:2 n'avait jamais été atteinte auparavant. Les graphiques donnant les rotations Faraday en fonction du champ magnétiques appliqués présentent pour toutes les concentrations étudiées des cycles d'hystérésis dus aux nanoparticules de $CoFe_2O_4$ comme l'a montré Choueikani *et al*.[8] Cet hystérésis devrait disparaître ou diminuer dans le cas où les nanoparticules magnétiques s'agrégeraient entre elles, le film serait alors inhomogène. Dans le cas de l'échantillon très concentré , la présence du cycle d'hystérésis met en évidence l'homogénéité des couches minces élaborées.

La comparaison de la rotation Faraday du ferrofluide avec les couches minces de TEOS dopées $CoFe_2O_4$ permet de confirmer que les nanoparticules de $CoFe_2O_4$ restent disperser de manière homogène (*Figure 3*).

Avant d'introduire le TEOS dopé dans une structure périodique, il est nécessaire d'étudier les propriétés optiques et l'organisation des opales directes et inverse non dopés. L'arrangement des billes de polystyrène constitue l'opale direct. Quatre dimensions de billes

de polystyrène ont été étudiées de 400 à 900 nm. L'organisation de cet opale est dite cfc, cette structure est à l'origine de l'apparition d'une bande interdite photonique (BIP). Le polystyrène est un matériau idéal pour la réalisation de l'opale direct par un processus d'auto-assemblage [6, 48, 67-70]. L'indice de réfraction du polystyrène, mesuré à 589 nm est de 1.59.

Le point suivant de ce travail est l'étude de l'influence de la taille des billes de polystyrène sur les propriétés. La mesure de la transmission optique en fonction de la longueur pour ces différents échantillons montrent un ou deux pics d'absorptions (1ère et 2eme harmonique de la loi de Bragg). Pour les échantillons élaborés, la longueur d'onde des centres des bandes interdites photoniques est proportionnelle au diamètre des billes de polystyrène. Ces longueurs d'onde peuvent être calculées avec la loi de Bragg (Eq .1). Les deux harmoniques obtenus par calcul sont légèrement plus faibles que les pics obtenus par les mesures. La loi de Bragg ne s'appliquant que sur des structures périodiques avec un arrangement précis, il est nécessaire de caractériser ces structures afin de mettre en évidence leur qualité structurelle.

$$\lambda_C = 2d_i\sqrt{n_{Eff}^2 - sin^2\theta} \qquad \text{Eq 2}$$

La mesure de la transmission optique sous différents angles d'incidence permet de déterminer la qualité optique des échantillons. La valeur réelle de la distance interplanaire et l'indice de réfraction effectif de l'échantillon peuvent être déterminés en utilisant la loi de Bragg modifié à l'aide de la loi de Snell (Eq 2), qui prend en compte l'angle de réfraction mesuré à partir de la normale. Par exemple, pour des billes de polystyrène utilisés ayant un diamètre de 453 nm, la distance interplanaire est évaluée à 370 nm et la taille des billes mesurées est de 454 nm. Cette étude met en évidence la conservation du diamètre des billes de polystyrène lors de l'élaboration. De plus, l'indice de réfraction effectif de l'échantillon est calculé à partir de la mesure et est égale à 1.41 à 1051 nm. Les billes de polystyrène ont un indice de réfraction de 1.59 à 589 nm.

La microscopie électronique à balayage a permis de mettre en évidence un arrangement cfc des billes de polystyrène (*Figure 4*) et une homogénéité pouvant atteindre 400µm².

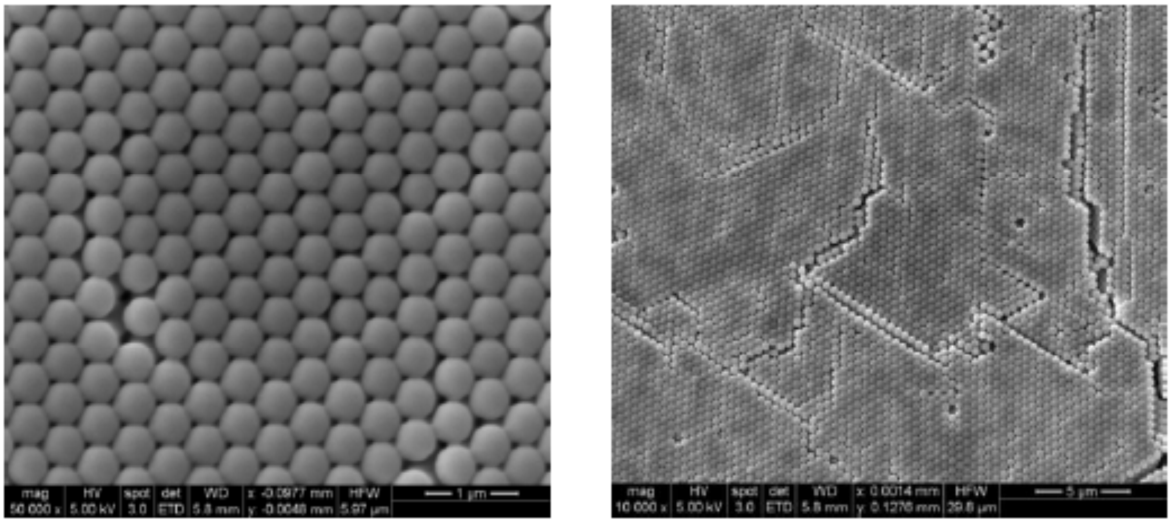

Figure 4. : Les images de la microscopie électronique à balayage des opales directes

Après sur la réalisation de l'opale direct, l'étape suivante est l'élaboration d'un opale inverse par imprégnation sol-gel avec une solution TEOS non magnétique. Les positions des BIP pour les opales directs sont différentes des positions des opales inverses. Par exemple, pour des billes de polystyrène de 453 nm, les positions des BIP sont à 1030 nm pour l'opale direct et 760 nm pour l'inverse (*Figure 5*). Ce phénomène est dû à l'indice de réfraction effectif qui a changé, la proportion air/polystyrène n'étant plus la même. Les échantillons d'opale inverse possèdent toujours une BIP, la structure tridimensionnelle cfc est conservée lors du passage de l'opale direct en opale inverse. Cette remarque est valable pour les quatre diamètres de billes utilisés.

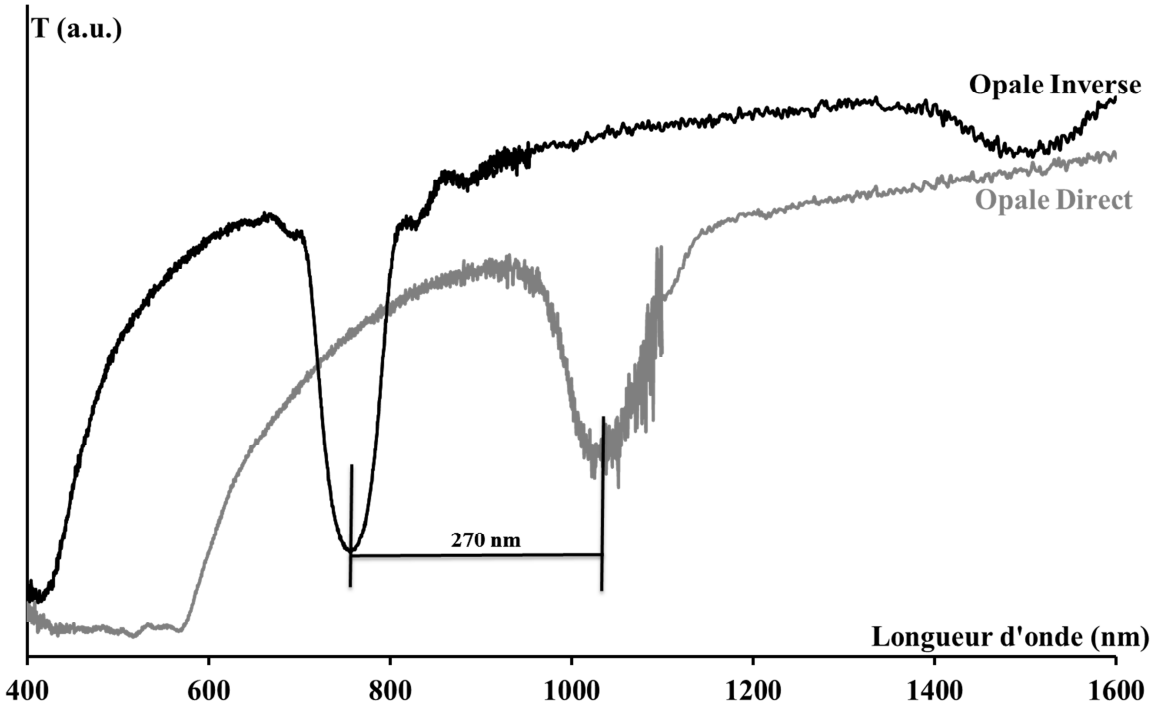

Figure 5.: Spectre de transmission de l'opales directe et inverse (les tailles des billes de polystyrène été 453 nm)

La transmission optique des échantillons montre des pics d'absorption correspondant aux BIP, calculées grâce à la loi de Bragg. Dans ce cas aussi, les deux harmoniques obtenus par calcul sont plus faibles que les BIP obtenues par les mesures. La position des BIP est proportionnelle à la taille des billes, même après imprégnation. De la même façon que pour les opales directs, l'indice de réfraction effectif et la distance interplanaire ont été déterminés. Le diamètre des empreintes des billes est de 708 nm, pour des billes de 800 nm par exemple. Ceci est certainement dû à la contraction de la matrice de silice pendant le séchage [6]. L'indice de réfraction effectif du matériau composite est égale à 1,08, l'indice de la silice est alors calculé et est égal à 1,28. En comparaison l'indice de la silice est de 1,44.

Enfin, des échantillons sont élaborés à partir des billes de polystyrène et d'une solution de TEOS dopée avec du $CoFe_2O_4$, le dopage ayant lieu avant l'imprégnation de l'opale direct. La position du centre de la BIP est, dans ce cas, décalée en longueur d'onde (*Figure 6*).

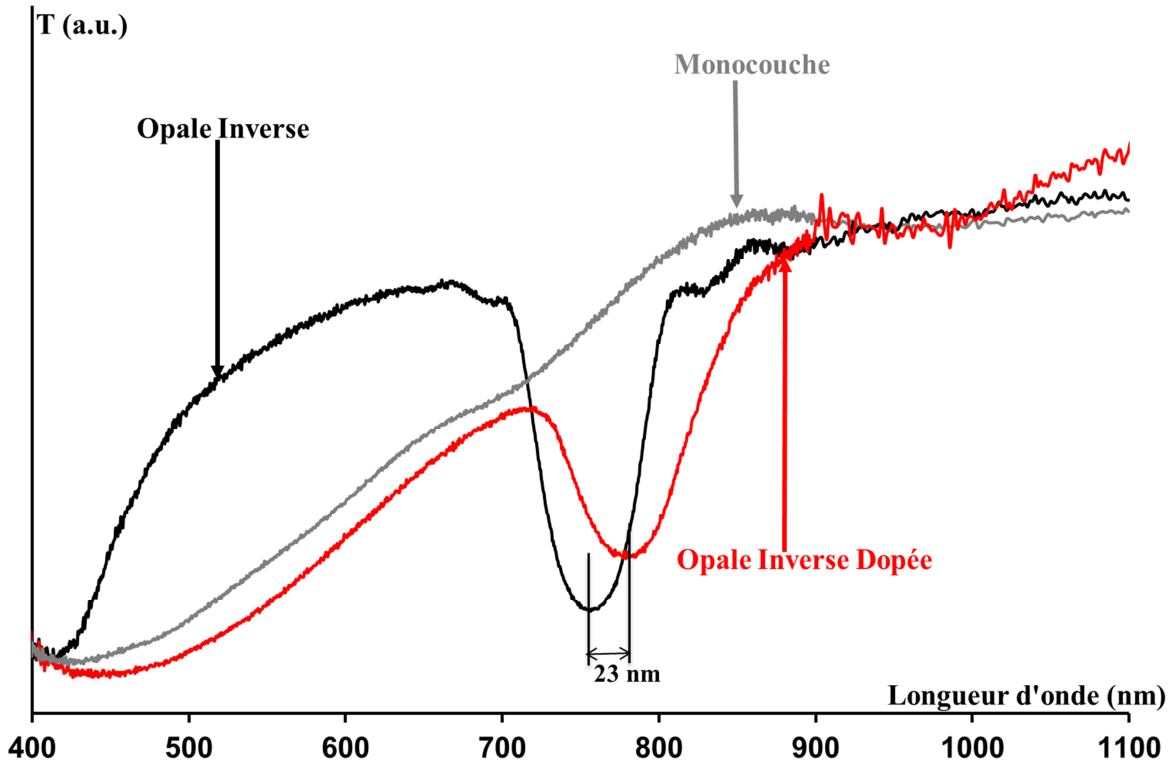

Figure 6.: Mesure de transmittance de la monocouche $CoFe_2O_4$ (monocouche 2:2), d'opale non-magnétiques et magnétiques inverses en fonction de la longueur d'onde (453 nm de taille d_{sph})

Le dopage contribue à une augmentation de l'indice de réfraction effectif de l'échantillon. La présence de BIP met en évidence que l'organisation du matériau reste de type cfc. Le comportement spectral de l'opale dopé apparaît comme un produit de la courbe correspondant à l'opale inverse non dopé et au spectre de la couche mince de TEOS dopée avec le ferrite de cobalt. L'influence de la structuration et du dopage est clairement visible.

Ces échantillons réalisés suivent aussi le comportement correspondant à l'équation de Bragg. Pour ces échantillons, la distance interplanaire et la distance entre les centres des sphères ont été déduites. Un retrait de 100 nm a été observé entre les mesures sur les opales inverses dopés et les opales directs. Ce résultat est identique aux opales inverses non dopés.

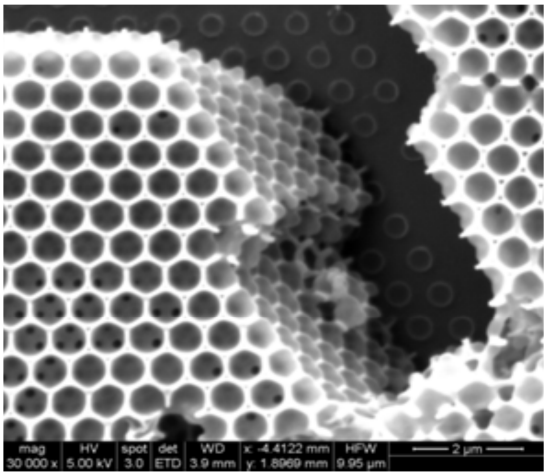

Figure 7.: Les images de microscopie électronique à balayage de l'opale magnetique

L'indice de réfraction effectif déduit des mesures ellispométriques est de 1,13 pour le matériau structuré. L'indice réel de la matrice de silice dopée au sein de l'opale inverse peut être calculée en supposant une structuration cfc et est égal à 1,43 pour une mesure réalisée autour de 1500 nm. Cette valeur d'indice est inférieure à celle déduite pour une couche de silice dopée (1,6 à 1100 nm). Cette différence a été aussi observée pour les échantillons non dopés et peut être attribuée à une porosité de la matrice de silice.

Les images de microscopie électronique à balayage montrent une organisation de type cfc (*Figure 7*). Le matériau réalisé est homogène en surface (sur environ 80 µm²) et en profondeur. Les images prouvent que la structure cfc a été maintenu pendant toute la procédure de l'élaboration.

La polarimètrie spectrale a permis de déterminer le comportement magnéto-photonique des opales inverses dopés dans une gamme de longueur d'onde de 400 à 1600 nm. Le spectre de la rotation Faraday de l'opale inverse dopé (courbe rouge) est très différent de la courbe de la rotation Faraday d'une monocouche dopée (courbe grise) dans la BIP centrée à 780 nm pour des billes de 453 nm de diamètre (*Figure 8*). En dehors de cette bande, les deux spectres de rotation peuvent être superposés, mais à l'intérieur de la BIP, un effet de résonance est observé. Sur le bord inférieur de la BIP, la rotation Faraday atteint une valeur minimale à 750 nm. Sur le bord supérieur, elle atteint une valeur maximale à 810 nm. Ainsi, la rotation Faraday est améliorée sur les deux bords de la BIP avec des valeurs maximales qui ont un signe opposé et une symétrique spectrale par rapport au centre de la BIP. Une telle amélioration sur les bords de la BIP pour un opale 3D dopé est similaire à ce qui a été obtenu par les calculs sur une structure 1D périodique. Ceci est le reflet d'un comportement magnéto-

photonique dû à une organisation périodique 3D. Ainsi, les opales inverses de silice dopée par des nanoparticules magnétiques ont la potentialité d'améliorer la rotation Faraday par rapport à une monocouche classique de la matrice identique dopée.

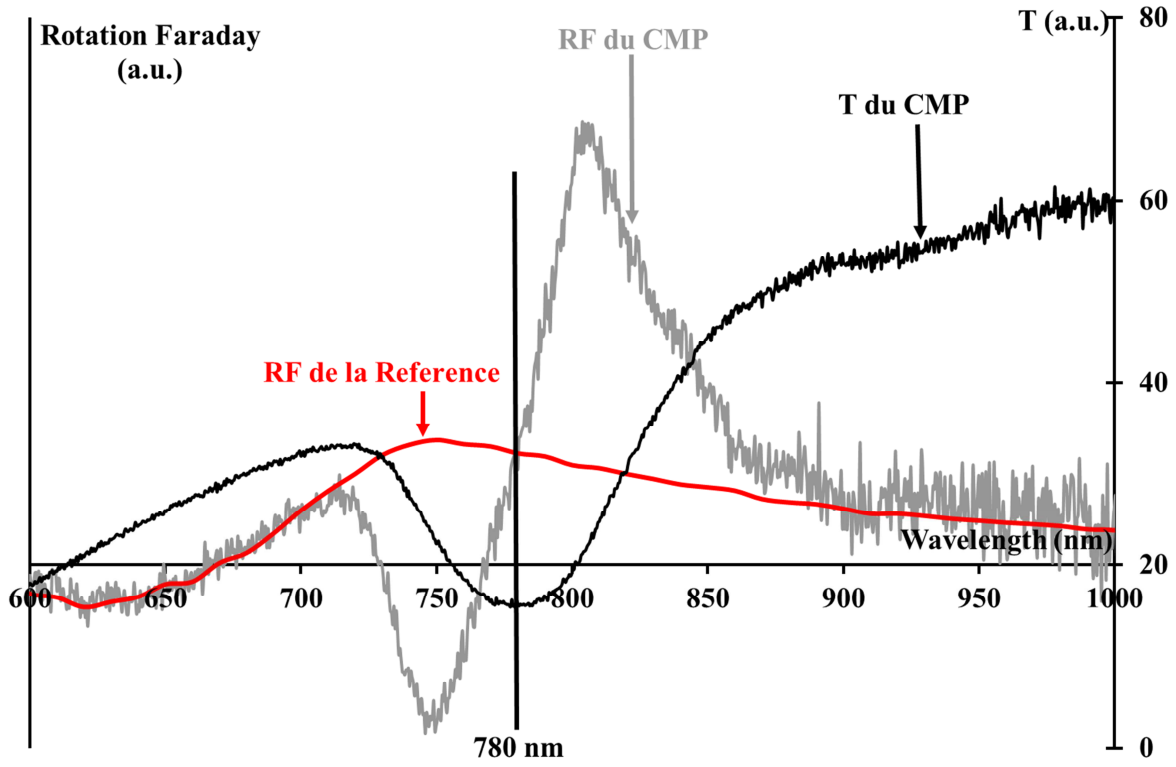

Figure 8.: Les spectres de Transmittance et de rotation de Faraday d'une opale dopé inversée basé sur un template 453 nm, et le spectre de rotation de Faraday d'une monocouche de cobalt-ferrite comme une référence

Cette étude a été étendue à des billes de polystyrène de différents diamètres. Le comportement de la rotation Faraday des opales inverse dopés pour ces différents diamètres de billes sont semblables à ce qui a été présenté précédemment. Ainsi, par rapport à la couche mince de référence, la rotation Faraday suit un comportement différent dans le domaine de la BIP. Il est intéressant de noter qu'avec les billes de polystyrène de 900 nm de diamètre, l'amélioration de la rotation Faraday se manifeste à une longueur d'onde autour de 1500 nm, correspondant au domaine des télécommunications. Dans le cas des billes de 799 nm de diamètre, la courbe de la rotation Faraday est donnée pour la seconde harmonique. En effet, la première harmonique se produit autour de 1200 nm, zone où l'activité magnéto-optique des nanoparticules de ferrite de cobalt est faible et donc aucun effet significatif n'a été mesuré.

Le comportement magnéto-optique est modifié pour le premier et second harmonique

sur les courbes de rotation Faraday. Ceci peut s'expliquer par l'étude analytique de la relation de dispersion $\omega - \vec{K}$ d'une structure périodique. Au bord des bandes interdites, les courbes de vecteur d'onde sont aplatis et la vitesse de groupe de l'onde diminue. Dans une telle situation, la différence du vecteur d'onde entre les polarisations droite et gauche est augmentée, entraînant l'amélioration de l'effet Faraday.

Un facteur de mérite, rapport entre la rotation Faraday et le coefficient d'absorption, a été déterminé. Cette valeur est relative, car il n'est pas possible d'obtenir une valeur absolue de la transmission. Dans le domaine extérieur à la BIP, les courbes du facteur de mérite de l'opale inverse dopé et de la monocouche dopée se superposent. Dans la BIP, le facteur de mérite du cristal magnéto-photonique a un comportement totalement différent. Ceci montre que le facteur de mérite peut être modifié et augmenté sur les bords de la BIP par rapport aux monocouches.

Ainsi l'objectif principal de cette étude qui était d'augmenter le facteur de mérite est partiellement atteint. Cette réalisation est partielle car la démonstration est basée sur une comparaison du comportement spectrale avec une monocouche classique. Une démonstration complète est requise pour obtenir une valeur absolue du facteur de mérite du CMP réalisé au laboratoire.

IV. CHAPTER: Optical properties of elaborated opals: Magneto-Photonic behavior

The previous chapter has detailed the protocol which is useful to realize silica inverse opals doped with cobalt ferrite nanoparticles, and the experimental tools which are required to study the physical, optical and magneto-optical properties of the samples. More than a hundred of opals and about fifty doped layers have been elaborated and studied during this work. The present chapter is dedicated to the results obtained through their study. It is divided into three main parts. The first deals with a specific study of the silica doped monolayers in terms of refractive index, Faraday rotation and especially the volume fraction of nanoparticles inside the matrix. In the second part, the main properties of direct and inverse non-magnetic opals are given in order to fix the ideas about the kind of sample we are able to realize, and the kind of properties we are able to reach. The last is concerned by the main results obtained during this work about the magnetic inverse opals through the presentation of their magneto-photonic behavior.

IV.1. Optical properties of doped silica monolayers

For a better understanding of the material which is the active core of the magneto-photonic crystals, this chapter starts with an analysis of silica monolayers doped by cobalt ferrite nanoparticles. Following the chemical protocol presented in section (III.2), four samples were made with constant quantity of ferrofluid but ascendant quantity of silica sol-gel solution. The incident liquid volume ratios were 2:2, 2:3, 2:4, and 2:5, respectively. The first element of the ratio denotes the $CoFe_2O_4$ ferrofluid quantity and the second signifies the TEOS sol-gel volume quantity. Thus, from 2:2 to 2:5, the amount of nanoparticles in the liquid initial preparation is decreasing. Using the dip-coating apparatus, layers were coated on glass substrate and submitted to a thermal annealing.

IV.1.1. Refractive index

The n refractive index, k extinction coefficient and the thickness of the monolayers were measured by Ellipsometer. The thicknesses of the layers from 2:2 to 2:5 liquid volume ratios are 337, 273, 249 and 247 nm, respectively. ***Figure IV-1*** shows that the refractive index is changing with the concentration of the magnetic nanoparticles in the samples. Based on the article of Xie[92] and Vincent[93] *et al*. Xie[92] and Vincent[93] *et al*, we can assess that undoped TEOS monolayers have a refractive index of about 1.44. The doping of the sol-gel solution with $CoFe_2O_4$ nanoparticles has clearly increased this value and ***Figure IV-1*** illustrates that with increasing the concentration of magnetic nanoparticles, the refractive index of the monolayers increases to reach a value as high as 1.8 at 400 nm for the 2:2 monolayer. As a consequence, k extinction coefficient is also increasing when the volume fraction (VF) of particles is increasing.

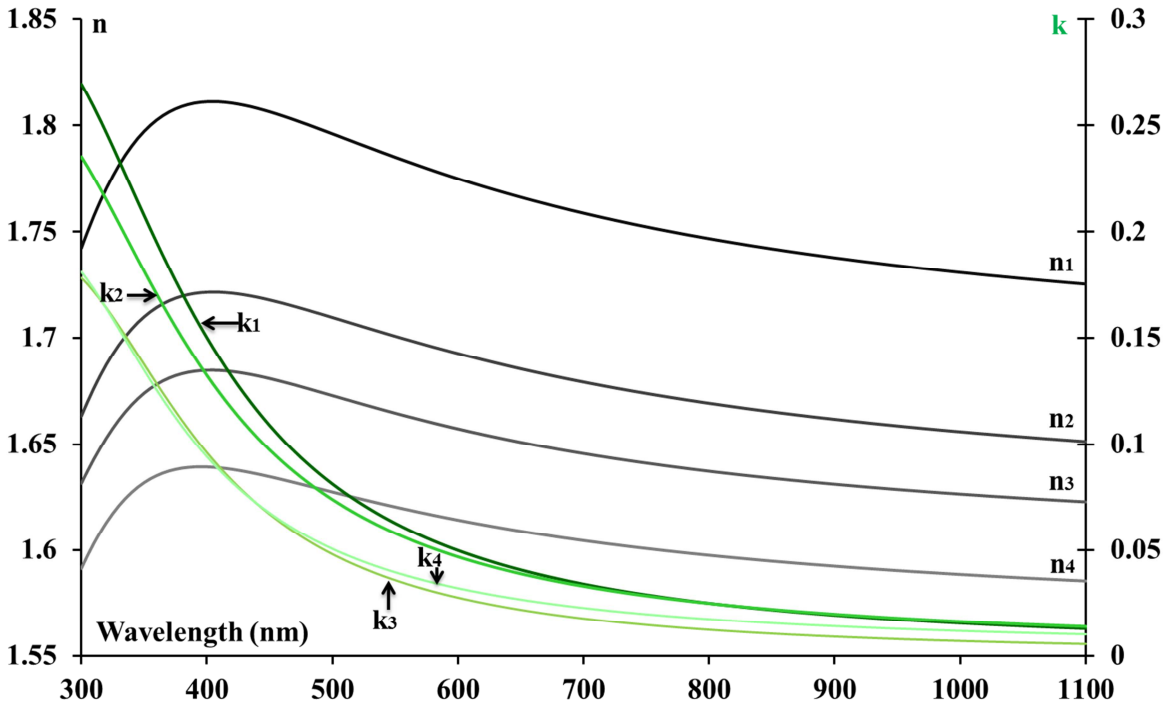

Figure IV-1: n-k graph as a function of the wavelength of cobalt-ferrite monolayers consisting different concentration of magnetic nanoparticles. 2:2, 2:3,2:4, 2:5 where the first value means the cobalt-ferrite and the second value is the TEOS sol-gel incident liquid VF

IV.1.2. Faraday rotation hysteresis loop

The Faraday rotation of the cobalt-ferrite doped monolayers was analyzed as a function of the magnetic field. The measurements were made using a free space ellipsometer based on a photoelastic modulation which proper frequency is 50 kHz. With such an optical configuration, the polarization rotation of an incident linearly polarized light is proportional to the second harmonic component (100 kHz) of the optical signal collected by a detector associated to a lock in amplifier. [28]. The sample under test is submitted to a longitudinal magnetic field with a strength varying from – 8000 Oe to 8000 Oe (-0.8 T to 0.8 T), and the measured rotation is the Faraday rotation. This kind of apparatus, which is quite usual in the laboratory for several years, is very sensitive (~ 0.001 °) but cannot offer a spectral measurement because it employs a laser source with a fixed wavelength (here 820 nm).

Figure IV-2 represents the specific Faraday rotation ($°\cdot cm^{-1}$) of the four monolayers measured at 820 nm. The behavior is classical with a linear slope at low fields, and a saturation at high field, the whole containing an hysteresis effect. The saturated rotations obtained at high field are 6703, 3120, 2767 and $1870°\cdot cm^{-1}$ when the volume ratio varies from 2:2 to 2:5.

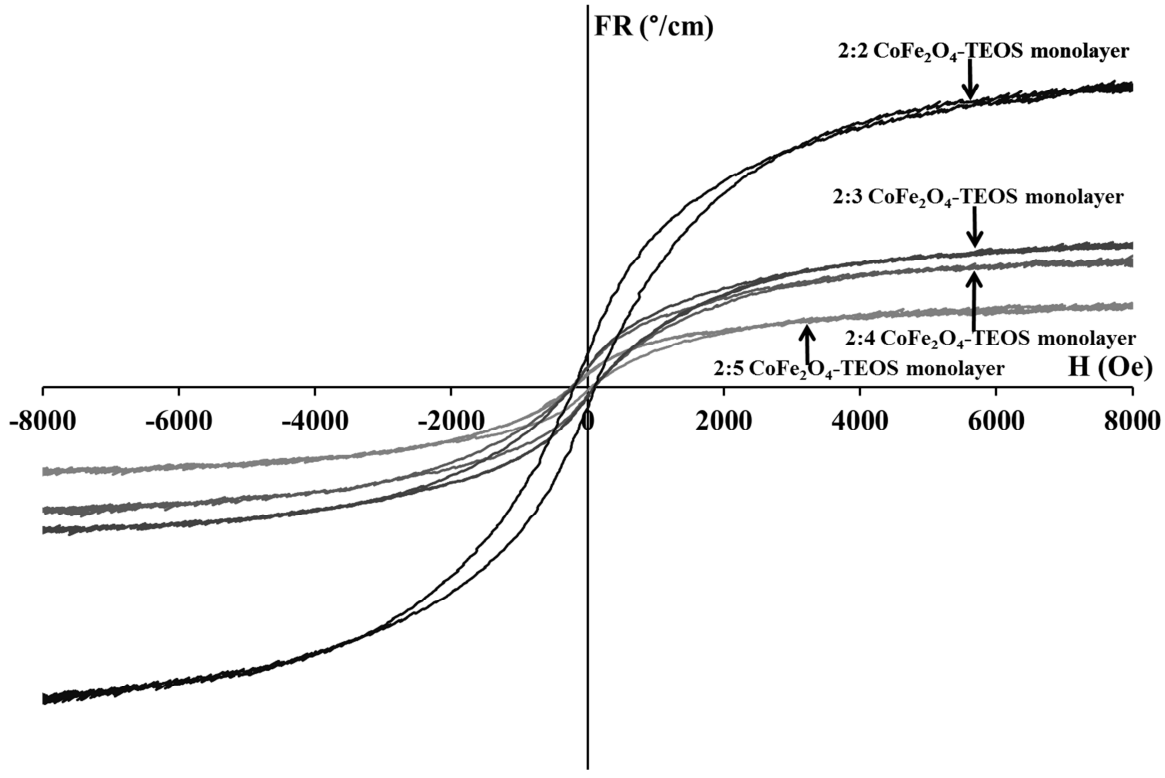

Figure IV-2: Faraday rotation curves of 4 different magnetic volume fraction monolayers (the measure was made at 820 nm)

Samples	Thickness (nm)	FR ($\frac{^\circ}{cm}$)	VF (%)
Ferrofluid		25	0.15
Monolayer 2:2	337	6703	42
Monolayer 2:3	273	3120	20
Monolayer 2:4	249	2767	17
Monolayer 2:5	247	1870	12

Table IV-1: Thickness, Faraday rotation and Volume fraction of the ferrofluid and the elaborated magnetic monolayers

Based on the previous work of the laboratory [1], we are able to calculate the volume fraction of the magnetic nanoparticles in the monolayers. Indeed, the saturated specific Faraday rotation of a composite material is proportional to the volume fraction of nanoparticles in the matrix. Furthermore, at 820 nm, a ferrofluid containing 0.15 % of cobalt-ferrite nanoparticles produces a saturated Faraday rotation of 25 $°\cdot cm^{-1}$. Thus, the volume fraction of nanoparticles in the silica matrix of the four layers has been calculated and reported in ***Table IV-1***. Such a volume fraction is varying from 12 to 42 %. This kind of value has never been reached before. It was no more than 2 %.

With such amounts of nanoparticles, one can wonder whether some aggregates may be present in the matrix and affect the propagation of light by inducing scattering. To study this assumption ***Figure IV-3*** was made by normalizing the curves from the previous graph. It shows that the four curves are fully superimposed and even if the volume fraction reach 40 %, the hysteresis loops maintains its form. This is the signature of an assembly of single nanoparticles with a random distribution inside the matrix without any aggregates, what confirms the good optical quality of the films.

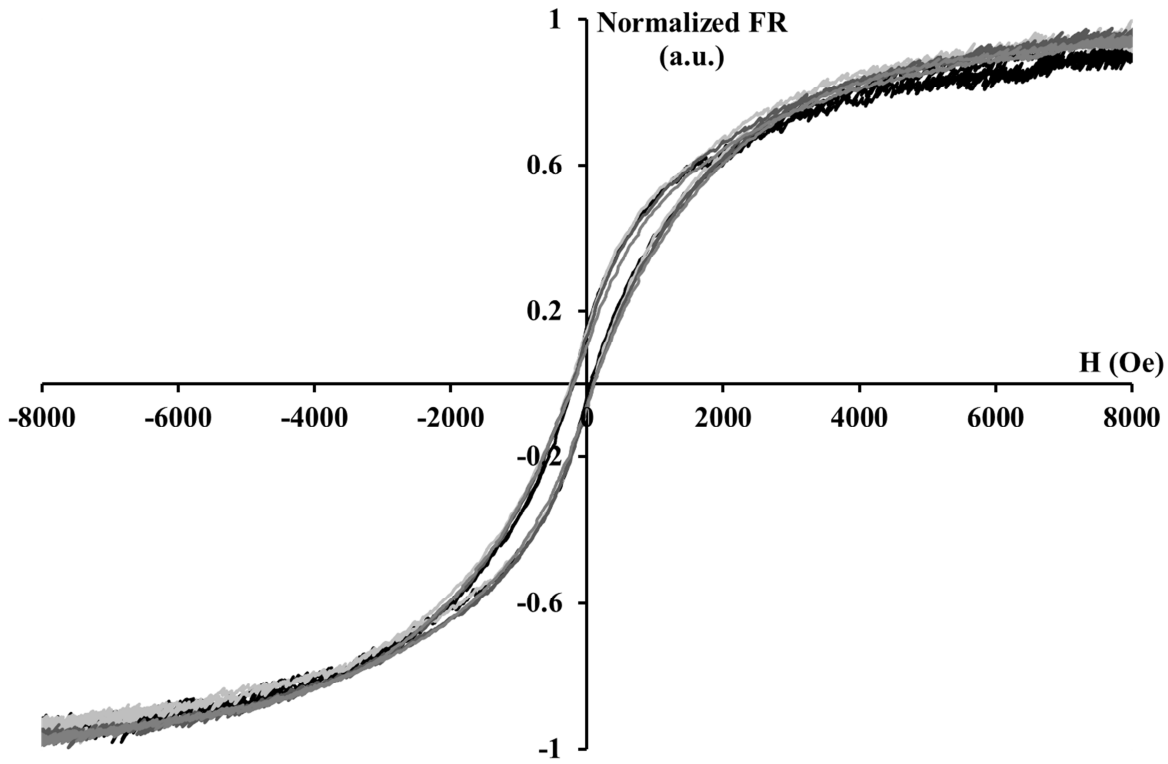

Figure IV-3: Normalized Faraday rotation curves of the four different volume fraction monolayers as a function of the magnetic field (measured at 820 nm)

Such a large amount of nanoparticles in the matrix (> 10 %) is a key element of the results obtained in this study. Indeed, in a doped inverse opal, 74 % of the volume is occupied by air. Thus, only 26 % of the volume can contribute to a magneto-optical effect. If the silica matrix has an amount of particles about 1 % as in the previous works of the laboratory, the whole Faraday effect may have been too weak to be detected by our apparatus. Thus, the large amount of nanoparticles in the matrix contributes to emphasize the magneto-optical effect and serves as a balancing of this “lack of active material”. Without such an amount of nanoparticles, it would certainly not have been possible to evidence the results presented in the last part of this chapter.

IV.1.3. Faraday rotation spectrum

It looks important to compare the Faraday rotation of the ferrofluid and the simple monolayer to check if the dispersion of the nanoparticles in the matrix has altered their properties compared to that obtained in the fluid. Thus, the measure of the FR of the ferrofluid and the doped layer was made with the spectral Polarimeter to analyze and compare their behavior. The ferrofluid in an aqueous medium contains cobalt-ferrite nanoparticles with a

volume fraction of 1 %. The used $CoFe_2O_4$: TEOS monolayer has 2:2 volume fraction ratio and 337 nm thickness. ***Figure IV-4*** presents the two FR curves as a function of the wavelength. Because of the different magnetic volumes fraction of the two samples, the graph of the monolayer was normalized to that of the ferrofluid.

Figure IV-4 shows that the two FR curves have exactly the same magneto-optical spectral behavior. In a magnetic material, this behavior is related to the electronic transitions of the magnetic ions and their crystallographic positions. Obtaining an identical behavior confirms that the structural properties of the nanoparticles is not affected by a dispersion in the silica matrix.

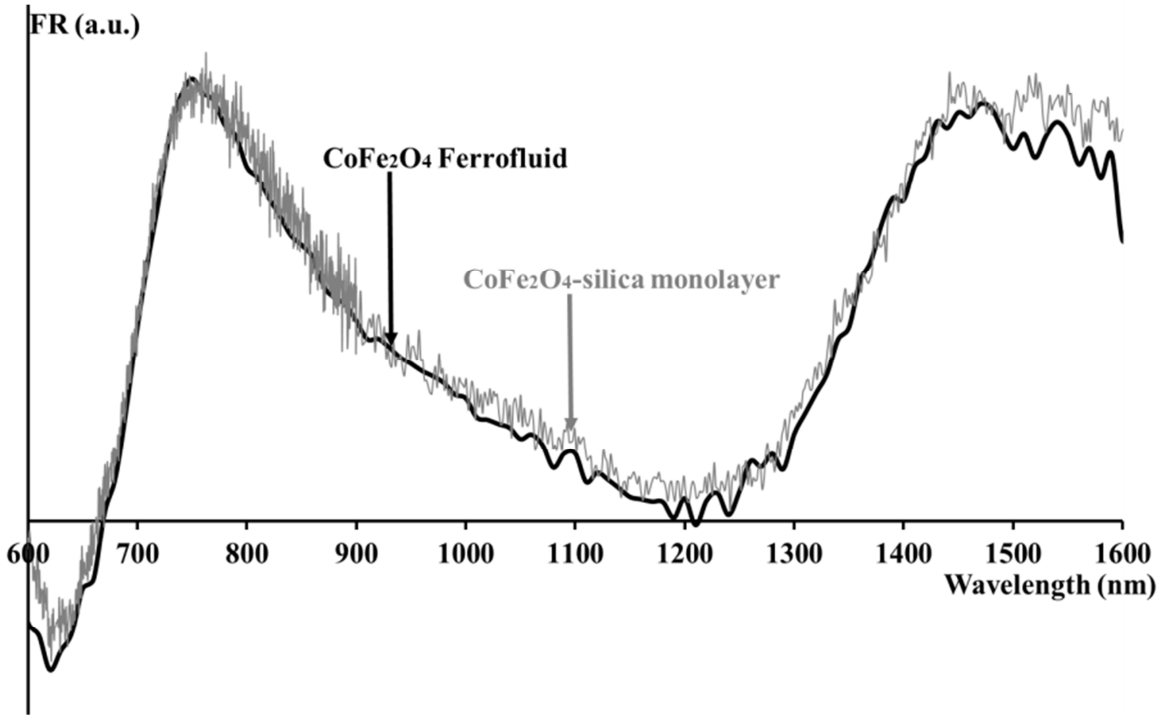

Figure IV-4: Normalized Faraday rotation curves of the $CoFe_2O_4$ doped silica monolayer and the $CoFe_2O_4$ ferrofluid as a function of the wavelength

IV.2. Optical and structural properties of undoped opals

Before the elaboration of the MPC an analysis of the structure of the direct and non-magnetic inverse opals has to be done. In this part, the direct opals and the non-magnetic inverse opals structure is characterized by Spectral Polarimeter and SEM equipements. ***Figure IV-4*** has indicated that the magnetic nanoparticles possess two Faraday rotation peaks, one at ~750 nm and the other at 1400-1600 nm. The further studies should be concentrated

about these waveranges. This means that the position of the PBGs has to take place in these areas. Using the Bragg law (Eq. I.8) applied for inverse opals, which consist of air (74 %) and silica (26 %) as a fcc periodic organization, the PBG was positionned in these two areas. Thus, the diameter size of the innitial PS was chosen as 400, 450, 800 and 900 nm.

IV.2.1. Direct opals

First of all the structural analysis of the created direct opals was made, because they provide the basic template of the inverse opal fcc arrangement. The realization of the perfect face-centered-cubic organization of the template is a key element of this project. As detailed in the previous chapter the direct opals are realized by a sedimentation self-assembly method as illustrated on ***Figure IV-5***.

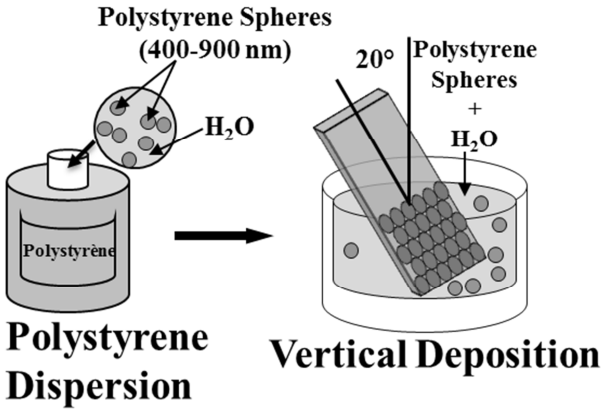

Figure IV-5: Direct opal elaboration schema

IV.2.1.1. PBG position

Based on the diameter sizes mentioned above, and assuming a perfect fcc arrangement the center position of the photonic band gap can be calculated with the Bragg low (Eq I.8). According to the provider of the spheres, the refractive index of the polystyrene is 1.59 at 589 nm. ***Table IV-2*** presents these values for the first and the second harmonic PBGs. Such a calculation show that depending on the diameter and the harmonic, the band gap position can vary from 476 to 2152 nm. However the wavelength range of the spectral polarimeter is [400-1600 nm]. It is thus clear that the measurements will not allow to evidence all of this band gap.

d_{sph} of the used polystyrene spheres (nm)	400±9	453±9	799±9	903±12
1. harmonic calculated PBG of the direct opals (nm)	953	1079	1904	2152
2. harmonic of the calculated PBG of the direct opals (nm)	476	539	952	1076

Table IV-2: Calculated position of the PBG for the four different sizes of polystyrene spheres. (Eq I.8). Assuming that the arrangement possesses the fcc structure, the Bragg law is used with a polystyrene refractive index of n_{PS}=1.59

3D MPC templates were realized by vertical deposition with a substrate inclination of 20 ° with the respect of vertical, using 0.2 % volume fraction of polystyrene in aqueous dispersion (***Figure IV-5***). The samples were dried as it was explained on ***Table III-5***. ***Figure IV-6*** illustrates the transmittance curves of the four different sizes of direct opals. For a nicer visibility, the four graphs were shifted on Y axes in the increasing order of the diameter size of the spheres. In the case of the two biggest diameters of the spheres the first harmonic cannot be observed on these curves. Otherwise, the PBG peaks are not far from the prediction, but both are a bit higher.

Figure IV-7 shows the PBG center positions of the direct opals as a function of the diameter size of the polystyrene spheres in the case of the second harmonic band gap. The measured values should obey to the Bragg equation (Eq I.8), which gives that the central wavelength is proportional to the diameter of the spheres. The perfect correlation between the experimental points and the linear fit shows that the measurements are in good agreement with this law.

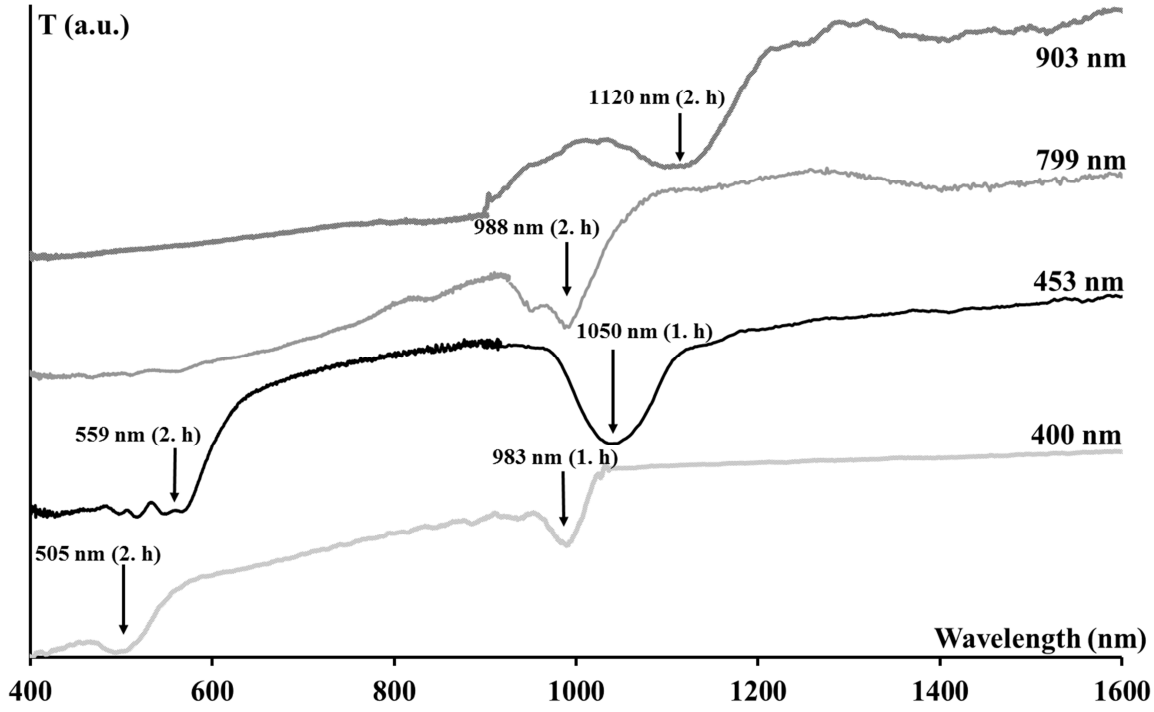

Figure IV-6: Transmittance curves of the direct opal templates as a function of the wavelength. The polystyrene diameter is given and the band gap is identified

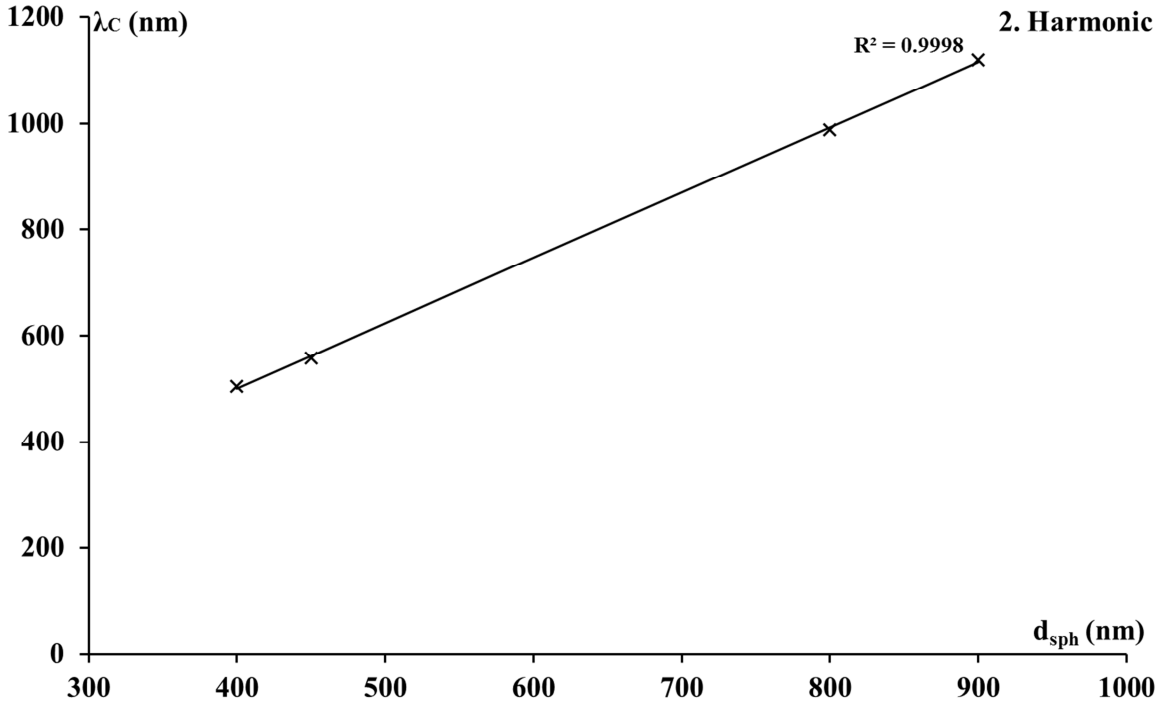

Figure IV-7: Measured positions of the PBGs of the four polystyrene templates as a function of the diameter size of the spheres

Because the resulted positions of the PBG peaks are a bit higher than the predicted values, a specific analysis of the structure analysis has to be made.

IV.2.1.2. Study of the structure

During the direct opal elaboration, disorganizations and cracks can appear in the template structure. To verify optically the quality of the direct opal templates, transmittance n measurements were made varying the incident angle of the light beam. In this way, the real value of the d_i interplanar spacing and n_{Eff} complex effective index of the prepared sample can be determinated using the Snell law modified Eq II.4, which takes into account the angle of refraction measured from the normal.

The resulted equation is given as it was explained in the 3rd chapter:

$$\lambda_C = 2d_i\sqrt{n_{Eff}^2 - sin^2\theta} \qquad \text{Eq IV.1}$$

If we consider 0 ° incident angle when the beam is perpendicular to the sample, the transmittance spectrums were registered from 0 ° to 42 ° with 6 ° different steps. The used diameter size of the PS was 453 nm, with the polystyrene volume fraction of 0.2 %, and the vertical deposition was executed at 45 °C.

Figure IV-8 shows the direct opal transmittance curves with the increasing incident angle of the light beam. Each graph was normalized for a better visualization of the tuning PBG position. The forbidden band was found at 1050 nm then with the growing angle the PBG position was blue shifted as it is expected from equation Eq I.8.

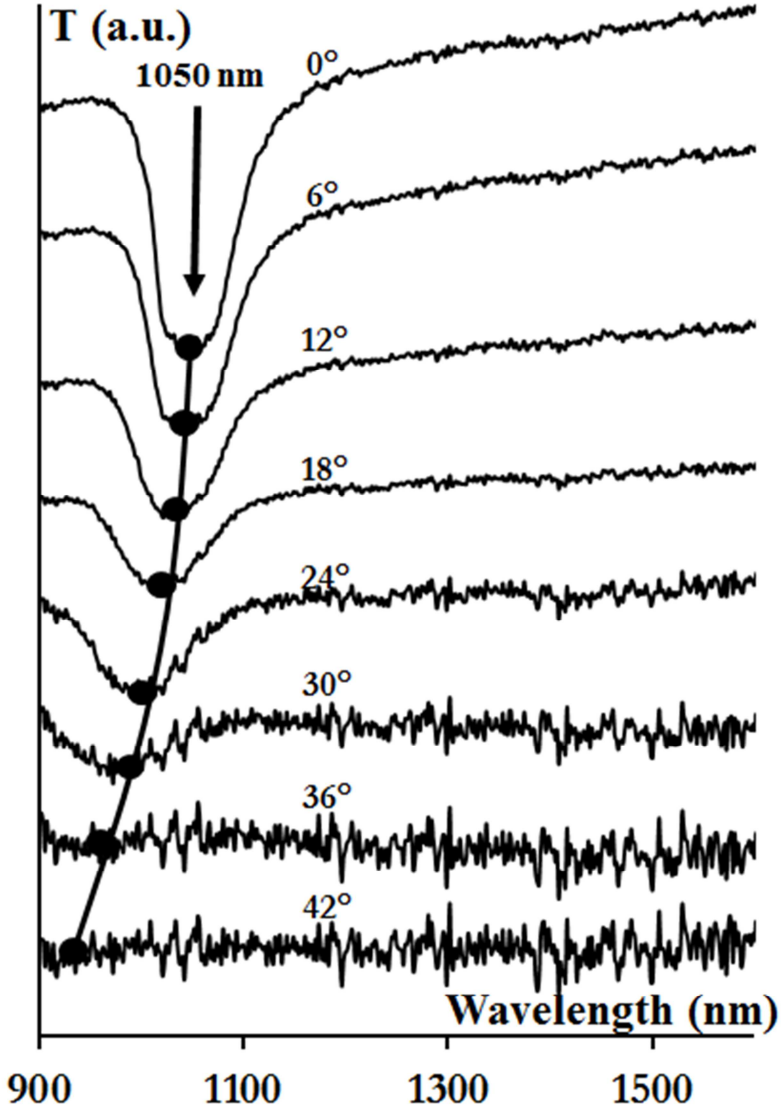

Figure IV-8: Transmittance of the direct opal as a function of the incident angle. The diameter of the polystyrene sphere is 453 nm and a focus is made on the first harmonic

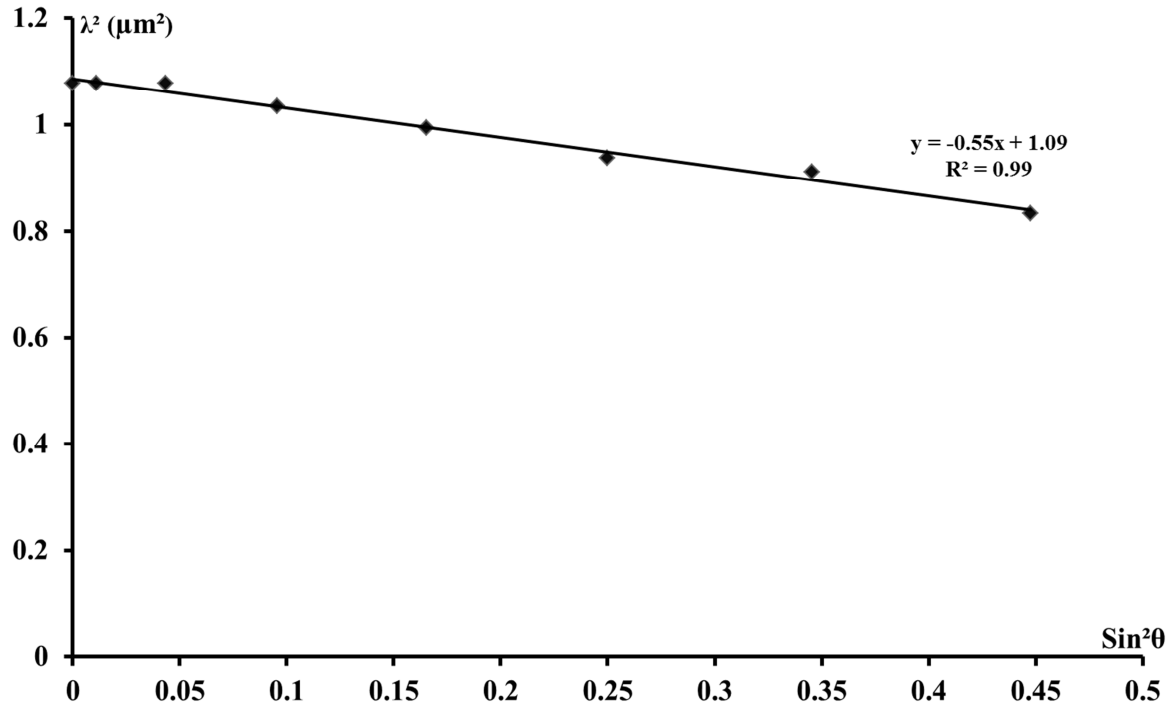

Figure IV-9: Center position of the first harmonic PBG on square plotted as a function of the sin²θ angle rotation

To get the real value of n_{Eff} and d_i of the elaborated direct opals the measured center of the bang gap has been plotted through its square value as a function of the sin²θ incident angle (***Figure IV-9***). From the slope of the fitted line the d_i interplanar distance can be determinated like:

$$slope = -(2d_i)^2 \qquad \text{Eq IV.2}$$

The average center to center distance between the spheres can be calculated like:

$$D = \frac{d_i}{0{,}8165} \qquad \text{Eq IV.3}$$

The effective refractive index can be defined knowing d_i like:

$$y - axis\ intercept = (2d_i)^2 n_{Eff}^2 \qquad \text{Eq IV.4}$$

From the linear fit of ***Figure IV-9***, the interplanar distance is calculated at a value of d_i = 370 nm. Thus, the average center to center position is D = 454 nm, which is exactly the diameter size of the used polystyrene spheres (d_{sph} = 453 nm ±9 nm). The Effective refractive index is then determined to be n_{Eff} =1.41. From the effective medium theory, such an effective index is expressed as:

$$n_{Eff} = \sqrt{f_{sph} \cdot n_{sph}^2 + \left(1 - f_{sph}\right) \cdot n_v^2} \qquad \text{Eq IV.5}$$

The value of 1.41 for the effective index leads to a value of 1.53 for the refractive index of the polystyrene. One should remind that the sample with 453 nm sphere diameter size produces a first harmonic PBG about 1050 nm. Given at 1.59 for 589 nm by the provider, it seems relevant that for higher wavelength the refractive index of the polystyrene decrease.

This first study and the good correlation obtained on the two previous figure evidence the fcc arrangement of our templates.

IV.2.1.3. SEM images

The visualization of the direct opal was made by Scanning Electron Microscope. The ***Figure IV-10*** and ***Figure IV-11*** show the 3D fcc arrangement of one polystyrene opal, made by vertical deposition procedure. The Diameter size of the polystyrenes is 453 nm. The polystyrene liquid concentration was 0.1 %. The magnification is x10000 and x50000 for ***Figure IV-10*** and ***Figure IV-11***, respectively. The electron microscope pictures can give information about the disorganizations and cracks of the structure. These images prove that the vertical deposition with the inclination of 20 ° can produce well-organized fcc structure in the area of 25 µm².

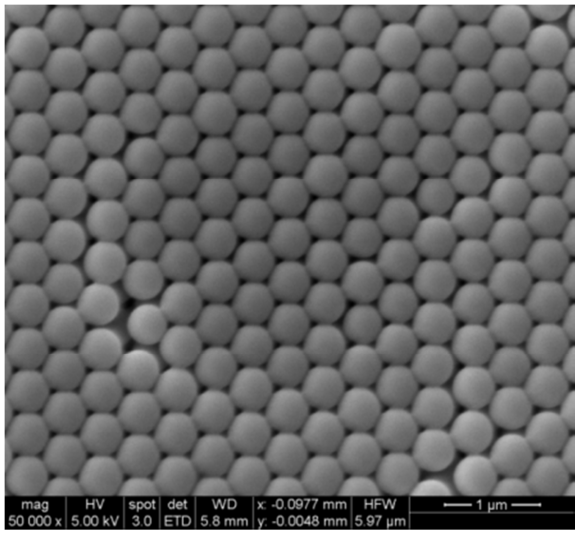

Figure IV-10: SEM image of 453 nm direct opal structure with the magnification of x10000 (incident liquid PS volume fraction=0.1%)

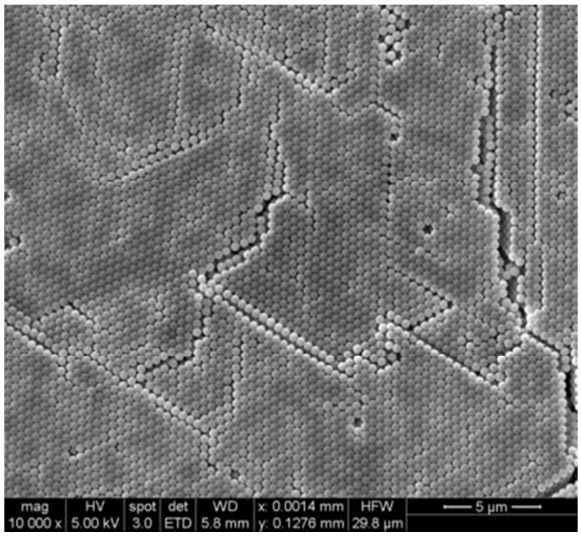

Figure IV-11: SEM image of 453 direct opal structure with the magnification of x50000 (incident liquid PS volume fraction=0.1%)

IV.2.2. Inverse opals

After the realization of the Fcc direct opal templates with four different sphere diameter sizes, the second step of the creation of 3D MPC was the elaboration of three dimensional non-magnetic inverse opal. This is very important to verify the Fcc arrangement and the optical effect of the opal. The next part gives the results of the non-magnetic inverse opal characterization made by Spectral Polarimeter and Scanning Electron Microscope.

IV.2.2.1. PBG position

Non-magnetic inverse opal was made by impregnation of direct opal, as it was explained in the 2nd chapter and recalled on figure (***Figure IV-12***).The direct opal structure has to sustain the impregnation without breakage, when the TEOS solution is entering between the polystyrene balls. Then this impregnated three dimensional opal is gelified through hydrolysis and drying process at 90 °C. Finally, the polystyrene template has to be eliminated by ethyl-acetate leading to the formation of a silica inverse opal.

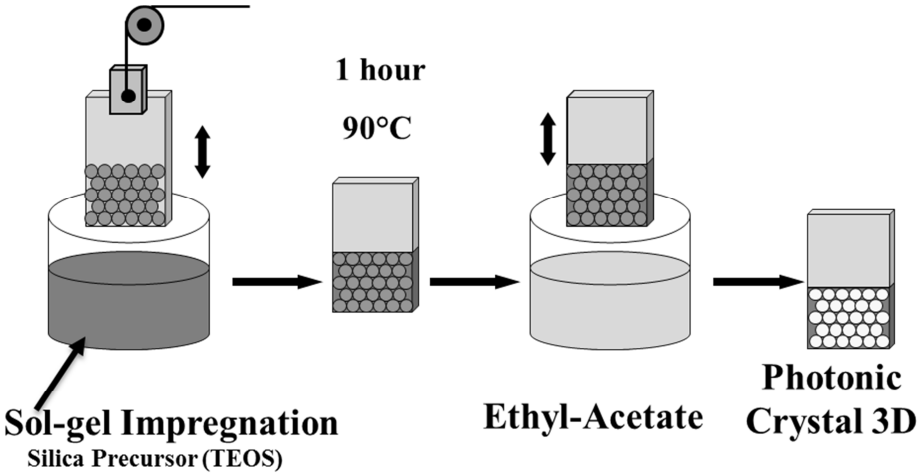

Figure IV-12: Inverse opal elaboration using direct opal

On ***Figure IV-13*** the transmittance curves are presented for the direct and inverse opal made with 453 nm diameter size of polystyrene spheres as a function of the wavelength. The positions of the photonic band gaps are at 1030 and 760 nm, respectively. ***Figure IV-13*** gives an optical prove that the three dimensional fcc structure has not fractured during the inversion process, because the sample always possesses the PBG in the transmittance spectrum.

Between the direct and inverse opals the PBG positions has about 270 nm difference. This phenomenon is due to two changes. As it is explained in the work of Waterhouse et al. [66], the PBG shift is mainly caused by the filling factor (FF) change, because in the direct opal 26 % of the volume is occupied by air whereas it is 74 % in the inverse opal. Thus, the effective index value which governs the Bragg law of the center wavelength is modified by the inversion. The minor second cause is the different refractive index of silica and polystyrene, 1.4 instead of 1.53.

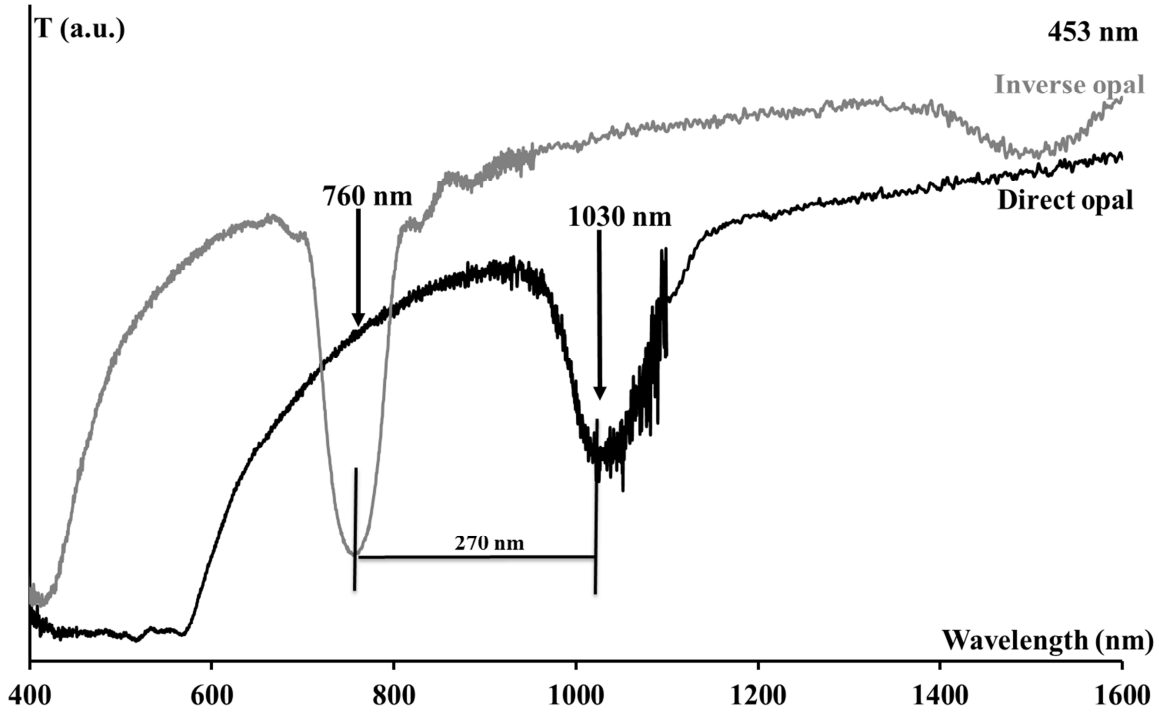

Figure IV-13: Transmittance spectrum of the direct and inverse (the used polystyrene spheres template was 453 nm)

Figure IV-14 represents the measured transmittance spectrum of the four different kind of inverse opals. For each value of initial sphere diameter, one or two photonic band gaps can be observed. For the two smallest diameter sizes, the second harmonic photonic band gap cannot be measured, because it is out of the wavelength range of the spectral polarimeter: below 400 nm. These curves evidence the ability to construct 3D arrangements whatever the size of the spheres.

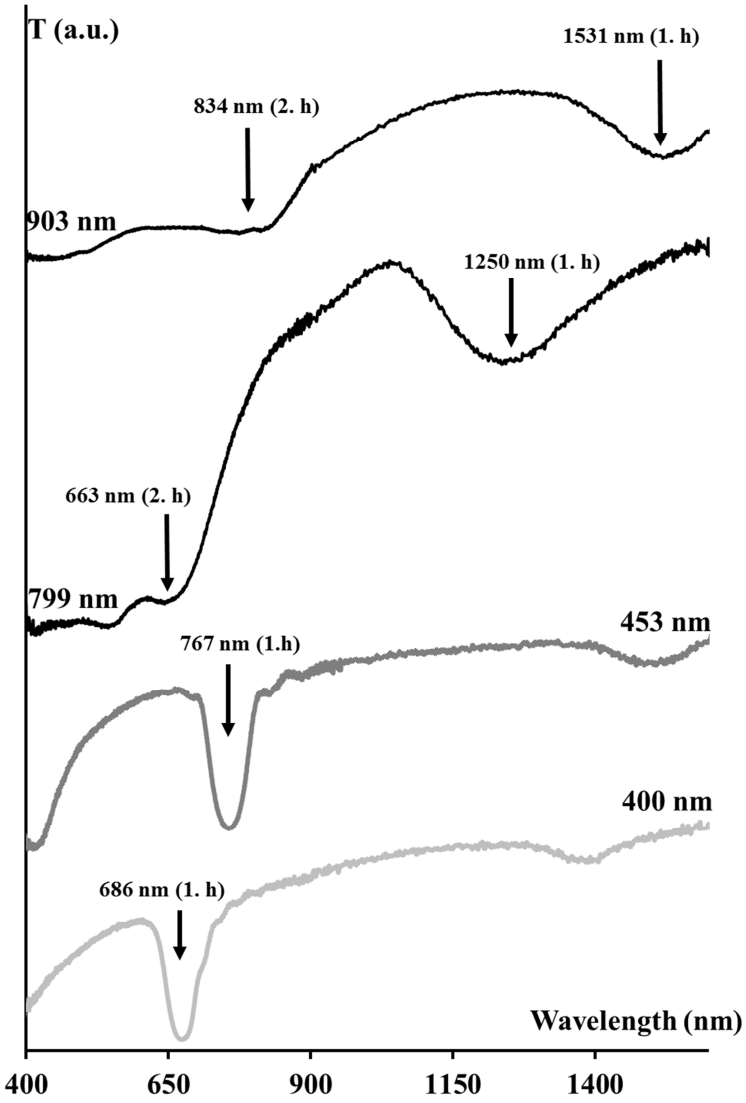

Figure IV-14: The measured transmittance spectrum of the four different size of inverse opals

Figure IV-15 presents the first harmonic λ_C PBG peak position as the function of the used diameter size of the direct opal template. Correspondingly with the Bragg law (Eq I.8), the center position of the forbidden bands tuned to the higher wavelength with the growing diameter size of the used PS template through a proportionnal relation. The correlation reported on ***Figure IV-15*** between the experimental points and a linear fit show that the measured values are in good agreement with the Bragg law.

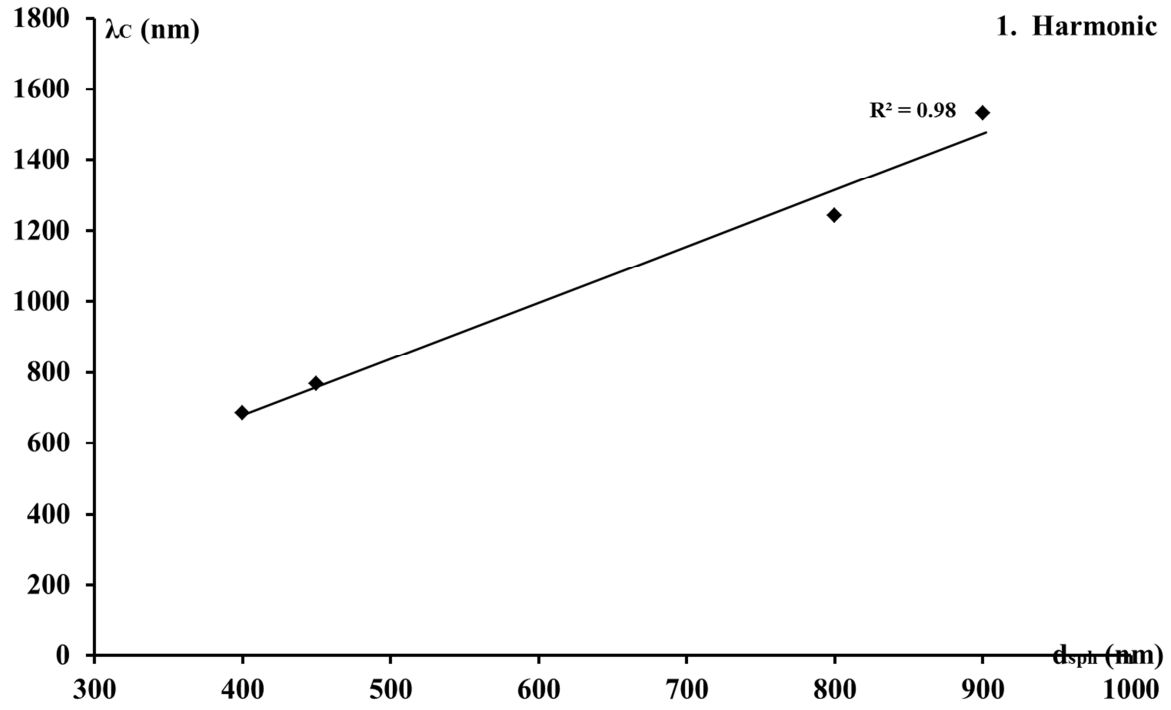

Figure IV-15: 1. harmonic PBG center positions as a function of the used d_{sph} of the direct opal templates

IV.2.2.2. Study of the structure

As in the case of the direct opals, the structure of the non-magnetic inverse opal was analyzed. To do so, transmittance measurements were made varying the incident angle of the light beam from 0° incident angle to 40 ° with 5 ° step differences. ***Figure IV-16*** presents such spectra of a non-magnetic inverse opal made by 799 nm PS template. ***Figure IV-16*** was adjusted by slipping the curves to form continuous wave of the band gap peaks, showed on ***Figure IV-16*** as a black line. The blueshift obeys to the Bragg law, where with growing angles the position of the PBG is tuned to the shorter wavelengths.

To definite the real value of the effective index n_{Eff} and the interplanar distance d_i , the square value of center wavelength of the band gap has been plotted as a function of the $\sin^2\theta$ incident angle (***Figure IV-17***). The 0.97 correlation coefficient obtained on this curve between the experimental points and the linear fitting confirms the good fcc arrangement of our inverse opals.

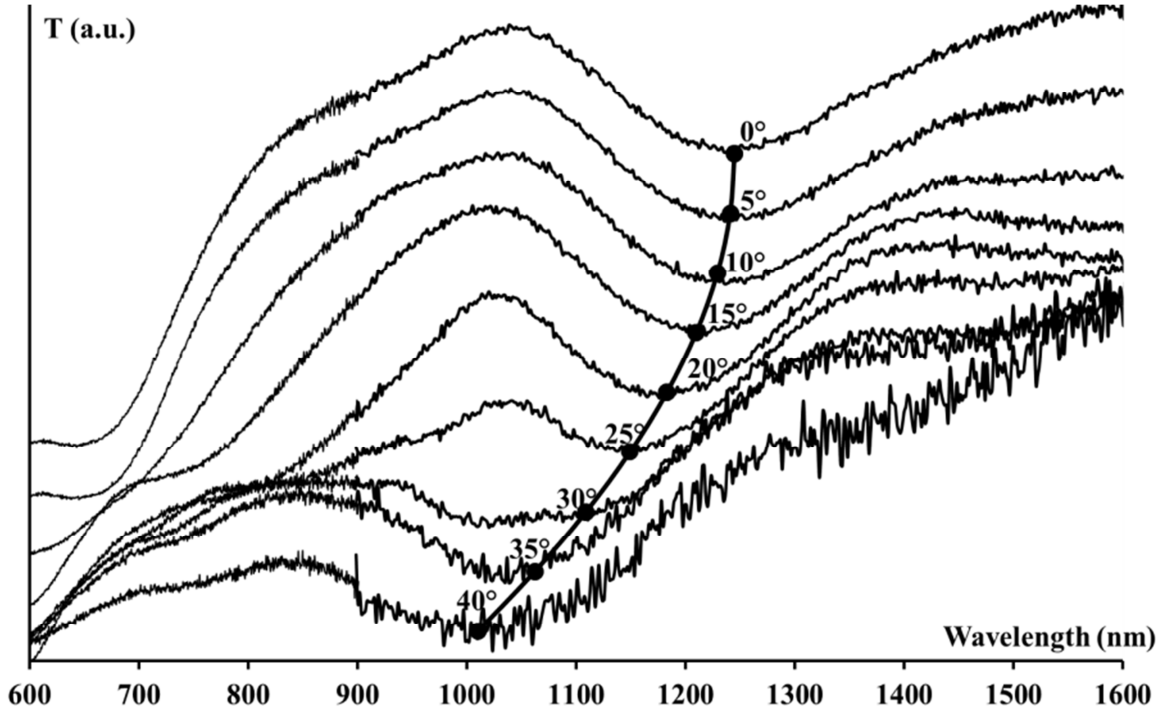

Figure IV-16: Transmittance spectrum with different incident beam angles (0 °-40 °). The inverse opal is made by 800 nm diameter size of PS template

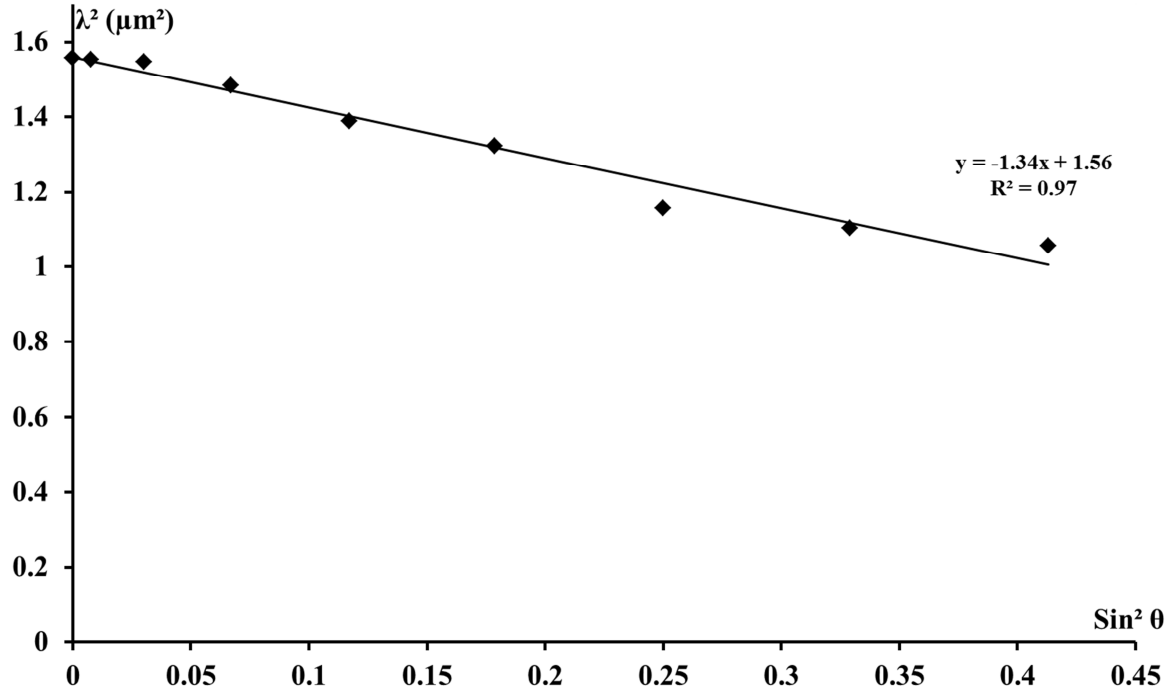

Figure IV-17: Square value of the center position of the first harmonic PBG plotted as a function of the sin²θ of the incident angle. The inverse opal was made with 799 nm d_{sph} template

As it was explained above d_i and n_{Eff} van de deduced from the linear fitting of the experimental points. In this way, the measured non-magnetic inverse opal has interplanar distance (d_i) value of 578 nm. The average center to center distance between the spheres (D) is 708 nm. This value is 100 nm smaller than the used sphere diameter size of the template opal, which is 800 nm. Such a phenomenon was explained in the work of Nishijima at al. [7]. They proposed that this difference is probably due to the shrinkage of the silica matrix during the drying process.

The n_{Eff} is resulted as 1.08. Using the effective index relation, Eq III.1 the refractive index of the silica has been determinated as 1.28. The predicted value of a silica matrix is about 1.44 [92,93], so we have obtained here a lower value. That may be due to the porosity of the silica matrix inside the opal.

IV.2.2.3. SEM images

Figure IV-18 and ***Figure IV-19*** show the electron microscope images of a 3D inverse opal. For the realization of this sample 903 nm d_{sph} template opal was used. For the elaboration of the direct opal Polystyrene dispersion of 0.2 % PS volume fraction was used. These pictures evidenced that an area of about 400 µm² the arrangement maintains a well-organized periodic fcc structure.

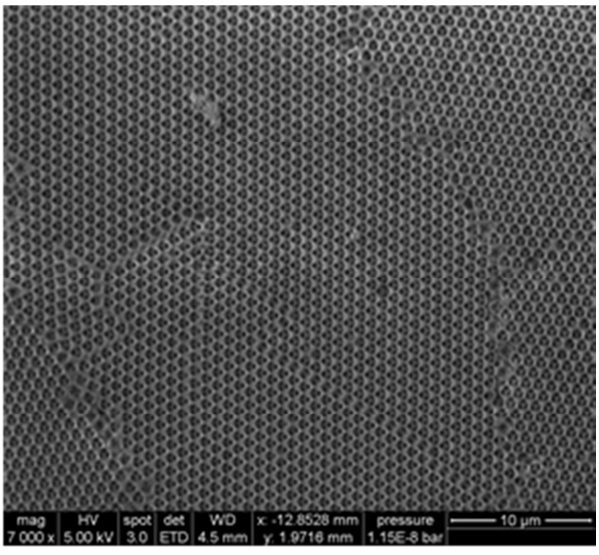

Figure IV-18: SEM image of non-magnetic inverse opal made by 903 nm direct opal with x7000 magnification

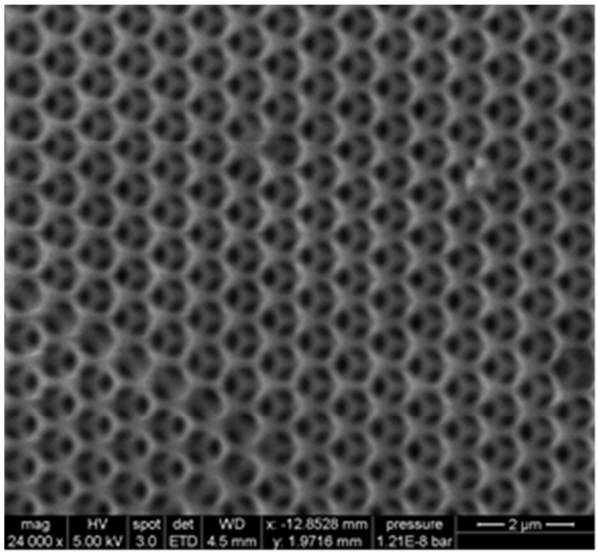

Figure IV-19: SEM image of silica inverse opal made by 903 direct opal with x24 000 magnification

IV.3. Magneto-optical inverse opals

In this part, the optical, physical and structural properties of doped inverse opals will be presented as in the prevois cases for direct and undoped. But it will be completed by the main results concerning the magneto-optical study of these elements.

For the elaboration of the doped inverse opals, the four different sizes of the templates were used in order to obtained PBGs at the two waverange where the cobalt-ferrite has large Faraday rotation (~ 750 nm and ~ 1500 nm).

The important step of the realization of the magnetic inverse opals is to dope the sol-gel solution with the magnetic nanoparticles ($CoFe_2O_4$) before the impregnation of the direct opal. The full protocol is detailed in the previous chapter.

IV.3.1. PBG position

On ***Figure IV-20*** are reported the transmittance curve of a direct opal, an undoped inverse opal and a doped inverse opal, in the case of a polystyrene template of 453 nm. This figure shows the photonic band gap tuning from 754 nm for the undoped to 777 nm for the doped inverse opal. This 23 nm shift can be attributed to the refractive index difference between a pure silica matrix and the doped one. Indeed, in the first section of this chapter, we have shown that the doping contributes to an increase of this index.

Figure IV-20 also presents the PBG of the polystyrene direct opal, which takes place at higher wavelength than the two inverse ones with distances of 232 and 259 nm. Furthermore, the PBG of the doped sample is remaining, so the structure should have fcc organization.

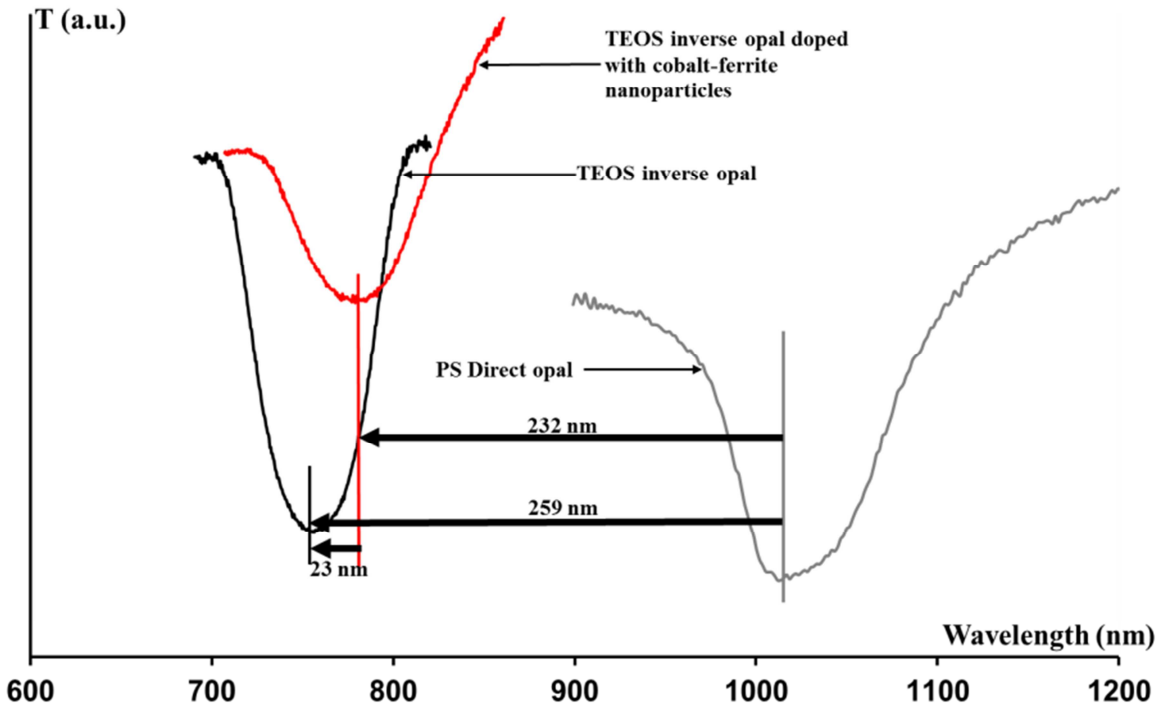

Figure IV-20: BPG position difference between the direct, the doped and the non-doped inverse opals (d_{sph} of the used template was 453 nm)

Figure IV-21 shows the transmittance measurements made on a non-magnetic inverse opal, a magnetic inverse opal and a classical magnetic monolayer (2:2). The spectral behavior of the doped opal appears as a product of the two other curves. Indeed, cobalt ferrite nanoparticles have a major range of absorption under 900 nm which results as a linear slope on the curve of the monolayer between 400 and 900 nm. The transmittance of the undoped opals remains at a quite constant value excepted in the area of the band-gap. The doped opal combines these two effects through a linear envelope between 400 and 800nm and a band gap about 780 nm. This ***Figure IV-21*** proves the possibility to achieve 3D doped inverse opals.

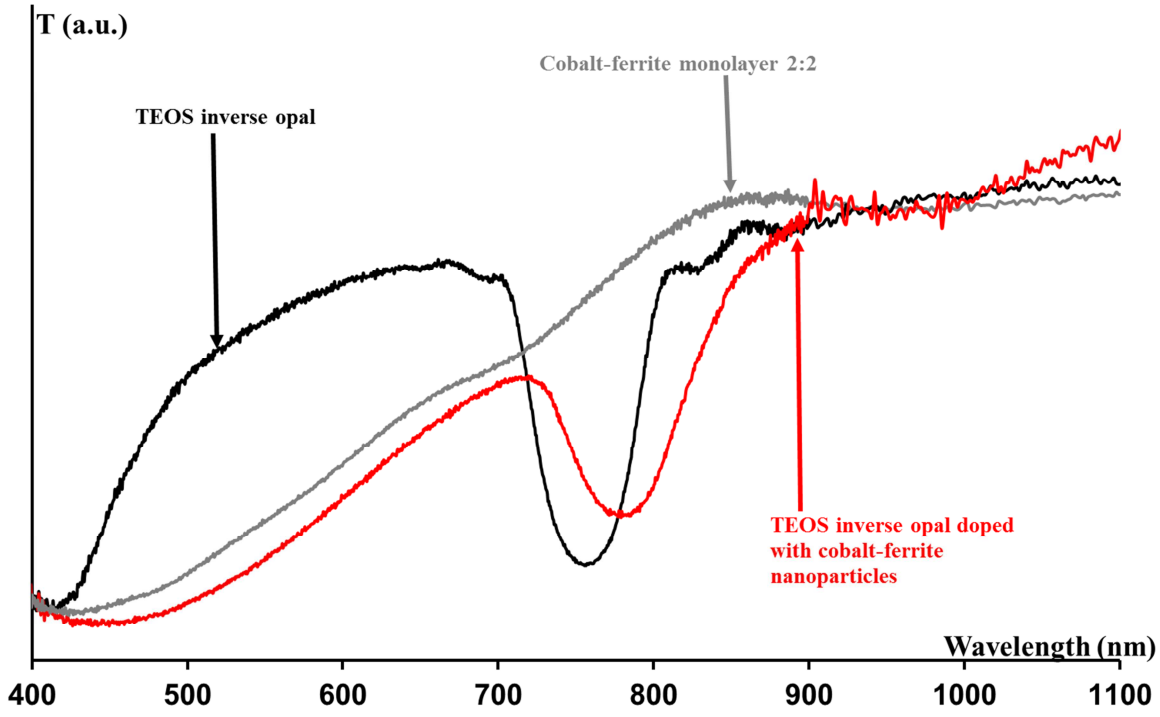

Figure IV-21: Transmittance measurement of the $CoFe_2O_4$ monolayer (2:2 incident liquid VF), non-magnetic and magnetic inverse opal as a function of the wavelength (453 nm d_{sph} size of used template)

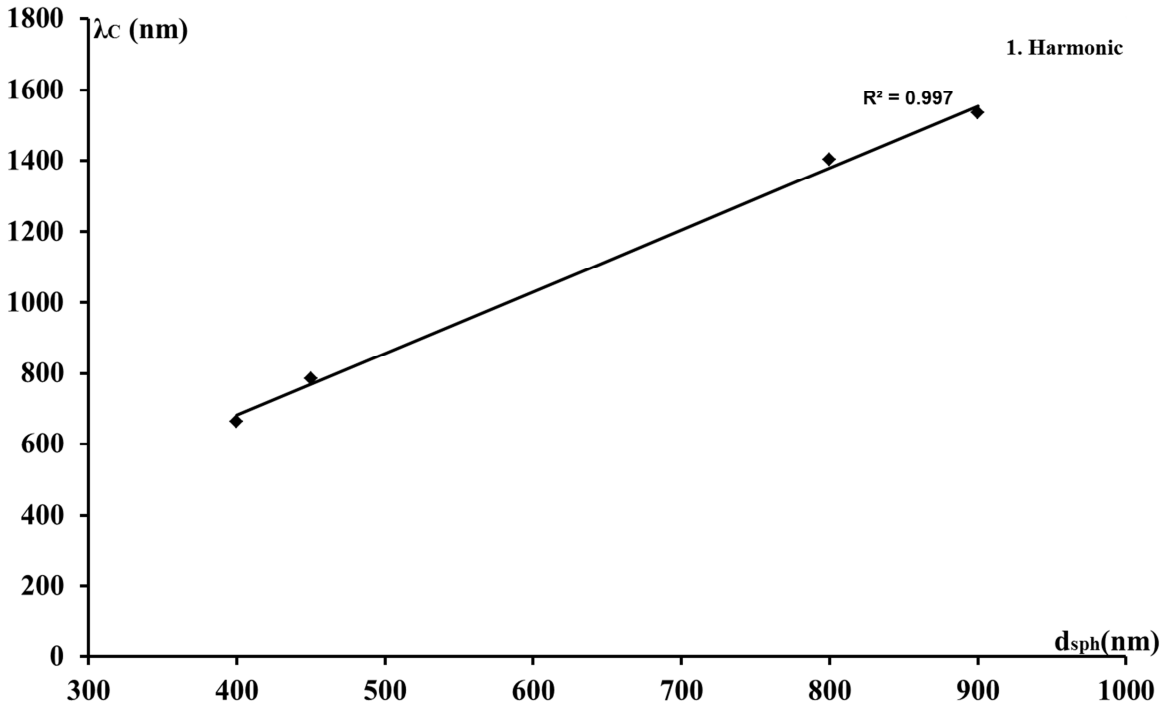

Figure IV-22: λ_C plotted as a function of the sphere diameter size of the used template, in the case of doped inverse opals

Figure IV-22 shows the center position of the PBGs of the doped inverse opals as a function of the size of the direct opal template. λ_C increases with growing d_{sph} size, which means that the realized samples follows the behavior of the Bragg equation (Eq I.8).

IV.3.2. Study of the structure

As in the case of direct and non-magnetic inverse opals, the interplanar distance d_i and effective index n_{Eff} can be calculated from the transmittance spectra measured at different incident angles. The result is reported on ***Figure IV-23*** through a square plot of the central wavelength. The sample was made by a 903 nm direct opal template The resulted d_i interplanar distance and average center to center distance between the spheres are 653 nm and 800 nm, respectively. Between the d_{sph} of the used template and the resulted center to center average distance there is 100 nm shrinkage. It is exactly the same result as in the case of non-magnetic inverse opals.

The n_{Eff} effective refractive index deduced from the ***Figure IV-23*** is 1.13. Using Eq III.1, the real value of the doped silica matrix inside the inverse opal can be calculated assuming fcc structure. It is equal to 1.43 with a measurement made about 1500 nm. This value is lower than the one deduced from the refractive index curve of the monolayer in the case of the 2:5 ratio: ~1.6 measured at 1100 nm. The same kind of difference has been observed for the undoped samples and may be attributed to the porosity of the matrix.

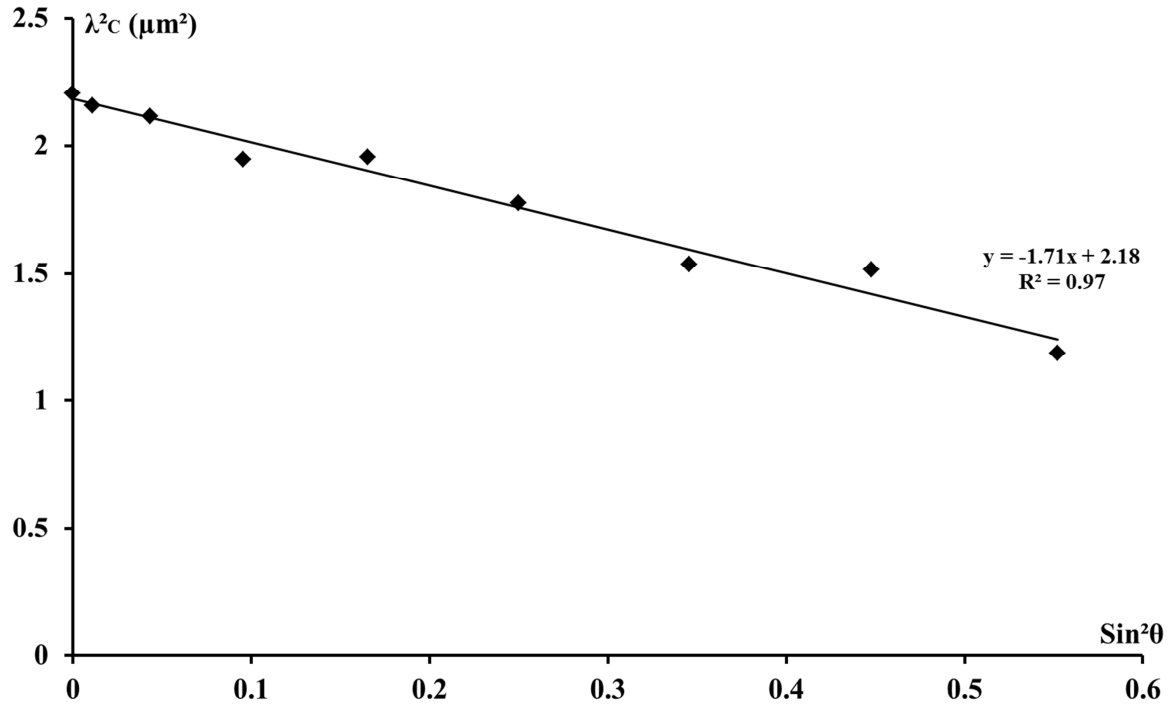

Figure IV-23: λ^2_C graph of a doped inverse opal made by 903 nm template as a function of the $\sin^2\theta$ of the incident angle

IV.3.3. SEM images

The Scanning Electron Microscope images reported on ***Figure IV-24*** and ***Figure IV-25*** are related to doped inverse opals made with 799 and 903 nm diameter sphere size templates. The magnifications were x30000 for both SEM images. ***Figure IV-24*** evidences the organization inside the three dimensional structure due to the presence of one crack. It can be seen that the structure contains 8 layers, and in this way we can evaluate the thickness of the crystal. Here, based on the value of the diameter of the initial spheres (799 nm) and taking into account the shrinkage the thickness is about 5.6 µm. Of course, this is a local determination of such a thickness whose homogeneity is certainly not very large. From ***Figure IV-25***, the fcc structure without disorganization can cover a 81 µm² area. This image proves that the fcc structure was maintained during the whole elaboration procedure.

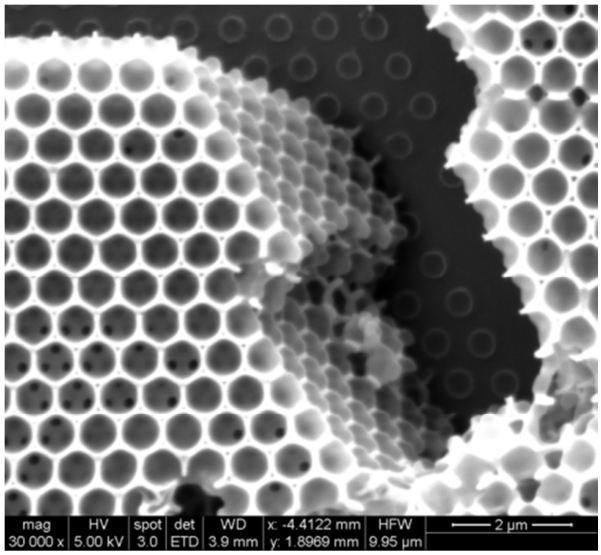

Figure IV-24: SEM image of 799 nm cobalt-ferrite-TEOS inverse opal (x30000 magnifications)

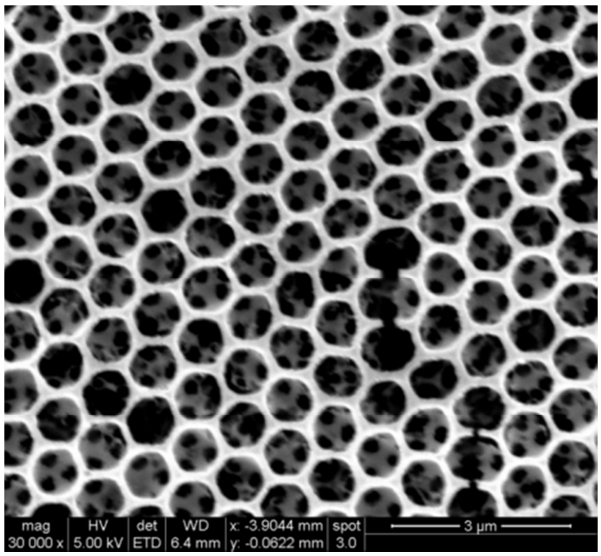

Figure IV-25: SEM image of 903 nm doped inverse opal (x30000 magnifications)

IV.3.4. Faraday rotation enhancement

Spectral Faraday rotation measurements were made with the spectral polarimeter in order to check the ability of the doped inverse opals to behave as magneto-photonic crystals. The wavelength range is 400-1600 nm. In order to clearly evidence the effect of the 3D arrangement on the magneto-optical effects, the FR curves of 3D opals are always plotted on the same graph than that of a classical monolayer. Of course, the vertical scale has to be adapted to arbitrary units. The reference monolayer has FR peaks about 750 nm and 1400-

1600 nm (***Figure IV-4***). Furthermore, the transmittance curve of the opals is also plotted on the same graph to identify the spectral position of the photonic band gap.

a) Magneto-photonic behaviour

Figure IV-26 is related to a doped inverse opal made using a 453 nm template. The comparison of the Faraday rotation spectrum of the opal (red curve) with that of the monolayer (gray curve) evidences a behavior that is completely different in the area of the band-gap which is centered at 780 nm. Outside this band, the two FR spectra can be superimposed, but inside the PBG a resonant effect is observed. On the lower edge of the BPG, the Faraday rotation is negatively enhanced to reach a minimum value at 750 nm. On the upper edge, it is positively enhanced to reach a maximum value at 810 nm. Thus, the Faraday rotation is enhanced on the two edges of the photonic band gap with maximum values which have opposite sign and a symmetrical spectral position about the center of the gap.

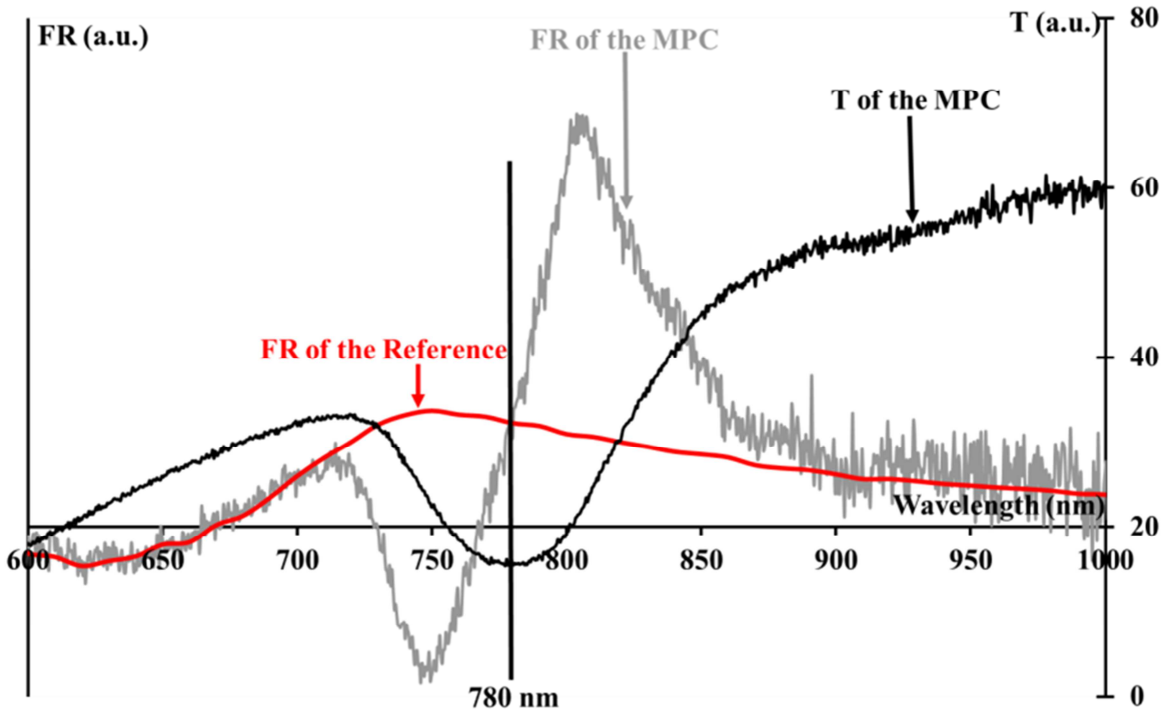

Figure IV-26: Transmittance and Faraday rotation spectra of a doped inverse opal based on a 453 nm template, and Faraday rotation spectrum of a cobalt-ferrite monolayer as a reference

Such an enhancement at the edges of the PBG of a 3D doped opal is quite similar to what has been obtained by the calculations on a 1D periodic structure in the second chapter. It is the signature of a magneto-photonic behavior due to the 3D periodic arrangement. Thus our silica inverse opals doped by magnetic nanoparticles have the potentiality to enhance the Faraday rotation compared to a classical monolayer of the same matrix.

To fulfill this study, the magneto-optical enhancement has been studied varying the size of the air spheres.

b) Influence of the size of the air spheres

On ***Figure IV-27***, ***Figure IV-28*** and ***Figure IV-29*** are reported the same curves than above but with air spheres size of 400, 903 and 799 nm, respectively. In the case of this last size, the curve is given for the second harmonic band-gap. Indeed, the first occurs about 1200 nm, in an area with a very low magneto-optical activity of the cobalt ferrite nanoparticles. So, no significant effect has been measured.

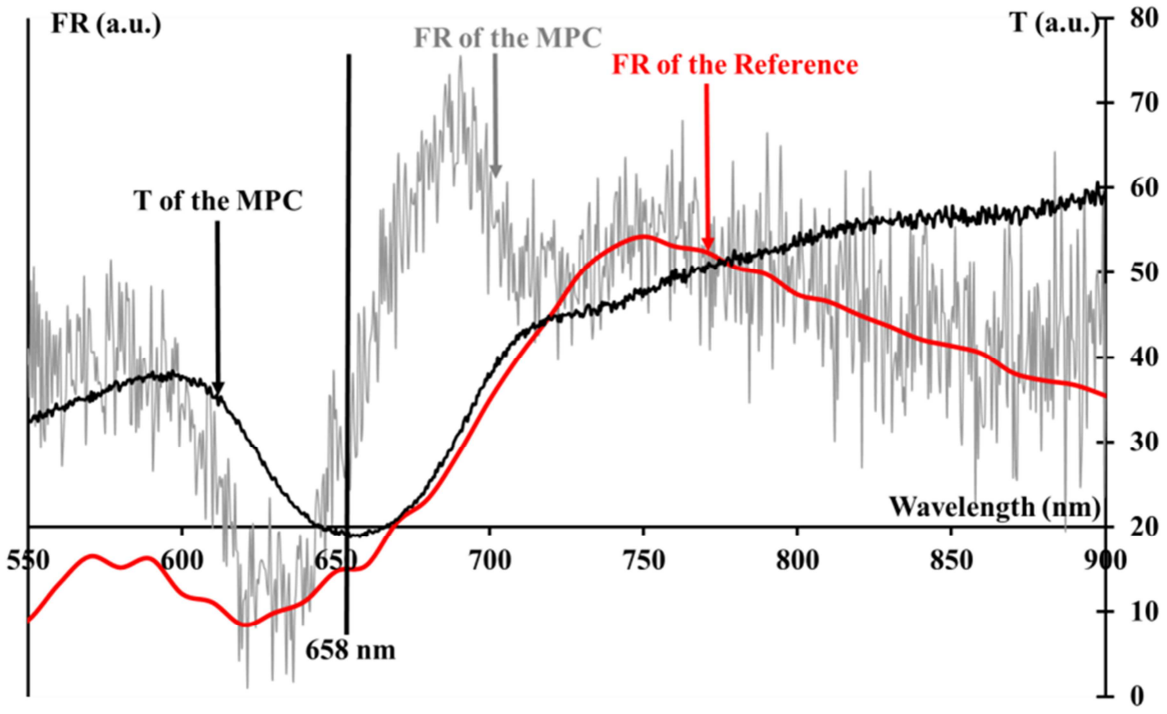

Figure IV-27: Transmittance and Faraday rotation spectra of a doped inverse opal based on a 400 nm template, and Faraday rotation spectrum of a cobalt-ferrite monolayer as a reference

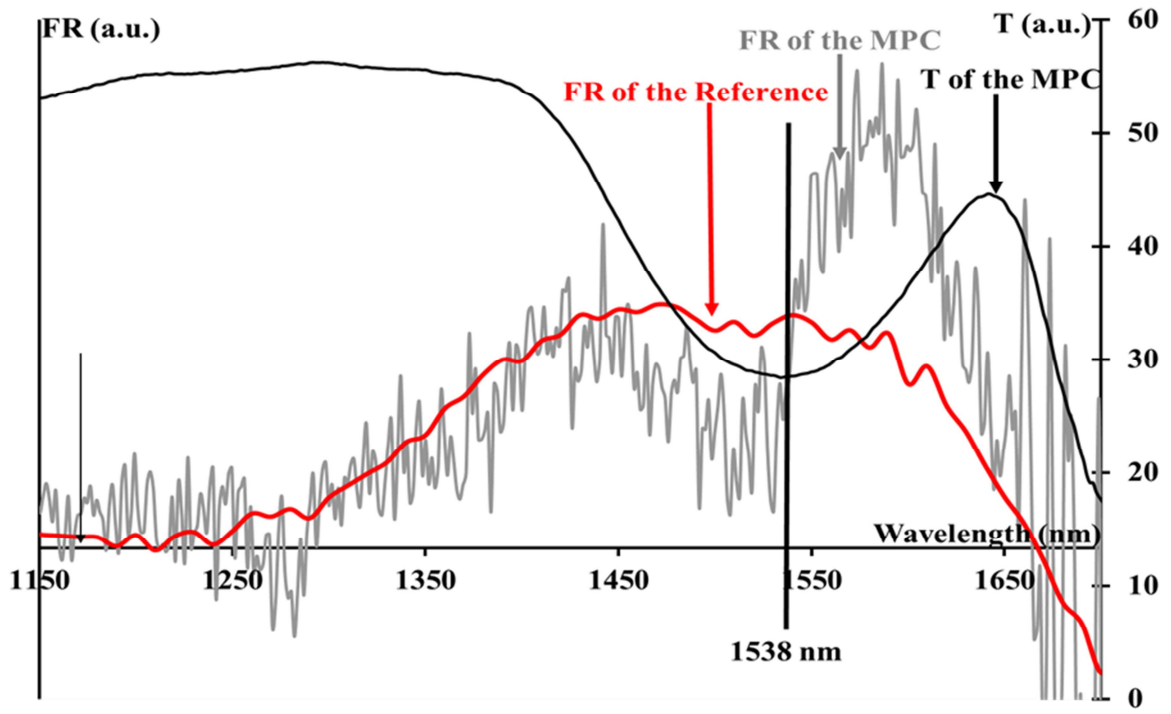

Figure IV-28: Transmittance and Faraday rotation spectra of a doped inverse opal based on a 903 nm template, and Faraday rotation spectrum of a cobalt-ferrite monolayer as a reference

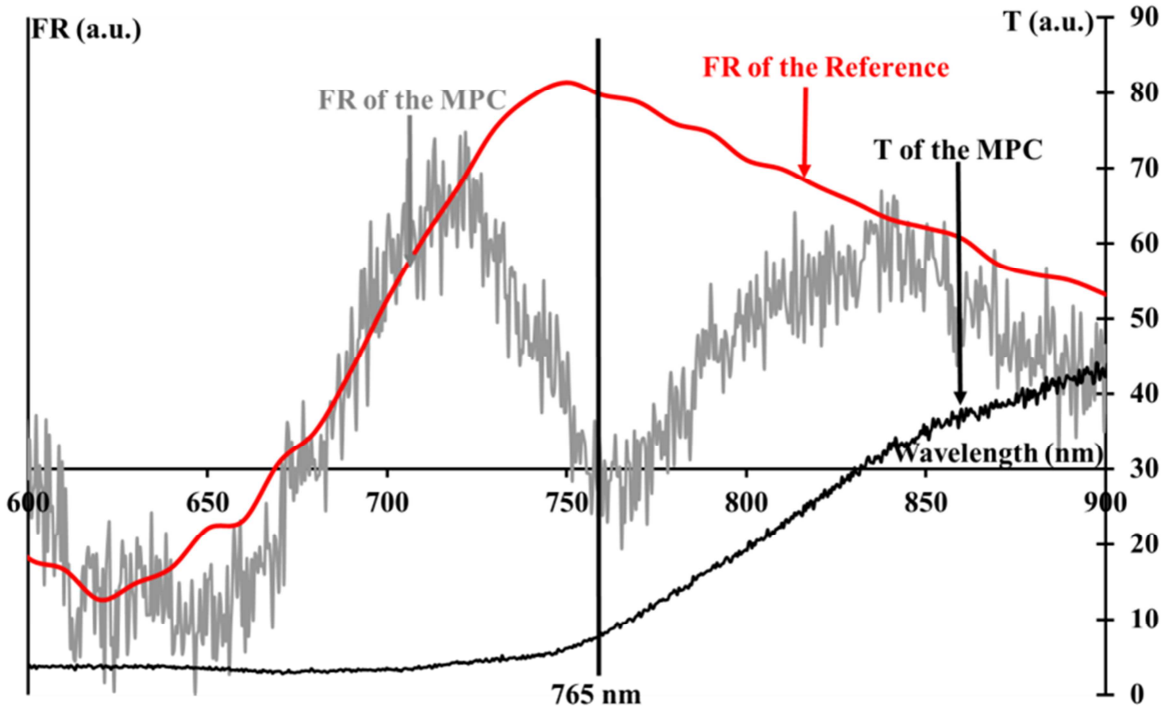

Figure IV-29: Transmittance and Faraday rotation spectra of a doped inverse opal based on a 799 nm template, and Faraday rotation spectrum of a cobalt-ferrite monolayer as a reference. The curves are related to the second harmonic band gap

These three curves show the same kind of behavior for the Faraday rotation of the doped inverse opals. Compared to the reference, it is always different in the area of the PBG. Of course the curves also depend on that of the reference which is not constant in the full wavelength range.

It is interesting to note that, with the 900 nm air spheres, the enhancement is evidenced at a wavelength value about 1500 nm, which is the telecommunications area.

c) Harmonic influence

Figure IV-30 shows the full range Faraday rotation spectra of an inverse opal based on a 900 nm direct template. The comparison with the reference underlines that the magneto-optical behavior is modified in the area of the first and second harmonic band gap: 1535 and 835 nm.

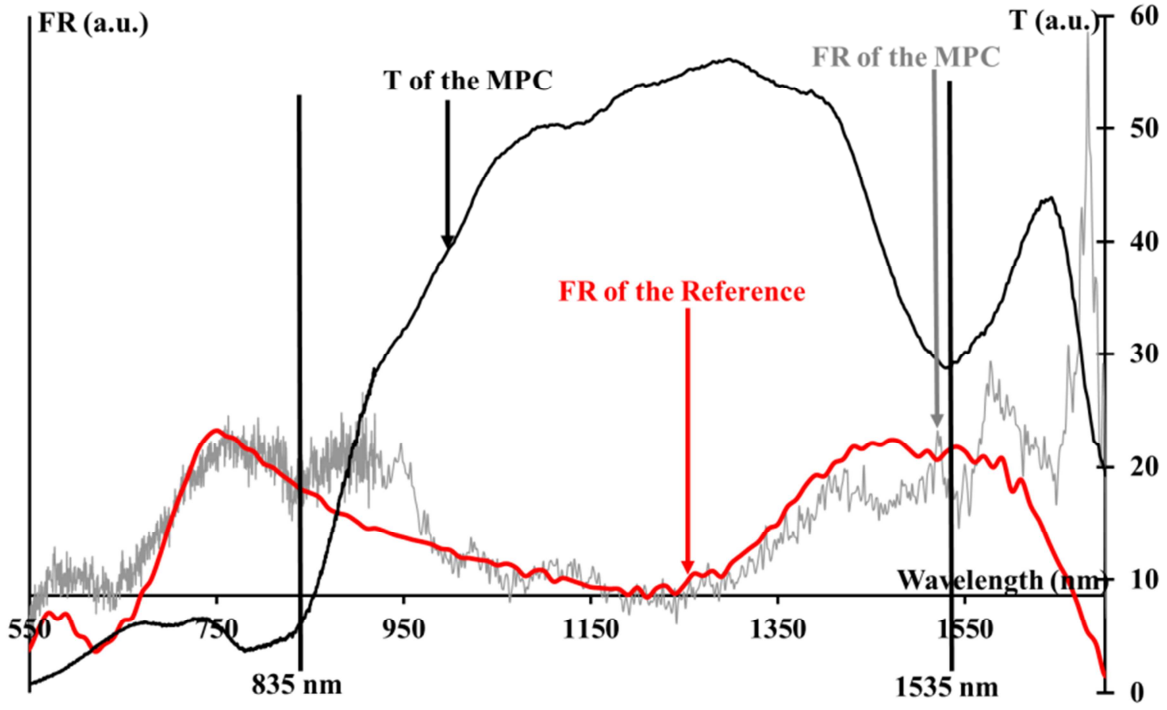

Figure IV-30: Full Transmittance and Faraday rotation spectra of a doped inverse opal based on a 903 nm template, and Faraday rotation spectrum of a cobalt-ferrite monolayer as a reference. First and second harmonic PBGs are shown.

At this stage, we can assume that the magnetic inverse opals realized with our composite matrix behave as magneto-photonic crystals. The same kind of behavior has been evidenced by Caicedo *et al.*[48] with Al_2O_3 inverse opals impregnated by Ni nanoparticles. But

the enhancement demonstrated by these authors is less than that reported on ***Figure IV-26***. That is certainly due to the fact that Ni nanoparticles have a weaker magneto-optical activity.

To explain this behavior, we can make a link with the analytical study, led in the second chapter, of the $\omega - \vec{K}$ dispersion relation of one dimensional periodic structure. At the edge of the band gap, the wavevector curves are flattening and the group velocity of the wave decreases. In such a situation, the wavevector difference between the left and right polarizations is increased, resulting through an enhancement of the Faraday effect.

IV.3.5. Merit factor

The absorption of a magnetic Faraday rotator is a negative factor, which plays an important role on the quality of the device. The merit factor, which is the ratio between the Faraday rotation and the absorption coefficient, is studied here. ***Figure IV-31*** presents such a merit factor of the reference 2:2 monolayer (red line) and the magneto-photonic crystal (black line) which was created with a 453 nm direct opal template.

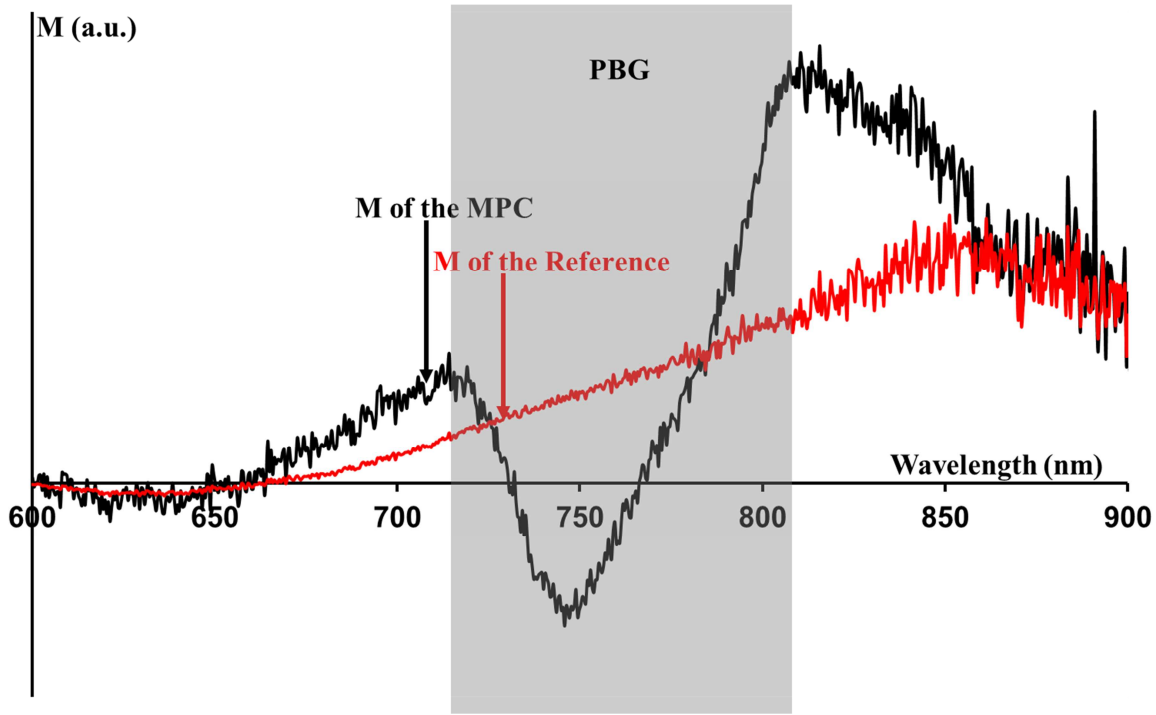

Figure IV-31: Merit factor of the MPC made by 453 nm direct opal and the merit factor of the 2:2 monolayer as a function of the wavelength

These curves are plotted with arbitrary units for the vertical axis because it has not been possible to obtain an absolute value of the transmittance of the MPC. Thus, the two graphs were normalized for a better comparison and the gray rectangle on ***Figure IV-31*** signs the area of the photonic band gap.

Out of the influence of the BPG, the curves are superimposed whereas, in the area of the band gap, the merit factor of the magneto-photonic crystal has a totally different behavior. It proves that the merit factor can be modified and increased at the edges of the PBG compared to the monolayer. This is the achievement of the main goal of this study *i.e.* the increase of the merit factor.

However, this achievement is partial due to the fact that the demonstration is based on a comparison of the spectral behavior with a classical monolayer. A full demonstration required to obtain an absolute value of the merit factor of our MPC.

CONCLUSION (FRANCAIS)

De nombreuses fonctions intégrées, telles que les amplificateurs, les sources lasers, les multiplexeurs, sont disponibles pour les systèmes de télécommunications à haute vitesse. Cependant, les isolateurs qui protègent les sources lasers ou les amplificateurs, ne sont pas disponibles sous la forme intégrée. Cette fonction est basée sur la non réciprocité de la rotation Faraday et est réalisée en utilisant un matériau magnéto-optique. Les matériaux conventionnels utilisés pour cette fonction dans la configuration d'espace libre, ne peuvent pas être intégrés en raison de la température élevée nécessaires à leur cristallisation. Afin d'y remédier, le laboratoire LT2C a développé un matériau composite basé sur l'utilisation d'une solution sol-gel de silice dopée avec des nanoparticules magnétiques de ferrite de cobalt. Ce matériau est totalement compatible avec les technologies intégrées sur verre et présente des propriétés magnéto-optiques intéressantes dans le secteur des télécommunications. Néanmoins, le facteur de mérite de ce matériau doit être amélioré.

Par ailleurs, comme exprimé dans la littérature, l'efficacité des matériaux magnéto-optiques peuvent être améliorée grâce à leur structuration sous forme de cristaux photoniques.

Ainsi, les motivations et les objectifs de cette thèse sont focalisés sur la réalisation et l'étude des cristaux photoniques en utilisant l'approche composite développé par le laboratoire. Un grand nombre de procédés sont décrits dans la littérature pour la réalisation de cristaux photoniques. Parmi eux, nous avons choisi l'auto-assemblage de micro-billes en polystyrène, en raison de sa capacité à être rempli avec un solution sol-gel. Pour réaliser cette étude, certaines mesures ont été vérifiées.

Tout d'abord, nous avons montré que l'utilisation d'un matériau composite peut augmenter le facteur de mérite par rapport à une monocouche magnétique sans arrangement périodique. Ce matériau est constitué d'une matrice sol-gel dopée avec des nanoparticules magnétiques, celle-ci constitue un cristal photonique 1D et possède un indice de réfraction relativement faible.

Ensuite, l'élaboration d'un modèle 3D à base de billes de polystyrène dans un structure cfc auto-assemblée a été obtenue en utilisant la méthode de dépôt vertical. Les bandes interdites photoniques induites par ces structures peuvent être réglées en utilisant différentes tailles de billes de polystyrène comme défini par la loi de Bragg. Les observations au MEB ont montré des zones homogènes de quelques centaines de micron carré. L'opale direct est ensuite imprégné dans une solution de TEOS dopée et non dopée, les billes de polystyrène ont été éliminées par de l'acétate d'éthyle.

Pour obtenir une rotation Faraday suffisante, la concentration volumique de nanoparticules magnétiques a dû être augmentée. Nous avons réussi, grâce à la qualité des nanoparticules magnétiques développées par Sophie Neveu du laboratoire PECSA, à atteindre 40% pour cette concentration volumique. Ce taux n'était que de quelques pour cent au début de ce travail.

Les mesures spectrales de la transmission optique en fonction de l'angle d'incidence, effectuées sur les opales direct et inverse, ont confirmé l'arrangement cfc de la structure composite avec une bonne correspondance avec les valeurs théoriques. Ces mesures ont permis de déterminer la distance interplanaire du réseau de la structure 3D pour les opales directs et inverses. Une contraction de la structure a été observée pendant le processus d'inversion.

Les mesures de polarimètrie spectrale ont permis d'obtenir le résultat principal de cette thèse. La rotation Faraday des cristaux magnéto-photoniques réalisés augmente sur les bords de la BIP. Ces augmentations sont présentes dans les premières et/ou secondes harmoniques des BIP, pour les différentes tailles de billes utilisées.

Dans ce travail, nous avons mis en évidence la capacité des cristaux magnéto-photoniques à base de nanoparticules magnétiques, à modifier le comportement spectral de la rotation Faraday sur les bords de la BIP. Néanmoins, nous devons accroître la qualité et l'homogénéité des cristaux magnéto-photoniques 3D. Ceci pourrait être réalisé de différentes façons. Dans un premier temps, nous pourrions optimiser l'élaboration de l'opale direct. En effet, la tension superficielle à l'interface air-verre et la solution de polystyrène est un paramètre très sensible, un nettoyage soigneux du support doit être testé.

La température de séchage est un paramètre clé sur la vitesse de tirage au niveau du ménisque et influence, donc, considérablement l'organisation de l'opale direct et doit être

optimisée. Inspirée des travaux de Hatton *et al.*[94], une autre procédure de fabrication peut également être utilisée : l'étape d'imprégnation et l'élaboration des opales directs peuvent être fusionnées. Dans ces conditions, le dépôt vertical peut être réalisé en utilisant un mélange d'une solution sol-gel à base de billes de polystyrène et de silice. Cette dernière procédure peut être très intéressante, car elle peut proposer une structure homogène avant l'élimination des billes de polystyrène.

Par ailleurs, les mesures spectrales de la rotation Faraday doivent être réalisées avec un banc optique plus sensible afin d'obtenir des courbes moins bruitées. Cette amélioration pourrait être possible par utilisation d'une modulation photo-élastique associée à une détection synchrone de l'amplificateur.

Ensuite, si les travaux mentionnés précédemment sont réalisés avec succès, les cristaux magnéto-photoniques 3D pourraient être appliqués comme couche de couverture sur des guides d'ondes réalisés par échange d'ions sur du verre. En effet, les perspectives à long terme du laboratoire étant l'intégration de la fonction d'isolateur, il semble pertinent de tester la capacité de l'opale à être intégré dans les technologies sur verre.

CONCLUSION

Numbers of integrated functions, such as amplifiers, laser sources, multiplexers, are available for high speed telecommunication systems. Netherless, isolation, which protects laser sources or amplifiers, is missing. This function is based on the non reciprocal Faraday rotation and is achieved using magneto-optical material. Conventionnal materials used for this function in free space configuration, can not be integrated due to the high temperature required for their cristallization.

To overcome this, LT2C laboratory has developed a composite material based on the use of cobalt ferrite magnetic nanoparticles to dope a silica sol-gel solution. This material is fully compatible with glass integrated technologies and presents interesting magneto-optical properties in the telecom area. Nevertheless, it's merit factor has to be improved.

Moreover, as expressed in the literature, efficiency of magneto-optical materials can be enhanced through their structuration as photonic crystals.

Thus, motivations and goals of this thesis were concerned by the realization and the study of photonic crystals using the composite approach developed by the laboratory. A lot of processes are described in the literature for the realization of photonic crystals. Among them, we have chosen self-assembled polystyrene micro-spheres arrangement method, for its ability to be filled with a sol-gel solution.To carry out this study, some steps have been checked.

Firstly, we have shown, that the use of a dilute magnetic material with a relatively low refractive index in a 1D photonic crystal, can increase the merit factor compared to a single magnetic monolayer.

Then, the elaboration of the polystyrene 3D template in a self-assembled fcc arrangement has been achieved using the vertical deposition method. The photonic band gap induced by these structures can be tuned using different sizes of polystyrene spheres as it is defined by the Bragg law. SEM observations showed homogeneous area up to few hundreds of micron square.

The direct opal was then impregnated in doped and non-doped TEOS silica solution and polystyrene spheres were eliminated by ethyl-acetate.

To obtain a sufficient Faraday rotation, the volume fraction of magnetic nanoparticles had to be increased. We managed, thanks to the quality of the nanoparticles developed by Sophie Neveu from PECSA laboratory; to reach 40%, whereas this rate was only a few percent at the beginning of this work.

The spectral optical transmission measurements performed on direct and inverse opals, as a function of the angle of incidence confirmed, with their good agreements with theoretical values, the fcc arrangement of the structure. Using these measurements, we deduced the interplanar distance of the crystal lattice for direct and inverse opal and observed shrinkage of the structure during the inversion process.

The main result of this thesis was deduced from spectral polarimeter measurements. The Faraday rotation of the realized magneto-photonic crystals showed an increase at the edges of the PBG. These increases were presented either in the PBG of first or second harmonic for all different initial sphere sizes.

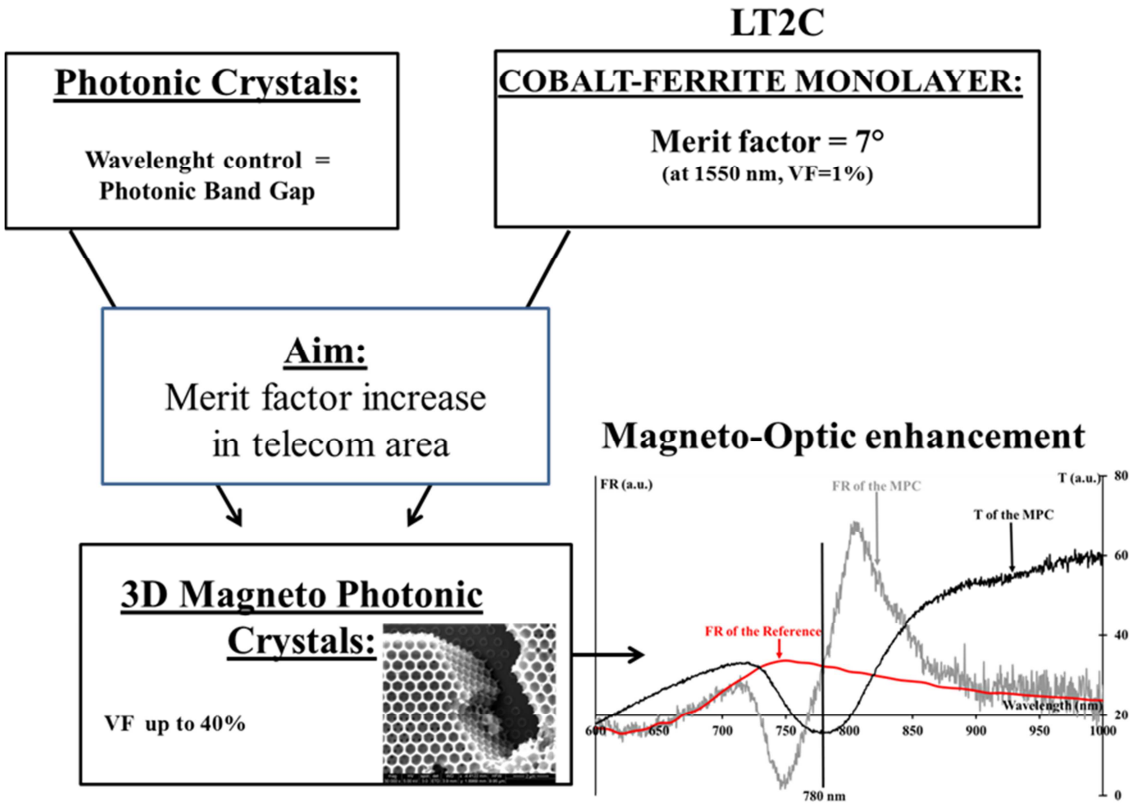

Schematic structure of this work

We have evidenced in this work the ability of the magneto photonic crystal based on the used of magnetic nanoparticles to change the spectral behavior of the Faraday rotation with an

enhancement at the edges of the PBG. Nevertheless, to go further in this way, we have to increase the quality and the homogeneity of the 3D magneto-photonic crystal.

This could be achieved by different ways. Firstly, we could optimize the direct opal elaboration. Indeed, surface tension at the interface air-glass and polystyrene dispersion is a very sensitive parameter, and a carefully cleaning of the substrate should be tested. The drying temperature, through its influence on the withdrawing speed of the meniscus, plays also an important role in the direct opal organization and should be optimized. Other procedure can be used also, like based on a work of Hatton *et al*. [94], where the impregnation step and the direct opal elaboration were merged. Thus the vertical deposition can be done using a mix of polystyrene-silica sol-gel solution. This last procedure can be very interesting, because it can propose a homogeneous structure before the elimination of the polystyrene spheres.

Moreover, spectral Faraday rotation measurements should be done with a more sensitive optical bench to obtain less noisy curves. This could be done using photo elastic modulation associated with lock-in amplifier detection.

If the previously mentioned works were successfully done, the magnetic three dimensional photonic crystals could be applied as a cover layer of an ion-exchanged glass waveguide. Indeed, long term perspectives of our laboratory being the integration of isolation function, it looks relevant to test the ability of the opal to be integrated in glass technologies.

ACKNOWLEDGEMENT

First of all I would like to thanks for the committee for taking time of understanding and criticizing my work with a strict and wise scientific aspects.

I am heartily thankful to my directors, Jean-Pierre Chatelon, Francois Royer and Damien Jamon, for their encouragement, guidance and support from the initial to the final aim, whom enabled me to develop an understanding of the subject. But they were not just my colleagues, but friends. They helped, when I lost in the beginning my luggage at the airport, buying furniture to my flat and when I asked help of learning their beautiful language (French). I cannot be grateful them enough.

I also would like to thanks for Professor Etelka Tombacz who proposed me this opportunity in Szeged three years ago. She also was my co-director of this work and helping me developing the polystyrene structure.

I am very grateful to Dr. Marie-Francois Blanc Mignon for her collaboration of taking the Scanning Electron Microscope Images to see the nano-arrangement of our opals.

I also like to thank for Jean-Jacques Rousseau and for all colleagues in the Laboratorie Telecom Claude Chappe who contributed to this study.

I am very grateful for the motivation from my family, my mother and my friends.

Lastly, I offer my regards and blessings to all of those who supported me in any respect during the completion of the project.

Renata Kekesi

REFERENCE

1. Choueikani F, Royer F, Jamon D, et al. Optical and magneto-optical characterisation of planar waveguides fabricated via organic-inorganic sol-gel process doped by cobalt-ferrite nanoparticles. *Optical Society of America*. 2010.

2. Inoue M. *Magneto-optical materials for photonics and recording-Magnetophotonic Crystals*. Boston, Massachusets; 2004.

3. Levy M, Yang HC, Steel MJ, Fujita J. Flat-Top Response in One-Dimensional Magnetic Photonic Bandgap Structures With Faraday Rotation Enhancement. *Journal of Lightwave Technology*. 2001;19(12):1964.

4. Inui C, Yosuke T, Hiroaki K, et al. Preparation of one-dimensional photonic crystals by sol-gel process for magneto-optical materials. 2008;516(6):481.

5. Inoue M, Arai K, Fujii T, Abe M. One-Dimensional Magnetophotonic Crystals. 1999;85(8):5768-5770.

6. Kahl S, Grishin AM. Enhanced Faraday rotation in all-garnet magneto-optical photonic crystal. *Applied Physics Letters*. 2004;84(9):1438.

7. Nishijima Y, Ueno K, Juodkazis S, et al. Inverse silica opal photonic crystals for optical sensing applications. *Optics Express*. 2007;15(20):12979-12988.

8. Kekesi R, Royer F, Blanc Mignon MF, et al. Preliminary studies of 3D Magnetophotonic Crystals designed from a template stuffed by sol-gel process. Dans: *Proceedings of SPIE, the International Society for Optical Engineering*.Vol 7713.; 2010.

9. Choueikani F. Etude des potentialites de couches minces sol-gel dopées par des nanoparticles magnétiques pour la réalisation de composants magnéto-optiques integrés. 2008.

10. Wittekoek S, Popma TJA, Robertson JM, Bongers PF. Magneto-optic spectra and the dielectric tensor elements of bismuth-substituted iron garnets at photon energies between 2.2-5.2 eV. *Phys. Rev. B*. 1975;12:2777–2788.

11. Royer F, Jamon D, Rousseau JJ, et al. Magneto-optical properties of CoFe2O4 ferrofluids. Influence of the nanoparticle size distribution. *Progress in colloid & polymer science*. 2004;126:155-158.

12. Thorlabs. Technical Documentation of Thorlabs.

13. Hutchings DC. Prospects for the implementation of magneto-optic elements in optoelectronic integrated circuits: a personal perspective. *Journal of Physics D: Applied Physics*. 2003;36(18):2222.

14. Ishii K, Hoshi Y, Naoe M, Yamanaka S. Preparation of stoichiometric YIG _lms by sputtering," In Ferrites. *SPIE Procceedings. SPIE, Belligham, WA*. 1980.

15. Fujita J, Gerhardt R, Eldada L. Optoelectronics interconnects, integrated circuits. *Proceedings SPIE*. 2002;4142:78-85.

16. Shoji Y, Mizumoto T, Yokoi H, Hsieh IW, Osgood RM. Magneto-optical isolator with silicon waveguides fabricated by direct bonding. *Applied Physics Letters*. 2008;92(7):071117.

17. Joudrier AL, Couchaud M, Moriceau H, et al. Direct bonding conditions of ferrite garnet layer on ion-exchanged glass waveguides. *Physica status solidi. A, Applications and materials science*. 2008;205(10):2313-2316.

18. Zayets V, Debnath M, Ando K. Optical isolation in Cd_1−xMn_xTe magneto-optical waveguide grown on GaAs substrate. *JOSA B*. 2005;22(1):281-285.

19. Shimizu H, Tanaka M. Design of semiconductor-waveguide-type optical isolators using the nonreciprocal loss/gain in the magneto-optical waveguides having MnAs nanoclusters. *Applied Physics Letters*. 2002;81(27):5246.

20. Shimizu H, Tanaka M. Magneto-optical properties of a Si-doped GaAs:MnAs-based magneto-photonic crystal operating at 1.55μm. *Physica E: Low-dimensional Systems and Nanostructures*. 2002;13(2-4):595-601.

21. Lesuffleur A, Vanwolleghem M, Gogol P, et al. Magneto-optical parameters of Co90Fe10 and Co50Fe50 ferromagnetic thin films for 1.3 μm integrated isolator. *Journal of Magnetism and Magnetic Materials*. 2006;305(2):284-290.

22. Royer F, Jamon D, Rousseau JJ, et al. Magneto-optical nanoparticle-doped silica-titania planar waveguides. *Applied Physics Letters*. 2005;86:011107.

23. Huang M, Xu ZC. Wavelength and temperature characteristics of BiYbIG film/YIG crystal composite structure for magneto-optical applications. *Applied Physics A: Materials Science & Processing*. 2005;81(1):193-196.

24. Shintaku T, Tate A, Mino S. Ce-sustituted yttrium iron garnets prepared on Gd3Sc2Ga3O12 garnet substrate by sputter epitaxy. *Applied Physics Letters*. 2002;81:5246-5248.

25. Zaman TR, Xiaoyun G, Ram RJ. Semiconductor Waveguide Isolators. *Journal of Lightwave Technology*. 2008;26(2):291-301.

26. Kim HS, Bi L, Dionne GF, Ross CA. Magnetic and magneto-optical properties of Fe-doped SrTiO3 films. *Applied Physics Letters*. 2008;93(9):092506.

27. Lopez-Santiago A, Gangopadhyay P, Thomas J, et al. Faraday rotation in magnetite-polymethylmethacrylate core-shell nanocomposites with high optical quality. *Applied Physics Letters*. 2009;95(14):143302.

28. Choueikani F, Royer F, Jamon D, et al. Magneto-optical waveguides made of cobalt ferrite nanoparticles embedded in silica/zirconia organic-inorganic matrix. *Applied Physics Letters*. 2009;94:051113.

29. Donatini F. Etude de l'anisotropie optique circulaire magneto-induite des ferrofluides dans le dominaine spectral visible-proche infrarouge applications. 1996.

30. Donatini F, Jamon D, Monin J, Neveu S. Experimental investigation of longitudinal magneto-optic effects in four ferrite ferrofluids in visible-near infrared spectrum. *IEEE Transactions on Magnetics*. 1999;35(5):4311-4317.

31. Royer F, Jamon D, Broquin JE, et al. Fully compatible magneto-optical sol-gel material with glass waveguides technologies: application to mode converters. *SPIE proceedings series, Conference, San Francisco*. 2011;7941.

32. Amata H, Royer F, Choueikani F. Hybrid magneto-optical mode converter made with a magnetic nanoparticles-doped SiO2/ZrO2 layer coated on an ion-exchanged glass waveguide. *Applied Physics Letters*. 2011.

33. Khartsev SI, Grishin AM. High performance [Bi3Fe5O12/Sm3Ga5O12]m magneto-optical photonic crystals. *Journal of Applied Physics*. 2007;101(5):053906.

34. Inoue M, Fujikawa R, Baryshev A, et al. Magnetophotonic crystals. *Journal of Physics D: Applied Physics*. 2006;39(8):151-161.

35. Sugimoto Y, Ikeda N, Carlsson N, et al. Fabrication and characterization of different types of two-dimensional AlGaAs photonic crystal slabs. *Journal of Applied Physics*. 2009;91(3):922-929.

36. Ovsianikov A, Ostendorf A, Chichkov BN. Three-dimensional photofabrication with femtosecond lasers for applications in photonics and biomedicine. *Applied Surface Science*. 2007;253(15):6599-6602.

37. Yablonovitch E. Inhibited Spontaneous Emission in Solid-State Physics and Electronics. 1987;58:2059–2062.

38. John S. Strong localization of photons in certain disordered dielectric superlattices. *Phys. Rev. Lett.* 1987;58:2486–2489.

39. Mı guez H, Lopez C, Meseguer F, et al. Photonic crystal properties of packed submicrometric SiO2 spheres. 1997;71:1148 - 1150.

40. Ye YH, Leblanc F, Haché A, Truong VV. Self-assembling three-dimensional colloidal photonic crystal structure with high crystalline quality. *Applied Physics Letters*. 2001;78:52.

41. Galisteo-Lopez JF, Palacios-Lidon E, Castillo-Martinez E, Lopez C. Optical study of the pseudogap in thickness and orientation controlled artificial opals. *Physical review B. Condensed matter and materials physics*. 2003;68(11):115109.1-115109.8.

42. Grishin AM. Amplifying magneto-optical photonic crystal. *Applied Physics Letters*. 2010;97:061116.

43. Wu Z, Levy M, Fratello VJ, Merzlikin AM. Gyrotropic photonic crystal waveguide switches. *Applied Physics Letters*. 2010;96(5):051125.

44. Śmigaj W, Romero-Vivas J, Gralak B, et al. Magneto-optical circulator designed for operation in a uniform external magnetic field. *Optics Letters*. 2010;35(4):568-570.

45. Baryshev AV, Kodama T, Nishimura K, Uchida H, Inoue M. Magneto-optical properties of three-dimensional magnetophotonic crystals. *Magnetics, IEEE*. 2004;40(10.1109/TMAG.2004.832282):2829 - 2831.

46. Pavlov PP, Usachev PA, Pisarev RV, et al. Enhancement of optical and magneto-optical effects in three-dimensional opal/Fe3O4 magnetic photonic crystals. *Applied physics letters*. 2008;93(7).

47. Koerdt C, Rikken GLJA, Petrov EP. Faraday effect of photonic crystals. *Applied physics letters*. 2003;82(10):1538-1540.

48. Caicedo JM, Pascu O, Lopez-Garcia M, et al. Magnetophotonic response of three-dimensional opals. *ACS Nano*. 2011;5(4):2957-2963.

49. Yablonovitch E. Photonic crystals: semiconductors of light. *Scientific American*. 2001;285:47-51.

50. Joannopoulos JD, Winn JN, Meade RD. *Photonic Crystals-Molding the Flow of Light*. 2e éd. Priceton, New Jersey: Priceton University Press; 2008.

51. Sakoda K. *Optical Properties of Photonic Crystals*. Verlag Berlin Heidelberg New York: Springer; 2001.

52. Kittel C. *Introduction to Solid State Physics*. 6e éd. United States of Amerika: John Wiley & Sons, Inc.

53. Saleh BEA, Teich MC. *Fundamentals of Photonics*. 2e éd. New Jersey: Wiley-Interscience; 2007.

54. Lopez JFG. An optical study of opal based photonic crystals. 2005.

55. Visnovsky S, Postava K, Yamaguchi T. Magneto-optic polar Kerr and Faraday effects in periodic multilayers. *Optics Express*. 2001;9(3):158-171.

56. Hamon T, Buil S, Popova E, Dahoo PR, Keller N. Investigation of a one-dimensional magnetophotonic crystal for the study of ultrathin magnetic layer. *Journal of Physics D: Applied Physics*. 2006;39(6):1012.

57. Višňovský S, Lopušník R, Nývlt M, et al. Analytical expressions for polar magnetoptics in magnetic multilayers. *Czechoslovak Journal of Physics*. 2000;50(7):857-882.

58. Tarhan II, Zinkin MP, Watson GH. Interferometric technique for the measurement of photonic band structure in colloidal crystals. *Optics Letters*. 1995;20(14):1571-1573.

59. Galisteo-Lopez JF, Ibisate M, Sapienza R, et al. Self-Assembled Photonic Structures. *Advanced Materials*. 2011;23(1):30-69.

60. Lopez C. Materials Aspects of Photonic Crystals. *Advanced Materials*. 2003;15(20):1679-1704.

61. Lopez C. Three-dimensional photonic bandgap materials: semiconductors for light. *Journal of Optics A: Pure and Applied Optics*. 2006;8(5):1-14.

62. Gu ZZ, Fujishima A, Sato O. Fabrication of High-Quality Opal Films with Controllable Thickness. *Chemistry of Materials*. 2002;14(2):760-765.

63. Hales TC. Sphere Packings 1. *Discrete & Computational Geometry*. 1997;17(1):1-51.

64. Hales TC. Sphere Packings 2. *Discrete & Computational Geometry*. 1997;18(2):135-149.

65. Octavio Alejandro Castañeda-Uribe1,3, Juan Carlos Salcedo-Reyes*1, Henry Alberto Méndez-Pinzón1, Aura Marina Pedroza-Rodríguez. Fabrication and optical characterization of a high-qualityfcc-opal-based photonic crystal grown by the vertical convectiveself-assembly method. *Universitas Scientiarum*. 2010;15(2):150-158.

66. Waterhouse GIN, Waterland MR. Opal and inverse opal photonic crystals: Fabrication and characterization. *Polyhedron*. 2007;26(2):356-368.

67. Cao Y, Wang Y, Zhu Y, et al. Fabrication of anatase titania inverse opal films using polystyrene templates. *Superlattices and Microstructures*. 2006;40(3):155-160.

68. Abramova V, Sinitskii A. Large-scale ZnO inverse opal films fabricated by a sol–gel technique. *Superlattices and Microstructures*. 2009;45(6):624-629.

69. Jin Y, Zhu Y, Yang X, Li C, Zhou J. Fabrication and characterization of cerium-doped barium titanate inverse opal by sol–gel method. *Journal of Solid State Chemistry*. 2007;180(1):301-306.

70. Jin Y, Zhu Y, Yang X, Wei C, Li C. Fabrication and characterization of cerium-doped titania inverse opal by sol–gel method. *Materials Chemistry and Physics*. 2007;106(2-3):209-214.

71. Stein A, Schroden RC. Colloidal crystal templating of three-dimensionally ordered macroporous solids: materials for photonics and beyond. *Current Opinion in Solid State and Materials Science*. 2001;5(6):553-564.

72. Garcia MT, Garcia I, Duque G, Lucas A, Rodriguez JF. Study of the solubility and stability of polystyrene wastes in a dissolution recycling process. *Waste Management*. 2009;29(6):1814-1818.

73. Cao Y, Wang Y, Zhu Y, et al. Fabrication of anatase titania inverse opal films using polystyrene templates. *Superlattices and Microstructures*. 2006;40(3):155-160.

74. Jin Y, Zhu Y, Yang X, Li Y, Zhou J. Fabrication and characterization of cerium-doped barium titanate inverse opal by sol–gel method. *Journal of Solid State Chemistry*. 2007;180(1):301-306.

75. Li Y, Piret F, Leonard T, Su BL. Rutile TiO2 inverse opal with photonic bandgap in the UV—visible range. *Journal of colloid and interface science*. 2010;348(1):43-48.

76. Jin Y, Zhu Y, Yang X, Wei C, Li C. Fabrication and characterization of cerium-doped titania inverse opal by sol–gel method. *Materials Chemistry and Physics*. 2007;106(2-3):20-214.

77. Yang Z, Huang X, Yang G, et al. Preparation and photonic bandgap properties of lead lanthanum titanate inverse opal photonic crystals. *Journal of Alloys and Compounds*. 2009;468(1-2.):295-298.

78. Wang A, Chen SL, Dong P, Zhou Z. Preparation of photonic crystal heterostructures composed of two TiO2 inverse opal films with different filling factors. *Synthetic Metals*. 2011;161(5-6.):504-507.

79. Brinker, Jeffrey C. *Sol-gel science*. Boston: Academic Press; 1990.

80. Sakka, Sumio, Kozuka, Hiromitsu. *Handbook of sol-gel science and technology*. Boston: Kluwer academi; 2005.

81. Choi SS, Lee SG, Im SS, Kim SH, Loo YL. Silica nanofibers from electrospinning/sol-gel process. *Journal of Materials Science Letters*. 2003;22(12):891-893.

82. Neveu S, Bee A, Robineau M, Talbot D. Journal of Colloid and Interface Science : Size-Selective Chemical Synthesis of Tartrate Stabilized Cobalt Ferrite Ionic Magnetic Fluid. *Journal of Colloid and Interface Science*. 2002;255(2):293-298.

83. Massart R. Preparation of aqueous magnetic liquids in alkaline and acidic media. *IEEE Transactions on Magnetics*. 1981;17(2):1247-1248.

84. Choueikani F, Royer F, Douadi S, et al. Low birefringent magneto-optical waveguides fabricated via organic-inorganic sol-gel process. *The European Physical Journal Applied Physics*. 2009;47(3):30401.p1-30401.p8.

85. Jiao Z, Wu M, Qin Z, Lu M, Gu J. The NO2 sensing ITO thin films prepared by ultrasonic spray pyrolysis. *Sensors*. 2003;3(8):285-289.

86. Petersson L, Meier P, Kornmann X, Hillborg H. Effect of surface cleanliness of aluminium substrates on silicone rubber adhesion. *Journal of Physics D: Applied Physics*. 2011;44(3):034011.

87. Reimer L. Scanning Electron Microscopy, Physics of Image Formation and Microanalysis. Dans: Berlin: Springer -Verlag; 1985.

88. Thornton PR. Scanning Electron Microscopy, Applications to Materials and Device Science. Dans: 1er éd. London: Chapman and Hall LTD; 1968.

89. Levenberg K. A method for the solution of certain problems in least squares. *Quart. Applied Math*. 1944;2:164-168.

90. Marquardt DW. An Algorithm for Least-Squares Estimation of Nonlinear Parameters. *SIAM J. on Applied Mathematics*. 1963;11(2):431-441.

91. Daveze P. Contribution a l'Etude des Proprietes Magneto-Optiques des Liquides Magnetiques. Applications Opto-Electroniques. 1992.

92. Xie H, Wei J, Zhang X. Characterisation of Sol-gel Thin Films by Spectroscopic Ellipsometry. *Journal of Physics: Conference*. 2006;28:95-99.

93. Vincent A, Babu S, Brinley E, et al. Role of Catalyst on Refractive Index Tunability of Porous Silica Antireflective Coatings by Sol−Gel Technique. *J. Phys. Chem. C*. 2007;111(23):8291-8298.

94. Hatton B, Mishchenko L, Davis S, Sandhage KH, Aizenberg J. Assembly of large-area, highly ordered, crack-free inverse opal films. *Proc Natl Acad Sci U S A.* 2010;107:10354-9.